

Diss. ETH No. 17031

**Production and Characterization
of Small Sized Zn_xO_y
Molecules in Gas Phase**

A dissertation submitted to the
SWISS FEDERAL INSTITUTE OF TECHNOLOGY
(ETH ZURICH)

for the degree of
DOCTOR OF SCIENCE

presented by
DANIELE CANNAVÒ
Dipl.-Phys., University of Rome “La Sapienza”
born September 6, 1971
citizen of Latina, Italy

accepted on the recommendation of
Prof. Dr. Alexander Wokaun, examiner
Prof. Dr. Renato Zenobi, co-examiner
Dr. Thomas Gerber, co-examiner

2007

Abstract

Diatomic and polyatomic zinc oxides and zinc-complexes are the subject of many studies in the fields of semiconductor and catalysis research, to mention only two of many important areas.

In the context of sustainable energy conversion, advanced projects aim at using zinc as a storage medium for solar energy. First, zinc oxide is reduced to zinc in a solar heated reactor. Metallic zinc can then be used as a fuel or as an agent to produce hydrogen in a water splitting reaction. Both processes return zinc oxide that can be recycled. In order to model the processes that take place in a high temperature reactor, understanding the behavior of Zn, ZnO and Zn_xO_y in the gas phase is extremely important.

Surprisingly there have only been a few investigations of diatomic ZnO, and the implications of the experimental data/evidence for ZnO in gas phase obtained so far remain controversial. Our goal is to establish whether stable ZnO molecules and multi-atomic zinc oxides exist. For this purpose, Zn_xO_y molecules have to be prepared in an environment suited for spectroscopic measurements; energy states and binding energies could then be determined. This data would allow an accurate description of the separation of zinc from heated ZnO powders in solar reactors. The knowledge of Zn gas-phase reactions is of great importance, as it can be used, for example, to facilitate an optimal removal of zinc in the context of waste incineration.

This thesis describes experimental approaches to produce ZnO molecules in a molecular beam. The setup comprised a pulsed supersonic noble gas jet. The noble gas can be seeded with O_2 , N_2O or H_2O .

Zinc vapour was produced by laser ablation from a sample of solid zinc. The Zn vapour plume was produced at an appropriate time such that the seeded noble gas pulse could entrain it. Laser vaporization produces high yields of Zn/ZnO without the need to heat any other part of the system such as a crucible. While expanding into vacuum, the gas jet is cooled to very low temperatures by collisions of the gas molecules, thus reducing internal

molecular energy in favor of kinetic energy. The very low temperature conditions facilitate the stabilization of species formed prior to expansion, even if they are only weakly bound. A time-of-flight mass spectrometer (Tof-MS) incorporating a dual stage reflectron was used for the detection of chemical species that showed up in the molecular beam. Molecules with masses ranging from 1 to 800 Da could be thus detected.

The timing of events could be varied during an experiment in order to maximize the signal associated to a given molecule. Parameters affecting the results, like the concentration of the oxygen containing species seeded in the noble gas, the intensity and wavelength of the ablation/ionization laser, etc. could also be varied deliberately.

Several gas mixtures ranging from pure (99%) O₂ and N₂O to their lean dilutions in He, Ne, Ar have been used for expansion of the zinc plume. Neutral zinc compounds containing oxygen could be observed only with lean mixtures of a few percent of seed gas. The impact of the laser power on the cooling of zinc after expansion has been characterized quantitatively by relating the broadening of zinc peaks with the transversal thermal velocity.

Test measurements with the setup using niobium produced niobium-oxides as well as Nb_n clusters. This confirmed that our experimental setup is suited for metal oxidation and cluster aggregation studies.

The results of the experiments presented in this thesis provide evidence that ZnOH and ZnO can be produced in a molecular beam, though the yield is surprisingly low compared to results obtained with other metals. The experimental results allow to recognize water as the H donor involved in ZnOH formation. In the experiments, neutral compounds or clusters other than ZnOH, Zn₂O₂H and Zn₂O₂H-H₂ were hardly produced. The absence of small pure zinc metal clusters that are only weakly bonded (e.g. ~ 0.02 eV for Zn₂) could be explained by the fact that we, in most likelihood, did not achieve ultra cold molecular beams.

The experimental setup proved to be a flexible tool to identify, without ambiguity, traces of ZnOH and ZnO when expanding ablated zinc together with 1% N₂O. To our knowledge, this is the first direct evidence of neutral diatomic zinc oxide and zinc hydro oxide in the gas phase.

Keywords: zinc hydroxide (ZnOH), zinc oxide (ZnO), Zn_xO_y, Smalley vaporization source, time of flight (Tof), reflectron, mass, spectrometry, niobium and water clusters, SIMION, trajectories.

Zusammenfassung

Zinkoxide und Zinkkomplexe sind Gegenstand vieler Forschungsstudien in der Halbleiter- und der Katalysetechnik, um nur zwei wichtige Bereiche zu erwähnen.

Im Zusammenhang mit der nachhaltigen Energieumwandlung wird in neuen innovativen Projekten angestrebt, Zink (Zn) als Speichermedium von Solarenergie zu verwenden. Hierzu, wird zuerst Zinkoxid (ZnO) in einem geheizten Solarreaktor thermolytisch zu Zink reduziert. Das metallische Zink kann dann als direkter Brennstoff oder als Ausgangsstoff zur Wasseraufspaltung genutzt werden, um Wasserstoff zu produzieren. In beiden Verfahren entsteht Zinkoxid, welches im Solarreaktor wiedereingesetzt werden kann.

Um die Prozesse in einem Hochtemperaturreaktor genau modellieren zu können, muss das Verhalten von Zn, ZnO und Zn_xO_y in der Gasphase bekannt sein. Überraschenderweise gibt es nur wenige Arbeiten über zweiatomiges ZnO, und die bisher erzielten experimentellen Ergebnisse über Zinkoxide in der Gasphase sind oft widersprüchlich. Ziel dieser Arbeit ist es, festzustellen, ob neutrale stabile ZnO-Moleküle und mehratomige Zinkoxidkomplexe in der Gasphase existieren.

Zu diesen Zweck müssen Zn_xO_y Moleküle in einer Umgebung dargestellt werden, die für spektroskopische Messungen geeignet ist. Molekül spezifische Energiezustände und Bindungsenergien könnten dann experimentell ermittelt werden. Die Kenntnis solcher Daten würde es erlauben, die Ausfällung von Zink aus dem heissen Zinksauerstoff-Gemisch im Solarreaktor genau zu modellieren und zu optimieren. Zn-Gasphasenreaktionen sind auch von grosser Wichtigkeit für die Rückgewinnung von Zink bei der Abfallverbrennung.

Diese Dissertation beschreibt experimentelle Ansätze, ZnO-Moleküle in einem Molekularstrahl darzustellen. Unter Verwendung einer Laserablations-Technik wird Zink aus einer festen Zinkprobe gelöst und verdampft. Der Zinkdampf wird durch ein vorbeiströmendes Edelgasgemisch mitgerissen. Das Edelgas kann mit O_2 , N_2O oder H_2O versetzt werden. Die Methode der Laserablation erzielt eine hohe Ausbeute von freigesetzten Zn-Atomen, ohne dass Teile der Messapparatur zur Erhöhung des Zn-Dampfdrucks zusätzlich

erhitzt werden müssen. Die Expansion des Zinkdampfgemischs ins Vakuum führt zu einer Temperatur-Erniedrigung der Gasmoleküle. Ebenso wird dabei die interne molekulare Energie zugunsten der kinetischen Energie verringert. Die sehr kalten Temperaturbedingungen erleichtern die Stabilisierung schwacher Bindungen, die während der Expansion gebildet wurden.

Ein Flugzeit-Massenspektrometer (ToF-MS) von Jordan mit einem zweistufigen Reflektron wurde verwendet, um die verschiedenen chemischen Verbindungen im Molekularstrahl zu klassifizieren. Massen von 1 bis 800 Da konnten damit aufgelöst werden.

Die zeitliche Abstimmung der Ereignisse liess sich variabel während eines Experiments gestalten, so dass selektiv Signale verstärkt werden konnten, die von einem bestimmten Molekül erzeugt wurden. Weiterhin konnten Parameter wie die Konzentration der sauerstoffhaltigen Verbindungen innerhalb des Edelgases, sowie die Intensität und die Wellenlänge des Ablationslasers variiert werden.

Verschiedene Gasmischungen, die von reinem 99% O₂ über reines N₂O bis zu deren hohen Verdünnungen mit Helium (He), Neon (Ne) und Argon (Ar) reichen, wurden im Molekularstrahl verwendet. Neutrale Zinkverbindungen, die Sauerstoff enthalten, konnten nur beobachtet werden, wenn niedrige Konzentrationen des Oxidations mittels von einigen wenigen Prozenten dem Edelgas beigemischt wurden.

Zusätzlich wurde der Einflussfaktor der Ablationslaser-Energie bezüglich des Kühleffekts nach der Expansion quantifiziert. Weiterhin wurden im Vorfeld Testmessungen an Niob durchgeführt. Unter den gegebenen Versuchsbedingungen konnten Niobium- und Niobiumoxid-Cluster produziert werden. Diese Messungen bestätigten, dass der experimentelle Aufbau prinzipiell zur Metalloxydation und Clusterbildung geeignet ist. Die experimentellen Resultate, die in dieser Dissertation präsentiert werden, zeigen, dass ZnOH und ZnO in einem Molekülstrahl erzeugt werden können, wobei die Ausbeute überraschenderweise niedrig ist im Vergleich zur Herstellung anderer Metalloxyde. Weiterhin konnte aus den vorliegenden Experimenten gefolgert werden, dass geringe Mengen von Wasser die Bildung von ZnOH begünstigt. Andere neutrale Zinkverbindungen oder Cluster ausser ZnOH, Zn₂O₂H und Zn₂O₂H-H₂ wurden kaum produziert. Das Fehlen von kleinen, reinen Zinkmetallclustern, die nur schwach gebunden sind, kann darauf zurückgeführt werden, dass ultra kalte molekulare Bedingungen nicht erreicht wurden.

Der in der Dissertation vorgestellte experimentelle Versuchsaufbau kann flexibel eingesetzt werden und ermöglicht die Herstellung geringer Mengen von ZnOH und ZnO. Unserem

Wissen nach ist dies der erste direkte Nachweis für neutrales Zinkoxid und Zinkhydroxid in der Gasphase.

Suchbegriffe: Zinkhydroxid (ZnOH), Zinkoxid (ZnO), Zn_xO_y , Smalley Verdampfungsquelle, Flugzeiten, Reflekttron, Massen Spektrometrie, Niobium und Wassercluster, SIMION, Flugbahnen.

Preface

“The long unmeasured pulse of time moves everything. There is nothing hidden that it cannot bring to light, nothing once known that may not become unknown.”

Sophocles BC 495-406, Greek Tragic Poet

For my daughter, Giulia

Acknowledgments

Zürich, June 25, 2007

I wish to thank Professor Alexander Wokaun for having given me the opportunity to work on this project, supervising my research and this dissertation with patience and attentiveness. There are a large number of people I would like to thank for support, both academically and socially, during my PhD. First of all, I wish to express gratitude to my wife, Dr. Elisabetta Chicca, for her help and encouragement when the experiments did not immediately yield results as they were supposed to do. There is no way to account for the assistance and support Dr. Gregor Knopp has given me. He was a valuable sustain for the experimental work and his contribution to its completion was substantial. He helped me a lot through fruitful discussions together with Dr. Peter Radi and Dr. Marek Tulej. Special thanks to Dr. Thomas Gerber who helped me to set up the mass spectrometer, the vacuum chamber and some of the devices I used during my research. He superintended my technical drawings and scientific writings. I appreciated the support received by Dr. Thomas Lippert who let us visit his experimental setup and gain some insight on metal ablation processes. Thanks to Dr. Rolf Bombach for his astounding technical suggestions and for his being friendly open to questions.

I am also grateful to Dr. Melanie Johnson and Andreas Walser for the assistance they generously offered to my experiments during my last months at Paul Scherrer Institute (PSI). Additionally, many people helped out to keep me healthy and sane during the last years: the Indiveri family, especially. Piotr Bodek, thanks a lot for setting up our experimental setups and for friendly sharing know-how and equipments in this time.

For financial support I would like to thank the Bundesamt für Energie (BFE) and PSI.

Daniele Cannavò



Contents

Abstract	i
Zusammenfassung	iii
Preface	vii
1 Introduction	1
2 Review: Evidence for the existence of ZnO in gas phase	7
2.1 The ZnO molecule: observations, computations and characteristics	9
3 Project Aim	17
3.1 Objective	17
3.2 Procedure, Tasks	17
3.3 Realization	17
3.4 Accompanying investigation	18
4 Experimental setup	21
4.1 Setup function and components	21
4.2 The Molecular Beam Apparatus	24
4.2.1 Pulsed Valve	25
4.2.2 Laser Vaporization	27
4.2.3 Laser systems	32
4.3 Time-of-Flight Mass Spectrometry	34
4.3.1 Jordan Re-ToF-MS: Dimensions and arrangement	35
Instrumental Design	35
Vacuum System	37

	Tof Ionization region	38
	Ion deflection and mass cutoff	39
	Liner	41
	Reflectron	41
	Ion detectors	42
	Interlocks	43
	Ionization	43
	Advantages of femtosecond lasers	44
4.4	Time delay schemes for triggering	44
4.5	Instrument characterization	52
4.5.1	Mass calibration	53
4.5.2	Re-ToF-MS Resolution	54
4.5.3	Gas Pulse	56
4.5.4	H ₂ O, Ar _x O _y clusters	57
4.5.5	Ablation laser energies	59
4.5.6	Zinc desorption	59
4.5.7	Number of ions detected	62
4.5.8	Contaminants	62
4.5.9	Zn yield versus experimental parameters	64
	Zn vaporization and ablation laser intensity	65
5	Results	71
5.1	ZnO sample	72
5.2	Nb _x O _y clusters	74
5.3	Production and observation of Zn compounds containing oxygen	77
5.4	Evidences of Zn ₂ X compounds (X=O, OH, N)	82
5.5	Summary of experiments	85
6	Discussion and Outlook	87
A	ToF-MS, reflectron and SIMION	89
A.1	Linear ToF-MS system	89
A.2	Two-Field ToF Mass Spectrometer	91
A.3	Two-field ToF-MS with a two-stage Reflectron	92

A.4	Ion time of flight vs v_{0x} and d_0 : an analytic expression	94
A.5	Set of potentials for a second order spatial focus condition	97
A.6	Two points calibration and mass correction	100
A.7	Computations with SIMION TM	100
A.8	Simulation results	103
A.9	Data evaluation and isotope distributions	124
A.9.1	C code to calculate for a molecule the relative isotopic abundance	124
B	Ablation and plume characteristics	125
C	Labview, Drivers, programs	129
C.1	Programs to scan with a SpeX monochromator	129
C.1.1	PMT in combination with a Boxchar	130
C.1.2	ICCD camera and Winview	130
Script to scan the grating and average the signal	130	
C.2	Dye laser step-motor driver	139
C.2.1	Visual basic code to move the dye laser grating	140
C.2.2	Labview code to vary the voltages on the ReTof-MS	142
C.2.3	Labview programs to adjust DG535 and BNC555 time settings	142
	Bibliography	145

List of Figures

1.1	In a solar furnace, the concentrated solar energy is used to dissociate ZnO into its components. The zinc-oxygen vapor has to be cooled rapidly in order to avoid recombination to ZnO. The gained zinc represents a mean to store energy.	2
1.2	Endothermic nature of the reaction between Zn and O: the dissociation energy of O ₂ is greater than that of ZnO. Thus, there is an energetic barrier to its formation. This gives a reason for the possible absence of ZnO in gas phase.	4
2.1	Potentials energy curves of the two lowest electronic states of ZnO along with the ZnO anion ground state, all modelled as Morse potentials versus inter-atomic distance using parameters by Bauschlicher [1] and Fancher [2]. For each state is shown the atomic asymptote (left hand side). Differences between the lowest energies values corresponding to the equilibrium internuclear distances (R_0) and the energies of the formal dissociation atoms are indicated.	8
2.2	The four lowest electronic levels of ZnO and the ZnO ⁻ electronic ground state. By photoelectron spectroscopy the lowest energy levels of the $^1\Sigma^+$ - (ground state), the $^3\Pi$ and the $^1\Pi$ states could be determined experimentally relative to the stable anion, namely a,b,c, and E.A..	9
4.1	Sketch of the actual experimental setup.	22

-
- 4.2 Schematic top view of the experimental setup. It comprises a source and a detection chamber. The laser light paths and the optical table are also sketched. The 4th and 2nd harmonic output beams generated by two distinct Nd-Yag lasers are alternatively used for material ablation. The 4th laser beam serves also for the ionization during a calibration procedure. In all other measurements the output beam of a femtosecond laser system ionizes the molecules for the mass spectrometric detection. 24
- 4.3 Front end of the solenoid valve, Series Iota One, used in our experimental set up. 26
- 4.4 A focused laser beam impinges on a zinc/zincoxide rod that revolves around and translates up and down along its cylindrical symmetry axis. The plume formed is entrained in a noble gas pulse, optionally mixed with oxygen donor molecules. 28
- 4.5 Sketches of the vaporization source with the first design of the main piece (S) (Typ 1). (b) Three dimensional drawing with a cutaway showing a cross section of the vaporization source comprising the main piece (S) and the motor holder (H). The pulsed valve (V) and the mini-motor (M) are also shown. The insets (a) and (c) illustrate respectively a side and a top view (Typ 1) of the vaporization source mid sections. 29
- 4.6 Top view of the vaporization source main piece with the second design (Typ 2) we adopted in our experiments. The gas pulse introduced by the valve flows into vacuum through the 2.5 mm diameter bore. A focused laser light enters the source piece from the 1.5 mm diameter opening on its side to ablate the rod surface. 30
- 4.7 A side view of the source-chamber. Parts labeled as 1 and 2 are the vaporization source and the ionization stage of the mass spectrometer respectively. The latter is wrapped in a metallic shroud with a conical diaphragm (skimmer) screwed on top of it. The skimmer is coaxial with the gas channel of the vaporization source positioned a few centimeters above. 31
- 4.8 Experimental setup with : Ti:S, Ti:sapphire; KLM, Kerr-lens mode locked. . 34

- 4.9 Picture 4.9(a) illustrates the ion source assembly of the Jordan Re-ToF-MS without the shroud holding the skimmer, that usually hides it. The assembly that protrudes in the ionization chamber (see Fig. 4.11), consists of repeller plate, extraction grid, acceleration grid, Einzel lenses and steering plates. The 40 mm dual microchannel plate detector is visualized in picture 4.9(b). It is mounted on a offset adaptor that fits the geometrical constraints. It provides high gain (10^6 to 10^7) with sub-nanosecond rise time on a 50 ohm output. The reflectron assembly is shown in picture 4.9(c) with an entry grid that we used at ground. Behind this, a set of several plates give a uniform repelling field. Together they form the so called repeller grid. 35
- 4.10 Schematic plot showing the typical potentials used for the Jordan ToF-MS. The ions are accelerated in the extraction/acceleration region towards the drift region. Ions with a constant speed enter the reflectron where they are decelerated and, after ion velocity reversal, accelerated back towards the detector. 36
- 4.11 The molecular beam produced by the ablation source is skimmed to select the central part within a small solid angle. Finally the remaining beam reaches the ionization stage of the mass spectrometer where it cross, transversely, a focused laser beam. The laser ionizes the molecules dispersed in the molecular beam. Emerging ions are accelerated by the DC voltage difference applied across a couple of plates, called repeller and extraction grid. A second stage (acceleration stage), where another field is applied, propels the ions further away towards the drift region, where no field is present. Ions with higher masses take more time to reach the detector. . . . 38
- 4.12 Detail of the ionization stage of the mass spectrometer from Jordan. A Ni skimmer is installed on a shroud enclosing the dual-stage ionization and acceleration section of the Re-ToF-MS. 39
- 4.13 Schematic of the HV pulse circuitry driven by a TTL signal. 39
- 4.14 Voltage vs time for the driving TTL pulse (upper trace) and the corresponding HV voltage applied to the steering plates of the Jordan Re-ToF-MS. The 40

4.15	Computed (line) and measured output signal (circles) of the Behlke fast switch versus time. Switching speeds are indicated for three instances (symbols).	41
4.16	Schematic block diagram of the connections for events synchronization in the experimental setup. The connections between devices and delay units we used in combination with the DCR- and Indi- triggering schemes and described in this section, are indicated with black and grey lines respectively. Directions of arrows show whether trigger signals are given in input or are generated by a device.	45
4.17	Master system timing diagram when the Indi-scheme is used. Ten complete acquisitions occur per second. T_0 is the period of the master clock for the DG 535 delay generator. The timing of all signals maximizes the yield of Zn with Ar, at 4 bar, as noble gas and a distance ablation source nozzle-skimmer of 4 cm.	46
4.18	Master system timing diagram when the DCR-scheme is used. The delays indicated are for Ne, at 4 bar, as noble gas and a distance ablation source nozzle-skimmer of 3.5 cm. The yield of ZnOH is maximized in correspondence to this set of values.	49
4.19	Intensity of ^{64}Zn , N_2O , N_2 and C versus ablation laser firing time for different ionization laser energies per pulse. With the overall timing conditions in table 4.2, from bottom to top the energies are $150\ \mu\text{J}$, $150\ \mu\text{J}$, $130\ \mu\text{J}$, $90\ \mu\text{J}$ and $65\ \mu\text{J}$	50
4.20	Intensity of the ^{64}Zn isotope versus delay between ablation laser and valve opening. Parameter for the curves is the aperture times of the pulsed valve. Conditions are the same as in Fig. 4.19.	51
4.21	A mass spectrum obtained using the capabilities of the digital oscilloscope and the high repetition rate of the fs-laser firing with respect to the frequency of data acquisition. The signal of chemical species always contained in the vacuum chamber, being equal in both the molecular beam spectrum and its reference acquired in sequence, can be removed by subtraction. Due to some drawbacks, described in the text, it has not been adopted for the measurements.	52

- 4.22 The para-xylene mass spectrum obtained by ionizing the molecular beam with a 266 nm laser beam (≈ 150 mJ/pulse). The spectrum was averaged over a hundred of consecutive acquisitions occurring at 10 Hz. The p-xylene is seeded in Ar with a pressure of 2 bar. 53
- 4.23 Mass versus time plot used for Re-ToF-MS calibration. (M_i, t_i) data points (rhombi) are obtained by guessing peaks occurring at time t_i in the signal by the Re-ToF-MS to be originated by M_i ion masses. Continuous line is a quadratic polynomial which give the best fit to the points. 54
- 4.24 Gaussian fit of the peak at 106 Da in Fig. 4.22. The parameters used for the resolution calculation are determined. 55
- 4.25 Ion intensity of N_2O versus time delay between valve opening and laser ionization (upper thick marks). The measured signal is proportional to the gas density. The scale on the bottom gives the time in microseconds, starting from the rising edge of the shadowed signal. 56
- 4.26 Mass spectrum acquired in the region between 75 Da and 600 Da using a gas mixture of Ar with 1% O_2 at 4 bar with the vaporization source not yet installed. 58
- 4.27 Spectrum acquired using a moist Ar+1% O_2 mixture with 2 bar between 1 Da and 250 Da. 58
- 4.28 Mass ablation per laser fire as determined in a series of measurements for the number of laser shots indicated at the bottom. The resulting yield of zinc per shot is of about 0.5 μg 60
- 4.29 Three photos of Zn and ZnO rods are shown. They are shots of a camera used in combination with a microscope. The photos were taken with various magnification of the microscope: 1X, 2X for Zn and 5X for ZnO, as indicated by the labels on each photo. 61
- 4.30 Mass spectra obtained in a mass range from 1 Da to 175 Da with (upper trace) and without (intermediate trace) the vaporization source running. Peaks occurring at the same masses in both the spectra, are found mostly similar (also in the intensity distribution) to those characteristic of a contaminant, Di-n-octyl phthalate, whose mass spectrum from NIST is shown at the bottom. 63

- 4.31 Optimization of Zn^+ signal. A range of measurements are shown for different back pressures of Argon, valve aperture times and detector sensitivities. 64
- 4.32 The intensity fading obtained by turning a graduated knob is represented in this plot for two different input laser powers (155 mW: red circles, 130 mW: black squares). The attenuation counter ranges from 2 to 12.5. 65
- 4.33 ^{64}Zn intensity measured with the mass spectrometer in the ion detection time domain. In a pseudo-3D plot are shown the data obtained for some power values of the ablation laser output beam, ranging from 0 mW to about 41 mW. 66
- 4.34 Areas beneath ^{64}Zn peaks of Fig 4.33, normalized to their maximum value, are plotted versus the power of the ablation laser output beam. 66
- 4.35 FWHM of ^{64}Zn peak (right y-axis) versus ablation laser power of the 266 nm output beam with 10 Hz frequency. Each measured peak broadening with indicated FWHM value could result from a contribution of the ion initial velocity distribution with values in the interval $[-v_{min}, v_{min}]$. The ordinates on the left axis show the computed velocities, v_{min} for the values of FWHM indicated on the right-hand-side. 68
- 5.1 Mass spectra measured in the interval between 60 Da and 170 Da. When ablating the ZnO sample, the valve let enter Ar at 4 bar back pressure. Results were not appreciably modified by the addition of 1% N_2O (O_2). (1) MCP highest sensitivity and the mass gate activated; (2) MCP intermediate sensitivity and mass gate off; (3) MCP intermediate sensitivity, without ablation laser and mass gate off. Vertical lines indicate the intensities and relative positions of the $C_{24}H_{38}O_4$ contaminant fragments. 72
- 5.2 Mass spectra obtained in the range of 1–59 Da by the ablation of ZnO in Ar at 4 bar back pressure. Results were not appreciably modified by the addition of 1% N_2O (O_2). Conditions for obtaining traces (1), (2), and (3) are those of Fig. 5.1 73
- 5.3 Distribution of niobium oxide clusters produced from a laser-induced plasma reaction of niobium with oxygen. 75
- 5.4 An enlarged view of the data presented in Fig. 5.3. The masses of niobium clusters containing two atoms of Nb are visible. 76

- 5.5 A detail of Fig. 5.3. Masses of niobium clusters with three atoms of Nb are shown. 77
- 5.6 Mass spectrum with Zn vapour in Ar and 1% O₂. Back pressure is 5 bar. The intensity of the upper trace between 78 Da and 90 Da, is magnified 10 times for comparison. 79
- 5.7 Mass spectrum obtained at the same conditions as in Figure 5.6 with (upper trace) and without (lower trace) laser ablated zinc plume. Peaks corresponding to ZnOH are evident with operating ablation source. The small peaks found at 80 and 82 Da might be related to ZnO (expanded inlay). . . 80
- 5.8 Mass spectrum of the molecular beam obtained by the expansion into vacuum of Ar and 1% N₂O, at 5 bar back pressure, seeded with Zn vapour. A histogram of the integrated measured peak intensities between 76 and 86 Da (dark grey) is shown above the spectrum. In the given mass interval the observed peak pattern could be determined by the simultaneous presence of ZnC, ZnCH, ZnN, ZnNH, ZnO and ZnOH in the molecular beam. The best fit of the histogram (light grey) determines for each molecule the relative abundances, respectively 12%, 7%, 48%, 12%, 22% and 0%. 81
- 5.9 Mass spectrum (and smoothed trace) between 79 and 189 Da in Ne+1% O₂ at 5 bar (back pressure). The smoothed trace obtained by averaging 25 adjacent samples, is superimposed to the measured spectrum (gray). Peaks referred to ZnOH, (ZnO)₂H, and Zn₂(OH)₃ presence are marked accordingly. 82
- 5.10 Mass spectrum (and smoothed trace) between 160 and 190 Da in Ne+1% O₂ at 5 bar (back pressure). Bottom: the smoothed trace obtained by averaging 25 adjacent samples is superimposed on the measured spectrum (gray). Top: the synthetic isotopic mass abundances of a contaminant, (ZnO)₂H and Zn₂(OH)₃ are traced on two parallel lines one above the other. The sum of the traces is eventually plotted on a third line above the other two. . . 83
- 5.11 Mass spectrum (and smoothed trace) between 160 and 170 Da with Zn vapour in Ne and 1% O₂ at a back pressure of 5 bar. The peaks can be attributed to (ZnO)₂H. The upper trace shows a synthetic mass spectrum of (ZnO)₂H taking into account the isotopic pattern of zinc and the resolution of our Re-ToF MS. 84

- 5.12 Mass spectrum (and smoothed trace) between 178 and 188 Da with Zn vapour in Ne and 1% O₂ at a back pressure of 5 bar. The peaks can be attributed to Zn₂(OH)₃. The upper trace shows the corresponding synthetic mass spectrum of Zn₂(OH)₃ reflecting the isotopic pattern of zinc. 84
- A.1 Schematic representation of a ToF-MS working principle: the arrival time to the detector of heavy ions (size indicated) is shorter than that of lighter ones and the difference increase linearly with the drift region length. Above, a chart illustrates a typical potential field along the spectrometer. 90
- A.2 Sketch of a two stages time of flight mass spectrometer. The distances between the electrodes in the extraction and acceleration stages are marked as d_1 and d_2 ; as for the linear ToF, d_0 and D indicate the depth of ions produced in the first stage and the drift tube length respectively. The electrode potentials are also designated. 91
- A.3 A sketch of the Re-ToF mass spectrometer we considered for calculations. The characteristics of its geometry resembles closely those of the Jordan model we used. The distances among electrodes each with the associated potentials are designated by symbols used in the text. 93
- A.4 Schematic drawing which illustrates the relation between the initial ion velocity and the parameters defined in eq. A.20. 95
- A.5 Comparison of the kinetic energy dispersion attenuations with and without reflectron 96
- A.6 Set of potentials along the Re-ToF versus its voltage at the extraction grid, obtained by imposing the condition listed in the box. The circles are used to show the set of potentials suggested by the user manual to start operation, optimized for 100 Da. The time of flight is plotted to observe that as long as we move to lower potentials the spatial resolution is expected to improve. 97
- A.7 The set of potentials which are solution for the eq. A.5 for a cation of mass 100 Da are plotted in function of the potential at the extraction grid. ToF and t_{turn} are also shown. The corresponding values of $t_{turn}^{1\text{ eV}}$ and of the spatial resolution are also shown. At higher potentials we expect a gain of spatial resolution and a contemporary increase of the time dispersion due to initial kinetic energy. 98

- A.8 Data flow diagram of the program we implemented. The main steps for computing the voltage values to be assigned to the electrodes of the Jordan Re-ToF mass spectrometer, maximizing the resolution, are indicated. 99
- A.9 A sketch of the 3D model of the Jordan ToF-spectrometer with reflectron. It is used by SIMION for numerical computations. 101
- A.10 The trajectories of the ions computed using SIMION. The ion flight paths have to be consistent with the geometrical constraint as well as with the voltage differences applied across the electrodes of the mass spectrometer, that determine all together the potential energy the ions are subjected to. On the bottom the effective potential energy surface found for the actual geometry of our spectrometer and the potential set₁₉ of table A.2 is shown. 105
- A.11 Time of flight distribution at the detector of 75 positive ions all having mass M (shown on the right) when set₀ potentials (in table A.2) are used. The bin size is 0.4 ns for all histograms. 106
- A.12 Histograms of the times of flight at the detector of 75 ions all having mass M , indicated on the right side. The potentials in the mass spectrometer are those of set₉ (see table A.2), bin size and vertical scales are the same as in Fig. A.11. 107
- A.13 The frequency distribution of the times of flight at the detector of 75 ions all having mass M , indicated on the right side, is obtained as in Figures A.11 and A.12 for the mass spectrometer potentials of set₁₉ (see table A.2). . . . 108
- A.14 Histograms of the depth of ions' flight in the reflectron expressed as a % of Δr , distance between its electrodes R1 and R2 (see Fig. A.3). The frequency distributions were determined with SIMION by letting 75 ions all having mass M , indicated on the right side, propagate through a model of our mass spectrometer. The set₀, set₈, and set₁₆ potentials are assigned in the mass spectrometer. The bin size and vertical range for all histograms are 10 μm and [0, 25] respectively. 109
- A.15 The ions time of flight at the detector, computed analytically with the Eq. A.10 and A.20 are compared with the corresponding values determined using SIMION with the same sets of voltages (of table A.2) and masses. At the top the percent difference ($\% \Delta$) is shown versus potential sets. 110

-
- B.1 Plasma plume development and material detachment produced by a nanosecond laser pulse. The process extends well after the short time during which the laser beam illuminates the material surface. 125
- B.2 Temperature variation of the plasma composition. It has been computed in Matlab by solving the Saha equation which prescribes a thermal equilibrium between neutral Nb atoms and its single and double charged ions. . . . 128
- B.3 As in Figure B.2, the relative abundances of Zn neutral atoms, Zn^+ and Zn^{++} with temperature is shown as computed using Saha eq. B.3. 128
- C.1 Interface of the Labview program we developed in order to drive the SpeX monochromator, through the SpeX compudrive, sampling electric signals with the boxcar. 129
- C.2 Interface of a Visual Basic program written to control the grating position remotely. 141
- C.3 Main interface of a Labview program to adjust NHQ output voltages of either channel A or B. 142
- C.4 Interface of the program that allow us to modify the time settings of the BNC555 and DG535 delay units accordingly. It allow to visualize/adjust the timing of pulses and store the corresponding settings. 144

List of Tables

2.1	According to Fig. 2.2, differences in energy between few electronic levels of ZnO and its anion, are given with corresponding references.	9
4.1	Mass spectrometer distances in inches and cm. The names refer to the nomenclature introduced in Fig A.3.	36
4.2	Delay settings on the DG 535, used in the Indi-scheme. For assigned noble gases, pressures, and geometry these settings grants the best yield of zinc. .	47
4.3	Some example of delays that maximize the intensity of ZnOH and N ₂ for the geometry, gas type and pressures indicated.	47
4.4	Table of the weight loss of a Zn rod determined after N laser light shots with the conditions described in the text.	61
4.5	Experimental conditions used for measurements we performed to characterize the initial kinetic energy of zinc ions (see in the text).	67
A.1	The potentials $V_{k,i}$ corresponding to the mass spectrometer electrodes are identified by the two indexes k, j . The first is associated to the order of the acceleration stage to which the electrode belong, while the second specifies the electrode's rank in the stage.	92
A.2	Potentials values to be applied to the electrodes of the mass spectrometer. They were determined by using the analytical approach described in the preceding text. The aim is to compare the previous prescriptions with the results of SIMION calculations, which should be more accurate dealing with the various physical parameters involved.	102

Chapter 1

Introduction

Zinc oxide is a nontoxic, abundant and thus cheap material. Also used as a catalyst or in solid state devices, it suits a broad range of practical applications, all arising from the unique and many-sided properties of the material. As a wide band semiconductor (with a direct band gap of 3.37 eV), zinc oxide exhibits a remarkable behavior in the visible and in the ultra-violet (UV) spectral regions. The ZnO is transparent to visible light, while in the UV it strongly absorbs the incident radiation. This renders zinc oxide, as an additive in UV-sunscreen products, very appealing.

Zinc oxide is gradually replacing the use of gallium nitride (GaN) in semiconductor devices in UV or blue light emitting diode and in UV lasers due to their similar lattice constants and direct wide band-gap. If used in conjunction with other elements like aluminium (Al) and gallium (Ga), the zinc oxide typical n-type can be enhanced and stabilized. ZnO with a wurtzite structure exhibits naturally an n-type semiconductor behaviour because of a deviation from stoichiometry due to the presence of intrinsic defects such as O vacancies (V_O) and Zn interstitials [3] (Zn_i). It has also been suggested that the n-type conductivity of unintentionally doped ZnO films is only due to hydrogen (H) [4, 5, 6]. Insertions of arsenic (As) or phosphor (P) as has been demonstrated recently [7], causes ZnO to be a p-type semiconductor. It is also promising the use of N, although controversial results were obtained so far [8, 9, 10]. Since, in this case, dopants may be compensated by low-energy native defects, such as Zn_i or V_O and background impurities (H), p-type doping is expected to be far less easy versus n-type.

The availability of ZnO with both p and n-type semiconductor characteristics has as a consequence that p-n junctions based on ZnO could be realized [11], attracting the semiconductor industry's interest. Solid state lasers, based on this technology are therefore expected to fol-

low in future. Lasers with an active volume in the form of a nanotube structure could be realized [12]. Moreover, the possibility to increase zinc oxide conductivity, with a proper doping, allows to have a visible transparent conductive material. This makes doped ZnO to be employed as electrodes in solar cells and in phosphor screens. ZnO is also important in electro-optics as non-linear material for frequency-doubling or as laser medium. Many more relevant aspects of ZnO could be mentioned. The reader is referred for details to the recent and complete review about ZnO materials and devices by Özgür et al. [3]

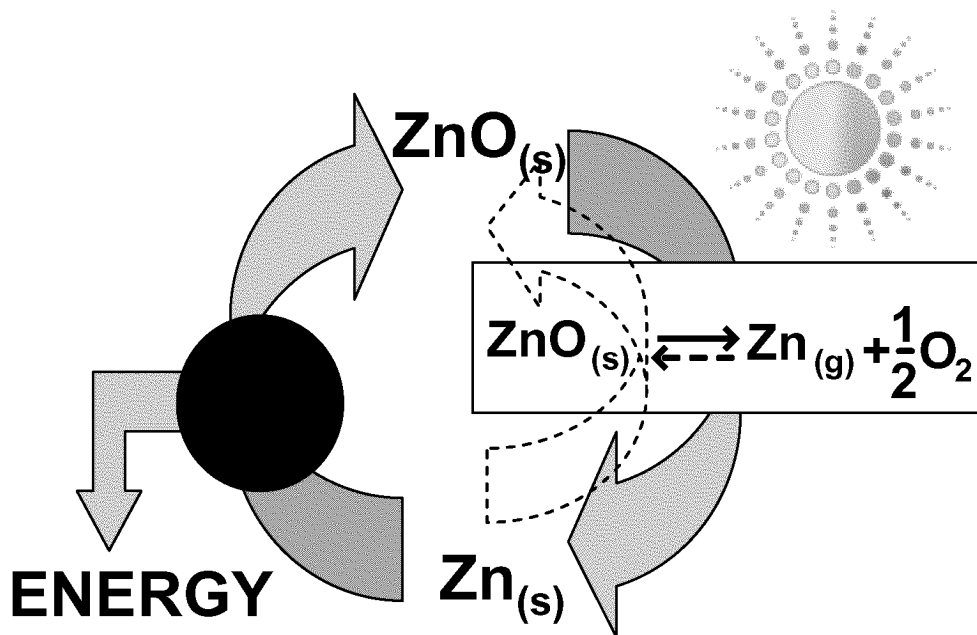
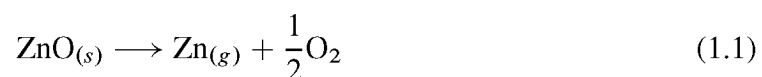


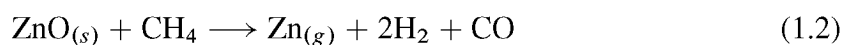
Figure 1.1: In a solar furnace, the concentrated solar energy is used to dissociate ZnO into its components. The zinc-oxygen vapor has to be cooled rapidly in order to avoid recombination to ZnO. The gained zinc represents a mean to store energy.

Metallic zinc could be used to store and transport solar energy. In this context the Laboratory for Solar Technology at PSI investigates the perspectives of the redox-cycle based on Zn/ZnO [13, 14]. The dissociation of $\text{ZnO}_{(s)}$ into its elements at temperatures near 2300 K can be used for the production of metallic Zn in a solar heated furnace. The solar radiation, concentrated by a mirror into a solar reactor, supplies the required process heat for the strongly endothermic [15] reaction to occur (the corresponding energy barrier is shown in Fig. 1.2):

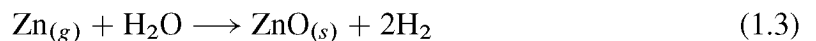


The gaseous products need quenching to avoid that the back reaction to ZnO takes place. The efficiency of the process depends, among others, on up to what extent the oxidation

of the formed zinc (in gas phase or while condensing) can be avoided. The zinc yield will thereby be determined by both the speed of the gaseous species separation and the rate at which $\text{Zn}_{(g)}$ and oxygen recombine to form $\text{ZnO}_{(s)}$ [16]. Combined processes with natural gas (NG) used as reducing species are considered of great interest, since they lower the ZnO/Zn thermal reduction temperature yielding as products both Zn and syngas (a mixture of H_2 and CO which represents a building block for several liquid fuels) [17]. By replacing fossil fuels with concentrated solar energy and combining both the production of Zn and syngas, the overall CO_2 emissions can be reduced substantially respect to the separate processes required. The proposed solar combined process, called "SynMet", can be represented by the overall reaction:



The solid zinc produced might be used to generate electricity in a battery (Zn/Air) or in a fuel cell. It may also be utilized as a reducing agent to produce hydrogen for electricity/heat generation, by reacting with water:



The following is a short survey of some important experimental conclusions drawn by different researchers:

- Mass spectroscopic studies proved that no molecular zinc oxide is formed from $\text{ZnO}_{(s)}$, when heated with or without an excess of oxygen [18, 19, 20, 21]: Exclusively the pathway $2\text{ZnO}_{(s)} \longrightarrow 2\text{Zn}_{(g)} + \text{O}_{2(g)}$ is observed;
- Zinc(g) oxidizes more efficiently to $\text{ZnO}_{(s)}$. $\text{Zn}_{(g)}$ forms if combined with $\text{Ar}/\text{N}_2\text{O}$ than when reacted with O_2 , pure or seeded in argon [22, 23, 15];
- Experimental determinations of the vibrational frequencies corresponding to various electronic states of ZnO are obtained from matrix studies [23, 15]. The results are consistent with photoelectron techniques measurements [2, 24, 25];
- The energy level scheme recently proposed by Bauschlicher et al. [1] is useful to interpret experimental results reported. In particular, the ab-initio calculations performed by Bauschlicher determined that ZnO in its $X^1\Sigma^+$ electronic ground state, formally dissociates into $\text{Zn}(^1S) + \text{O}(^1D)$ atoms. The first electronically excited state $^3\Pi$ is connected to $\text{Zn}(^1S) + \text{O}(^3P)$, atoms in their ground states, as dissociation products;

- Pešić [26] claimed to have identified, in light emission from an arc discharge, bands in the wavelength domain ranging from 520 to 600 nm originating from $\text{ZnO}_{(g)}$;
- The ZnO^- anion has been observed in molecular beams [2, 24, 25].

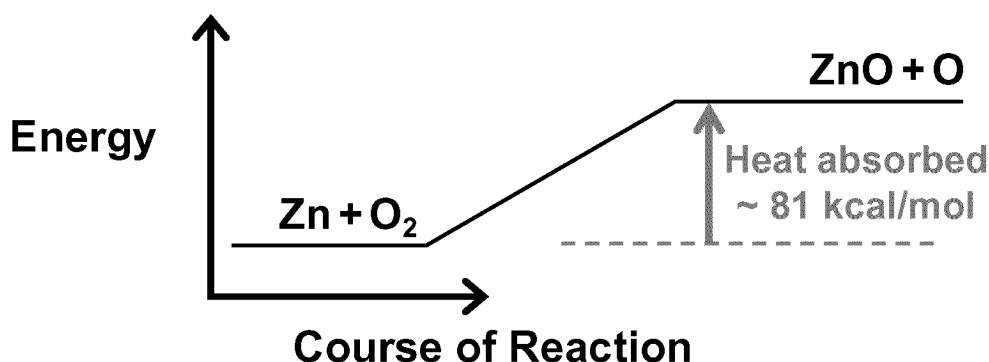


Figure 1.2: Endothermic nature of the reaction between Zn and O: the dissociation energy of O_2 is greater than that of ZnO. Thus, there is an energetic barrier to its formation. This gives a reason for the possible absence of ZnO in gas phase.

The aim of this project was to confirm the existence of neutral diatomic ZnO and Zn dimers (Zn_2) in the gas phase. Though ZnO is known to have a bound ground state, there was up to now no direct proof of its occurrence in the gas phase. In order to elucidate the formation and thermochemistry of molecular zinc oxides we performed molecular beam experiments to produce Zn containing species from their gaseous constituents. In analogy to other investigations of metal oxides, laser ablated zinc is expected to form Zn_xO_y clusters in an oxygen containing atmosphere. Therefore we chose the same experimental techniques to perform mass spectrometric measurements on possibly forming Zn-O compounds.

The bond energy of ZnO was in dispute for quite a time, experiments and theories yielding values from 0.66 eV [27] to 2.8 eV [22]. From thermochemical considerations an up to now accepted dissociation energy of $D_0 \sim 1.61$ eV was inferred for ZnO by Clemmer et al. [22]. Direct evidence for the existence of molecular ZnO has, to our knowledge, only found in Ar and N_2 matrices. The matrices were prepared by deposition of laser ablated zinc reacting with O_2 prior to condensation [15] or by deposition of zinc evaporated in a Knudsen cell together with ozone (O_3). In the latter case ZnO was observed after irradiation with a mercury arc lamp [23].

The occurrence of gaseous monomeric ZnO is still questionable [26, 19, 22] and so is its possible role, besides Zn_2 , as starting point for nucleation. Zn_xO_y clusters in the gas phase were not yet reported. Some information, however, is available about the existence, formation and composition of ZnO nano-structures deposited on surfaces [28]. Theoretical

investigations [29, 30] show that neutral fullerene spheroids of the type $(\text{ZnO})_x$ with $x > 11$ could be stable. Matxain et al. [31] inferred a high stability of two dimensional structures (rhombi, hexagons) of small Zn_iO_i ($i= 1-9$) clusters. In analogy to other investigations of metal oxides laser ablated zinc is expected to form Zn_xO_y clusters in an oxygen containing atmosphere. Ionization mass spectrometry has proven valuable for cluster investigations, since the relative peak intensities in a mass spectrum indicate the cluster stabilities and hence minima in the chemical potential of the observed species. Up to now it could be shown that ZnO cations [21, 32, 33, 34] and anions were formed by laser ablation from a Zn or a ZnO target [24, 25, 2]. Recently, ion cluster formation in UV laser ablation plumes was studied by time of flight spectrometry [35]. However, there is no direct evidence for the production of neutral ZnO [20]. Spectroscopic investigations of a plume ablated from solid ZnO were, in contrast to earlier reports [26, 19], not successful in finding any emission bands clearly attributable to diatomic ZnO [36].

Chapter 2

Review: Evidence for the existence of ZnO in gas phase

The aim of this chapter is to provide a synoptic description of the theoretical results and experimental evidence obtained from previous investigations on diatomic zinc oxide synthesis. Heating $\text{ZnO}_{(s)}$ does not yield Zn_xO_y vapour. Rather, bulk ZnO is found to dissociate into Zn and O_2 . In the gas phase, the reaction $\text{Zn} + \text{O}_2 \rightarrow \text{ZnO} + \text{O}$ was determined to be strongly endothermic ($E \sim 81$ kcal/mol) [15], the dissociation energy of O_2 being greater than that of ZnO. The dissociation energy $D_0(\text{ZnO})$ of the ZnO molecule in its electronic ground state, was derived from theoretical calculations [1] and from experiments with photoelectron spectrometry [25, 2]. The results are in good agreement with the 1.6 eV dissociation energy already experimentally determined previously by Clemmer et al. [22] using a guided ion-beam mass spectrometry.

Table 2.1 summarizes the energies at equilibrium nuclear distance of the four lowest electron states derived by different authors. Figure 2.2 presents a scheme of the lowest four electronic levels.

Data on electronic ground state vibrational levels were reported by Chertihin and Andrews [15]: the corresponding energies were derived from infrared (IR) spectroscopic measurements on ZnO and triatomic ZnO_2 , in the configuration OZnO , stabilized in a matrix. Theoretical models including ab initio calculations were performed by Bauschlicher et al. [1, 27] to describe the ZnO diatomic molecule. The predictions consistently reproduced the electronic and IR findings in the experiments. A list of important experimental observations are summarized in the following:

- Mass spectroscopic studies prove that bulk ZnO decomposes to its elements, when

heated with or without an excess of O_2 [18, 20]. Thermal evaporation of solid zinc oxide it is not a suitable method to get ZnO in gas phase;

- Zinc (g) forms $ZnO_{(s)}$ more readily when combined with Ar/ N_2O than when it reacts with O_2 , pure or seeded in argon [22, 15, 23];

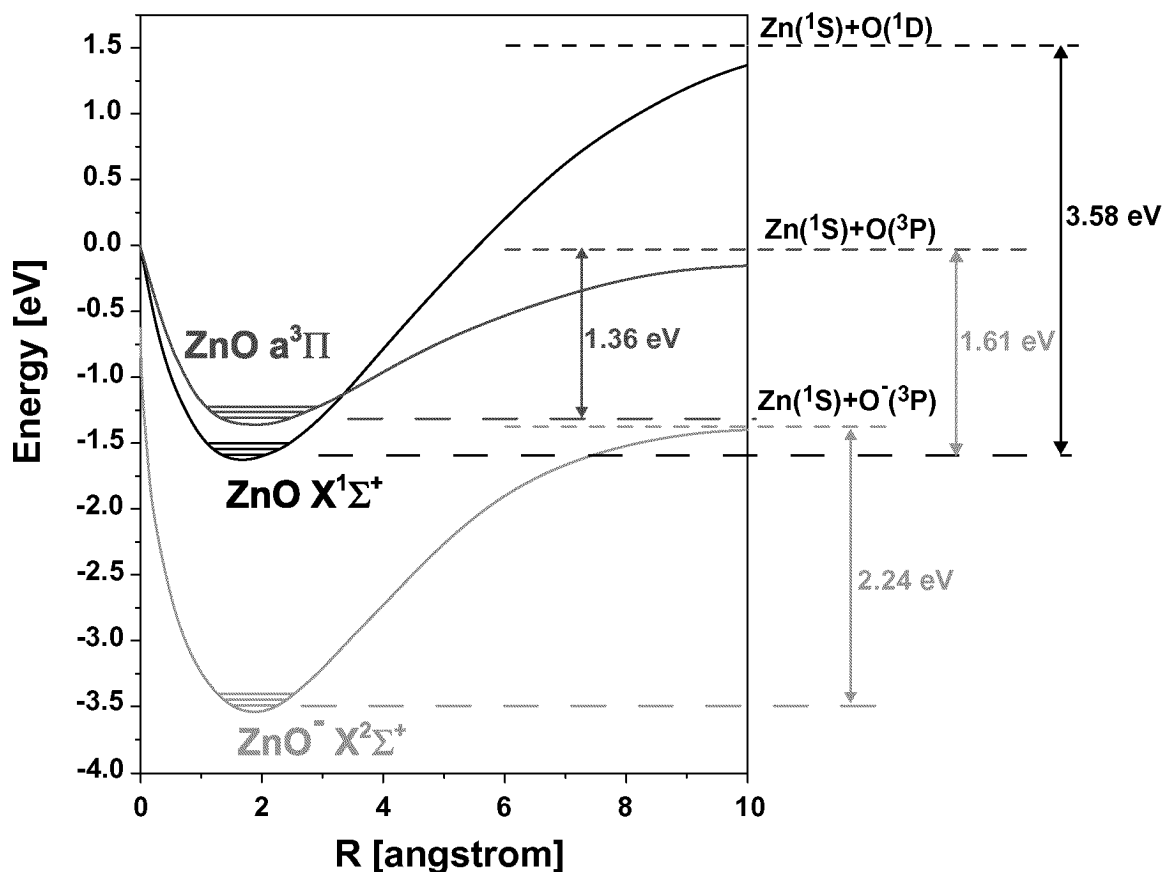


Figure 2.1: Potentials energy curves of the two lowest electronic states of ZnO along with the ZnO anion ground state, all modelled as Morse potentials versus inter-atomic distance using parameters by Bauschlicher [1] and Fancher [2]. For each state is shown the atomic asymptote (left hand side). Differences between the lowest energies values corresponding to the equilibrium internuclear distances (R_0) and the energies of the formal dissociation atoms are indicated.

- Singly ionized Zn radicals react with NO_2 to give $ZnO_{(g)}$ only when the reactants attain kinetic energies above a threshold of ~ 3.4 eV [22];
- The ZnO^- anion can be generated with the setup proposed by Fancher et al. [2] comprising a supersonic expansion ion source. The neutral ZnO molecule appears to be less stable than the anion despite the extra electron that is added to an anti-bonding orbital [24, 2, 1].

Based on these observations, in order to generate ZnO, in gas phase, we attempt to reduce thermal excitation by:

- the use of laser-ablation of solid zinc to evaporate it in a carrier gas;
- generating a molecular beam expanding supersonically into vacuum. During the supersonic expansion a condition is realized in which the molecule gain speed in one direction at the expense of the thermal energy (“freezing” effect).

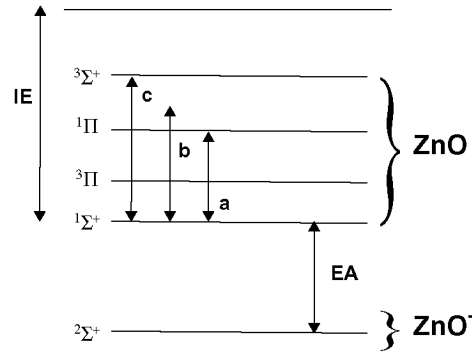


Figure 2.2: The four lowest electronic levels of ZnO and the ZnO⁻ electronic ground state. By photoelectron spectroscopy the lowest energy levels of the 1Σ⁺ - (ground state), the 3Π and the 1Π states could be determined experimentally relative to the stable anion, namely a,b,c, and E.A..

	[1](theor.)	[2]	[25]	[22]
IE[eV]				9.34 (±0.02)
a[eV]	0.26	0.25	0.305	
b[eV]			0.31	
c[eV]	1.26 [27]			
EA[eV]	2.03	2.088	2.077	
D(ZnO)[eV]	1.63			1.61 (±0.04)

Table 2.1: According to Fig. 2.2, differences in energy between few electronic levels of ZnO and its anion, are given with corresponding references.

2.1 The ZnO molecule: observations, computations and characteristics

The nanosecond laser ablation of ZnO is a well-studied subject since the process is mainly used for the production of thin films [36]. The characteristics of the deposited material depend crucially on the properties of the ablation plume i.e. the degree of ionization and

the velocity of the species contained within the plume. Because of this, the plume characteristics have been studied previously by means of mass spectrometry and optical emission spectroscopy. Previous experimental optical studies of the laser-induced plume in vacuum and in ambient gas environments did not show the evidence for ZnO formation. Mass spectrometric measurements from other researchers confirm that zinc, in reaction with an oxygen containing gas mixture, exhibits a rather small inclination to the formation of neutral diatomic ZnO [18, 19, 21].

In 1966 D.S. Pešić claimed to have observed ZnO emission bands between 500 and 600 nm [26] in an arc-spectrograph experiment. In this wavelength region, Pešić measured the emission spectra using a DC arc between zinc electrodes in an oxygen atmosphere. When ^{16}O was substituted with ^{18}O , the most intense bands in the spectra could be correlated to the isotope shift, confirming that the emitting species contained oxygen. Moreover, the spectra acquired when running the arc in an atmosphere of Ar, N_2 , H_2 , and H_2O did not show any of the features observed before in oxygen. This was interpreted as proof that Zn_2 , ZnN , ZnH , and ZnOH are not emitters for the measured spectral bands. However, to date, no other researchers have been able to confirm the spectral observations reported by Pešić, thus raising doubts about the correct identification of the emitting species [19].

B.G. Wicke [19], in 1983, studied the dynamics of the chemiluminescent oxidation of zinc atoms by N_2O to form electronically excited ZnO (denoted in the following text as ZnO^*). The heat of a pulsed laser, when focused on a zinc film, forms zinc atoms in a dense cloud expanding into vacuum through a molecular beam apparatus. The chemiluminescence produced by the chemical reaction $\text{Zn} + \text{N}_2\text{O} \rightarrow \text{ZnO}^* + \text{N}_2$ was monitored with a photomultiplier while a quadrupole mass spectrometer recorded the mass species in the molecular beam. The qualitative evidence for the reaction yielding ZnO as the source of the chemiluminescent emission was thus obtained from the mass spectrometer. By the analysis of the chemiluminescent reaction cross section the lower value for the dissociation energy was derived to be $2.8(\pm 0.2)$ eV. The cross section of ZnO reaction increased with increasing kinetic energy of the reactants, more rapidly for energies above 2.5 eV. Particularly, ZnO formation was significantly enhanced by small amounts of thermal energy added to the N_2O by heating it rather than supplying Zn with the same amount of kinetic energy.

The weakness of the chemiluminescent signal did not allow for dispersion of its spectrum but the wavelength region of the emission was found consistent with the observations by Pešić.

The first determination of the bond and ionization energies (IE) of neutral ZnO was reported by D.E. Clemmer et al. [22] in 1991. This was achieved by characterizing the kinetic energy dependence of the reaction of Zn^+ with NO_2 using ion-beam techniques. Zinc ground state ions were produced either by electron impact ionization of zinc vapour or by Ar-ion impact on a solid zinc surface. The ions were mass selected prior to being slowed down to the desired kinetic energy. The ions entered a NO_2 containing cell where the pressure chosen was low enough that multiple collisions were minimal. The products of the reactions as well as the unreacted beam were detected in a quadrupole mass analyzer when leaving the gas cell. The value obtained for the ZnO bond energy ($D_0(\text{ZnO}) = 1.61 (\pm 0.04) \text{ eV}$) is similar to the one experimentally found in 1990 by E.R. Fisher et al. [37] for ZnO^+ . The reduced capacity of Zn^+ to form an ionic bond with O_2 is balanced by the electron promotion required for Zn to form covalent bonds [27]. The $\text{IE}(\text{ZnO})$ was determined by Clemmer to be $9.34 (\pm 0.02) \text{ eV}$.

The values for $\text{IE}(\text{NO}_2)$ and $D_0(\text{ZnO}^+)$ could also be derived and turned out to be consistent with the findings from previous researches [37, 38].

In 1993, L.R. Watson et al. [20] performed a high temperature mass spectrometric study to determine the bond energy of ZnO. The goal was to solve the contradiction among previous experimental findings for this value [22, 19]. The reaction



was studied with an ion detection system. A magnetic sector mass spectrometer analyzed the neutral molecular beam effusing from a inductively heated cell containing $\text{ZnO}_{(s)}$. At the entrance of the mass spectrometer the molecular beam entered a region in which ions were produced by electron-impact. The ZnO detection limit of the apparatus was of $2.6 \times 10^{-10} \text{ atm}$. The yield of species was determined as a function of the cell temperature ranging from 1400 K to 1700 K. An O_2 flow was added in the cell in order to favor the term on the right hand side of the reaction 2.1. However no $\text{ZnO}_{(g)}$ was observed. This result together with the derived detection limits, allow the determination of an upper limit for the dissociation energy ($D_0(\text{ZnO}) \leq 2.3 \text{ eV}$). This is consistent not only with the previous derivation by Clemmer et al. [22] but also with the ab-initio calculation performed earlier by Bauschlicher [27].

The laser desorption and ionization of a matrix of ZnO in lithium borate was investigated with a mass spectrometer by S.W. Hunsucker [39] in 2001. The ZnO concentration by weight was of 9.2%. They used a frequency tripled Nd:YAG laser (355 nm) providing a pulse energy maximum of 3 mJ. In the measured spectrum, after having subtracted the background, only the peaks corresponding to the major isotopes of zinc were seen. A peak visible in the spectrum at 128 Da was attributed to Zn_2^+ . Lower values of laser pulse energies resulted in no detectable traces of Zn. A pressed pellet of ZnO was also analyzed using the same experimental setup. The resulting mass spectrum exhibited series of peaks that could be assigned to Zn^+ , $(\text{ZnO})^+$, Zn_2^+ , $(\text{Zn}_2\text{O})^+$, $(\text{Zn}_2\text{O}_2)^+$, and Zn_3^+ . The metal peaks (eg. Zn and Zn_2) were more intense than those of their respective oxides.

The reaction products of the laser ablation of zinc in an atmosphere of O_2 (or N_2O), trapped in argon or nitrogen matrixes, were studied with infrared spectroscopic techniques by Chertihin and Andrews [15] in 1997. The wavelengths region of interest extended from 11.1 μm to 22.2 μm . The infrared absorption of zinc compounds embedded in the matrices was measured depending on the matrix temperature in the interval between 10 and 30 K. Oxygen isotopic substitution was performed for the identification of the products. A signal attributed to ZnO was observed in solid Argon, which could be confirmed by the oxygen isotopic shift analysis. A Raman fundamental value of 769 cm^{-1} for the ZnO resonance was derived from the strong absorption band observed in this region. A fundamental of $780(\pm 10)\text{ cm}^{-1}$ could be inferred for ZnO in the gas phase from the matrix vibronic resonance.

A previous spectroscopic investigation of matrices produced by the thermal reaction of Zn and O_3 in an excess of Ar at 15 K was reported earlier by Prochaska and Andrews [23] in 1980. They had already found the absorption bands around 769 cm^{-1} , which they assigned to ZnO vibration. The signal enhancement in the resonance Raman spectra was attributed to the predicted optical absorption in the 530 nm region, in accordance with the ZnO chemiluminescence observed by Wicke [19].

In 1998, R.E. Leuchtner [21] investigated species produced in the plume from solid ZnO ablated with a laser. The masses, charges and kinetic energies of the species in the plume were determined by time of flight mass spectrometry and photo-ionization techniques. The

248 nm output beam of a KrF laser with fluences varying over the range $0.2 - 2.5 \text{ J/cm}^2$ was used for the ablation. Neutral species were ionized either by electron impact, field ionization, or photoionization with the second harmonic (532 nm) output beam of a Nd:YAG laser. A quadrupole mass analyzer was adopted. Only Zn and O, both, as neutrals and ionized, together with Zn^{++} , could be detected. The analysis of the kinetic energies of species in the ablation plume suggested that electron ejection mechanisms are likely to be involved. Over a fluence energy threshold of 0.7 eV the electron-ion recombination was substantial. Zn^+ and the doubly ionized zinc, whose presence was finally reproducible, recombined with ambient electrons to form metastable particles.

Fancher et al. [2], in 1998, reported about their photoelectron spectroscopic study of ZnO^- . Anions of ZnO were produced in a hot supersonic expansion ion source. It comprised an oven where Zn was continuously evaporated at 650°C expanding through a $125 \mu\text{m}$ nozzle orifice with 270-400 mbar argon (Ar). In the region outside the nozzle an effusive flow of N_2O was present. The electrons were produced by a filament which intercepted the expanding jet producing 20-30 pA of ZnO^- for an electron current of 10 mA. An axial magnetic field directed the anions towards a detector. The vibronic features they could observe in the photoelectron spectrum of the ZnO anion provided information about the neutral ZnO, allowing to determine the adiabatic electron affinity of zinc oxide ($EA(\text{ZnO}) = 2.088(\pm 0.010) \text{ eV}$). This value together with the oxygen electron affinity (1.46 eV) and the experimental value of $D^0(\text{ZnO})$ determined earlier by Clemmer et al. [22], allowed to compute also $D^0(\text{ZnO}^-)$. A Franck-Condon analysis of the ZnO^- photoelectron spectrum was conducted with electronic potential curves for both anion and neutral ZnO modeled as Morse oscillators. The analysis rapidly converged to give a simulated spectrum that fitted the experimental one rather well. To achieve the best fit the researchers used the experimental results for the vibrational energy from Prochaska et al. [23] and estimated the anharmonicity by using the value of the CaO molecule (4.8 cm^{-1}). For ZnO^- , the hot band vibrational spacing derived from the spectrum at low electron binding energies was given as input for vibrational frequency and in this case the anharmonicity of GaO (6.24 cm^{-1}) was used. As result of the analysis a change of the bond length between the anion and the neutral ZnO, (0.07 \AA) and the best fit vibrational frequencies $625(\pm 40) \text{ cm}^{-1}$ and $805(\pm 40) \text{ cm}^{-1}$, respectively, could be determined.

More recently, in 2000, the investigations by M.L. Campbell et al. [40] on the reactivity of N_2O with Zn and other transition elements in gas phase were reported. Atoms of Zn were generated by the 248 nm photodissociation of a precursor ($Zn(TMHD)_2$) using the output of an excimer laser. Where TMHD indicates 2,2,6,6-tetramethyl-3,5-heptanedione, the ligand used for the precursor synthesis. The transition metal atoms together with N_2O were entrained in N_2 and admitted into a reaction chamber through calibrated mass flow controllers. The evolution of the reaction was analyzed by performing laser induced fluorescence (LIF) measurements in the chamber for the time preceding and following the occurrence of a photolysis pulse, as a function of temperature and pressure. For temperatures up to 623 K the reaction was extremely slow and an upper limit for the rate constant was estimated to be $1 \times 10^{-16} \text{ molecules}^{-1}\text{cm}^3\text{s}^{-1}$. Correspondingly, the minimum activation energy was derived to be 0.67 eV.

Because their fit provided a poor description of the experimental spectrum for low electron binding energies, the features observed were tentatively attributed to photo-detachment transitions to the first (electronic) excited state, $^3\Pi$, according to theoretical computations by Bauschlicher [1]. The corresponding molecular constants were found to be consistent with the recent theoretical derivation [1].

The difference in electronegativity of unlike atoms in a compound is a measure of their competitive attitude to attract electrons. Expressed by a non-dimensional number, the electronegativity depends on the scale chosen [41]. According to Pauling's description of bonding, the electronegativity difference determines the variation of bond energy from the average energy of the corresponding homo-atomic bonds [42].

In the scale proposed by Pauling, the electro-negativity difference between Zn and O exceeds a value of 1.7, considered by many researchers to be a threshold for the estimation of the relative ionic contributions in hetero-atomic bonds, as reviewed by G. Sproul [43]. For non-transition elements, such a value is often found to be associated with more than 50% ionic bonding forces. It is known that methods based on molecular mechanics are much less efficient in describing ionic molecules than quantum-mechanical techniques. Therefore a serious attempt to analyze the structure of ZnO should be performed with an ab-initio approach. Such calculations were accomplished by Bauschlicher [27, 1] and yield results which are in agreement with recent experiments [25, 24, 2, 22]. The principal problem with first row transition metal monoxides results from the presence of many unpaired electrons, which produce a number of low-lying electronic states. The

description of the molecule can also be obtained with semi-empirical approaches which involve approximations in the molecular computation. For this reason, they do not always allow a definite assignment of one of these states to be the ground state [44].

In 1986 Bauschlicher and Longhoff [27] found with ab initio calculations the state $^1\Sigma^+$ to be the ground state and determined the first excited electronic state $^3\Pi$ to be extremely low lying. The ZnO description given by Bauschlicher and Longhoff [27] resulted to be inconsistent with recent experimental findings by Fancher [2]. In particular the proposed ZnO model prescribed that the extra electron in the singly charged ZnO anion occupies an anti-bonding orbital, contradicting the experimental evidence $D^0(\text{ZnO}^-) > D^0(\text{ZnO})$. Therefore new ab initio calculations were performed by Bauschlicher and Partridge [1] in order to attain a more accurate description. Results were also derived using density functional theory (DFT) for a comparison.

From the new ab initio computations they could infer based on symmetry considerations that the ZnO molecule in its electronic ground state, $X^1\Sigma^+$, does not dissociate formally to the atoms in their ground states. An extensive contribution of the heterolytic state, $B^1\Sigma^+$, which correlates to Zn^+ and O^- asymptote is assumed to lower the $^1\Sigma^+$ potential energy curve below the $^3\Pi$ energy potential. This makes the $^1\Sigma^+$ state the ground state even if, as illustrated in Fig. 2.1, the state $^3\Pi$ dissociates to its ground-state atoms [1] and gives to ZnO a 3.58 eV dissociation energy in its ground state that exceeds the one corresponding to ZnO^- (2.2 eV).

In 2001, first Kim et al. [25] and then Moravec et al. [24] reported about their photoelectron spectroscopic investigations on ZnO^- generated in a pulsed molecular beam. A laser ablation source produced zinc vapor using a 10–15 mJ/pulse from a second harmonic output of a Nd:YAG laser, operated at 30 Hz, impinging on a rotating and translating Zn rod. The zinc was entrained in the helium seeded with O_2 coming from a pulsed valve prior to expansion into vacuum through a 20 mm long nozzle having a 3 mm diameter nozzle. The skimmed anions were separated according to their mass in a 1.2 m mass spectrometer before being selectively photo-detached. The neutral resulting from the photo-detachment by applying a repulsive field in front of the ion detector was observed to monitor the source fluctuations. The photo-electrons were accelerated for detection towards a second MCP.

Particularly interesting are the results by Moravec et al. [24]. By varying the polarization of the light beam used for the electron detachment they were able to argue about the atomic

orbitals involved according to symmetry considerations. This investigation offered insights to the first 4 electronic states of ZnO. In addition a band of weak intensity, visible at low electron binding energy, could be assigned to the electronic transition $a^3\Pi + e^- \leftarrow A^2\Pi$, determining for the excited anion state a $0.72(\pm 0.08)$ term energy. The Franck-Condon analysis led to a substantial confirmation of the predicted trends for both, the bond lengths and vibrational frequencies of ZnO and ZnO⁻.

Chapter 3

Project Aim

Vaporization and dissociation mechanisms of zinc oxides are not yet fully understood, despite the fact that ZnO is broadly used. The full electronic spectrum of diatomic ZnO is still unknown though photo-electron techniques recently revealed the map of the three lowest states in accordance with theoretical predictions [24, 25]. Spectroscopic experiments must therefore deal with a difficult search of the lines in a large range of wavelengths unless a reduction of the spectral region under investigation could be derived by other methods.

3.1 Objective

The aim of this project is to suggest under which condition $\text{Zn}_{(g)}$ and O_2 react to form $\text{ZnO}_{(g)}$. Identification of some reactions that lead to $\text{ZnO}_{(g)}$ formation.

3.2 Procedure, Tasks

In order to gain some insight we developed a spectrometric setup, comprising a ToF spectrometer. It allowed us to characterize the species produced under “cold conditions”, with a molecular beam, while a complementary project in another group, was analyzing the kinetics of the Zn reoxidation in hot condition.

3.3 Realization

Laser vaporization techniques allowed us to have high yield of zinc without having to heat up the system. The very cold conditions that are usually obtained at the entrance of the mass spectrometer help stabilizing the species formed in the molecular beam. The pro-

duced molecules (which have their thermal energy reduced and converted to kinetic energy along a specific direction) can reach the detector before they dissociate. Different oxygen containing species that could react with zinc to form ZnO compounds were used. They were introduced in the experimental setup seeded in a noble gas. Their concentrations as well as the type of noble gas were varied to determine the advantages of particular combinations. Zinc exhibits a characteristic isotopic pattern what can simplify the identification of Zn containing compounds: it has five stable isotopes with natural abundances 48.6% (M=63.929 Da, ^{64}Zn), 27.9% (M=65.926 Da, ^{66}Zn), 4.1% (M=66.927 Da, ^{67}Zn), 1.9% (M=67.925 Da, ^{68}Zn), 0.6% (M=69.925 Da, ^{70}Zn) respectively.

3.4 Accompanying investigation

In parallel to the research described here the oxidation kinetics of hot zinc vapours is investigated by PSI's Laboratory for Solar Technology. The aim is to quantitatively characterize the rate of zinc oxidation in conditions similar to the ones at the exit of a solar reactor. The two projects were thought to provide all together experimental observations on molecular ZnO formation in hot and cold conditions (sharing instruments and information). A detailed description of the setup used by Solar Technology can be found in [45]. The main characteristics are shortly recalled in this section. The setup, called REKIN, is based on a coaxial jet where a flow of zinc vapour optionally diluted with an inert gas is confined in a hot stream of oxygen (also mixed with inert gas at will). The confined coaxial jet is implemented using a system of two concentric nozzles. The gases can be preheated up to 1000 K. Varying the gas temperature before expansion and the geometry of the nozzles allow to control whether only zinc atoms or also droplets will participate in the reaction with oxygen. The exact geometry of the nozzles determines if a laminar flow or a turbulent mixing can be established. A two-dimensional laser-light-sheet intercepts the jet stream to probe the flow field, spatially resolved, with a planar laser induced fluorescence (PLIF) technique. In 2004, the mixing behavior in the flows at different experimental conditions could be determined by PLIF experiments carried out at room temperature with acetone as a tracer [46]. The experiments with zinc were planned to be conducted with a oxygen temperature close to the maximum achievable with the gas heating system. Due to a failure of the heating system, experiments on ZnO formation in gas phase were delayed. However, since then, an extensive characterization of the REKIN nozzle at room tempera-

ture by Computational Fluid Dynamics (CFD) and Particle Image Velocimetry (PIV), was performed in cooperation with the Fachhochschule Aargau. Results are not yet published though. New experiments with zinc using the REKIN setup are planned to be carried out soon, as the problems with the heating system will be solved. Currently work is in progress to describe the oxidation/condensation of zinc vapor and oxygen using the generic model on the aerosol formation, suitably adapted.

Chapter 4

Experimental setup

4.1 Setup function and components

The experiments up to now have shown the difficulties involved in the production of zinc oxide in gas phase with a substantial density. As yet, no appropriate device has been designed for the production of dense zinc vapor and its reaction with oxygen.

Laser vaporization sources have been successfully employed to investigate various metal oxides [47, 48, 49, 50, 51]. They are often used in combination with a supersonic expansion technique to provide intense molecular/cluster beams with practically all metals. The target material is ablated and seeded into a flowing stream of inert gas expanding into vacuum from a small nozzle. Rarefaction and the adiabatic cooling of the gas mixture steeply reduces the collision rate experienced by beam components as a function of distance from the expansion source. A simple model, which describes the molecular beams produced by a supersonic expansion of a binary gas mixture with one component diluted, was presented in 1993 by DePaul et al. [52].

Weakly bound complexes and clusters are formed if sufficient collisions occur before the beam becomes too rarefied and further interactions among the contained chemical species are hardly possible. Molecules produced initially are entrained with the expanding gas. They lose internal energy by collisions during expansion [53]. Depending on how much internal energy the molecules lose, they either stabilize or dissociate. At the same time, the probability of further collisions drops off.

A schematic drawing of the experimental apparatus realized for our experiments is shown in Figure 4.1. A gas mixture containing a small addition of an oxygen donor to a noble gas is introduced with high (up to 6 bar) backing pressures into a vacuum chamber by a

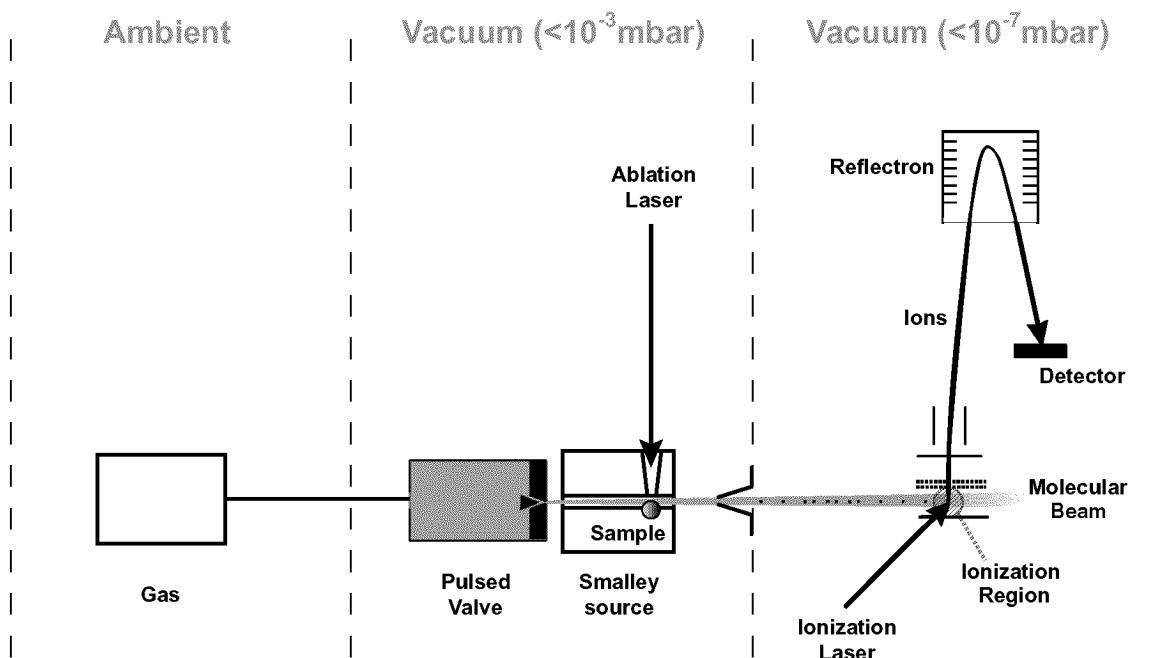


Figure 4.1: Sketch of the actual experimental setup.

pulsed valve. For maintenance of a high vacuum into which the gases can expand, huge pumping rates are necessary. Pulsing the valve reduces the size of the vacuum pumping system required, by limiting the total gas throughput. Still, during the gas pulse, high densities can be established close to the valve nozzle enabling high reaction rates. Before expansion metal vapour has to be added to the gas stream. Metal vapour can be produced by heating up a solid sample to a temperature providing an adequate vapour pressure or by ablating material from a surface. Ablation of the target material from a solid body is most elegantly performed with laser light focused to a small spot. The laser beam impinges on the material surface which gets hot and starts to evaporate and is sputtered off. Laser ablation process produces dense vapours at very high temperatures in an expanding plasma plume that crosses the gas stream path. High vapour temperatures are adverse to molecule formation. However, the hot metal plume rapidly mixes with the carrier gas resulting in temperatures at which chemical species may associate.

The buffer gas density can be varied to maximize the cooling efficiency of the plume and achieve an optimal cooling and stabilization effect on expansion.

A vaporization source based on a Smalley design [54, 55, 56] was realized and used to evaporate Zn into a gas stream. The zinc vapour, entrained in the gas flow, expands into vacuum through a nozzle. The length of the source exit channel, also called mixing region

or “waiting room”, could be chosen long enough so that many three-body collisions can occur that, in turn, favor cluster formation [57].

As a rule, one observes more heavy complexes the longer the transit time in the mixing region lasts. The carrier gas containing clusters eventually proceeds downstream and rarefies on expansion up to a point where no more collisions occur. At this point, the molecular beam is skimmed from the expansion cloud by a diaphragm. This collimated beam of molecules then enters the interaction (ionization) region of a time of flight mass spectrometer (ToF-MS). In this region, the output from a second laser ionizes specific chemical compounds contained in the molecular beam. Ions formed are guided to a detector by electric fields along the mass spectrometer.

The molecular beam apparatus in its present configuration consists of two stainless steel cylinders. As depicted in Fig. 4.2 we refer to these cylinders as “source” and “detection” chambers respectively, since both vaporization and ionization occur in the “source” and charged molecules are detected in the latter.

The source chamber is the one with the largest volume of ~ 21 liters. It has 10 ports of access with various sizes. Two pairs of ports with flanges on opposite sides and diameters of DN 160 ISO-LF are available. The ports of one of these pairs are closed with DN160 flanges having 40 mm diameter fused silica windows. The ionization light of a laser crosses the chamber passing through these windows. The ablation laser light is passed through two other DN 40 ISO-KF ports, also fitted with fused silica windows. The ablation laser beam propagates parallel to the ionization beam, at a distance of ~ 135 mm. In the source chamber, through the top port, the vaporization source is connected to the solenoid valve.

The 4-ports detection chamber has a volume of ~ 15 liters. The smallest port, with flange KF63, is located at the top side of the chamber and hosts a vacuum gauge. Located at the opposing side a second port ends with a flange CF100 and is used for attaching a vacuum pump. The remaining two ports are terminated with ISO-CF DN160 flanges. One of them is used to fasten the detection chamber to a ISO-LF DN250 flange of the source chamber, while the port corresponding to the other DN160 flange is sealed vacuum tight with a blind flange. The detection chamber houses a reflectron and two micro-channel plate (MCP) ion detectors, as described below.

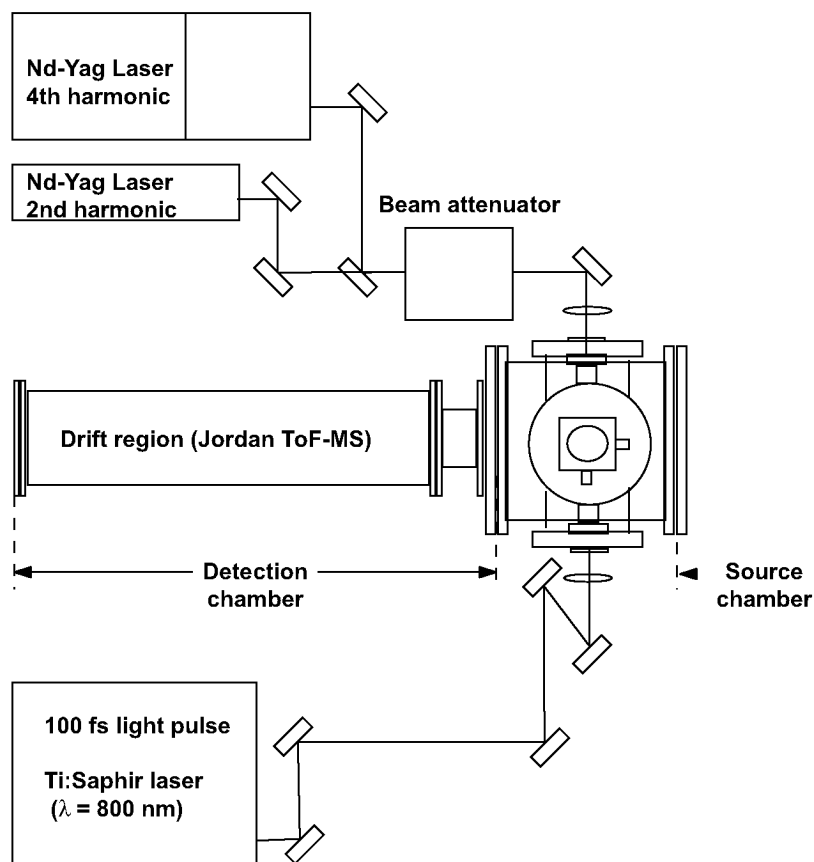


Figure 4.2: Schematic top view of the experimental setup. It comprises a source and a detection chamber. The laser light paths and the optical table are also sketched. The 4th and 2nd harmonic output beams generated by two distinct Nd-Yag lasers are alternatively used for material ablation. The 4th laser beam serves also for the ionization during a calibration procedure. In all other measurements the output beam of a femtosecond laser system ionizes the molecules for the mass spectrometric detection.

4.2 The Molecular Beam Apparatus

Since the 1920s [58] atomic and molecular beams have been used in spectroscopic investigations. These beams are also termed "effusive" beams [59] when the constituent particles act as individuals with the number of collisions reduced almost to zero. A collision-less beam of molecules is obtained if the orifice size is small enough such that $D \ll \lambda_0$, where D is the diameter of the circular orifice and λ_0 is the mean free path of the gas at pressure P_b , which is the backing pressure of the gas reservoir [60]. In 1951 Kantrowitz and Grey published a theoretical description of a proposed supersonic jet as a molecular beam source [61]. While their original goal was to increase the beam intensity, they noted that

their source would produce a cooling of the translational and internal degrees of freedom of the molecules in the beam. The main feature of Kantrowitz and Grey's proposal was the reversal of the inequality noted above with respect to the nozzle diameter and the mean free path. If $D \gg \lambda_0$, there could be many collisions as the gas flows through the orifice and through the expansion region downstream from the orifice. This hydrodynamic flow condition converts the enthalpy associated with random atomic motions into directed mass flow, causing the mass flow velocity u to increase [60]. It is this conversion of random motion to directed mass flow which causes the temperature to decrease. Other thermodynamic quantities are affected by this process, for example, the classical speed of sound, c , defined as

$$c = \left(\frac{\gamma K_B T}{m} \right)^{1/2} \quad (4.1)$$

where $\gamma = C_p/C_v$ is the heat capacity ratio, K_B is the Boltzmann constant, T is temperature, and m is the particle mass. Since c is proportional to $T^{1/2}$, the local speed of sound decreases during the expansion process, and the Mach number ($M = u/c$) increases. In an ideal expansion $M = 1$ for the most constricted point in the nozzle, but with additional expansion M can get greater than one [60]. If $M > 1$, the supersonic flow regime is reached, and it is this regime in which our present apparatus functions. The core of the expansion (the so-called "zone of silence") is the active region for downstream experiments. Skimmers are frequently employed to separate the cold core of the beam from the hot shock wave which defines the outer envelope of the expansion. In our case a conical skimmer with a 1 mm diameter orifice separates the source and detection chambers, where the detection chamber remains at hundred times lower pressure than the source chamber. In a conically skimmed beam, internal relaxation freezes and the molecular flow regime dominates, thereby minimizing multi-body collisions that would lead to molecular cluster formation [62]. Since the expansion process is dependent on the properties of the gas involved, it is observed that heavier gases are more likely to form clusters, as they get rid of the internal energy per collision more efficiently. Early experiments carried out suggest that using Ar as a carrier gas is much more likely to promote cluster formation than He.

4.2.1 Pulsed Valve

A two-way solenoid valve (Series 9, DC 28 V, Parker Hannifin Corp.) is the basis of our source design. The valve consists of a magnetically actuated poppet-and-spring mechanism

which opens very fast and closes vacuum tight after a very short opening time. The minimum time for opening and closing is about $160 \mu\text{s}$ with very good repeatability up to speeds of about 120 Hz. A schematic drawing of the valve is shown in Figure 4.3. A solenoid coil is incorporated in the valve body and a voltage difference can be applied to its terminal to energize it. The plunger consists of a magnetic material. A teflon poppet provides the vacuum tight seal. Both plunger and poppet have a cylindrical shape. The

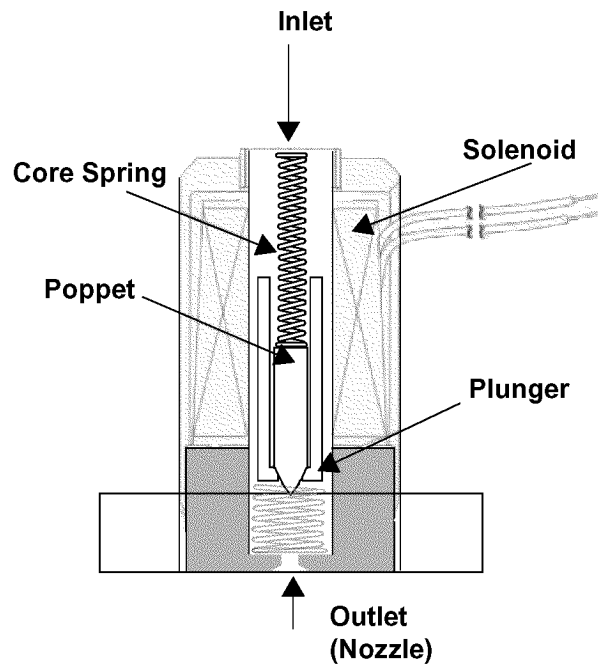


Figure 4.3: Front end of the solenoid valve, Series Iota One, used in our experimental set up.

poppet is installed within the plunger, and their main axes are coaxial with the valve. The opposing forces of two springs make the poppet and the plunger move together as a single unit. The poppet is pushed by a core spring towards the bottom of the plunger, while an auxiliary spring presses on the latter in the opposite direction.

In the de-energized condition, the core spring, assisted by the gas pressure, holds the valve seal on the valve seat and shuts off the flow, by clogging the nozzle orifice of the valve. A nozzle diameter of 1 mm was used. When energized, the core and seal are pulled into the solenoid coil and the valve opens. Voltage differences of few tens of volts make the electro-magnetic force acting on the plunger exceed the combined forces of the spring and the pressure of the gas medium.

In general, the softer the poppet material, the more likely it is to deform over time. Yet, a soft poppet, at the beginning of its life cycle, is more likely to form a better seal. The

harder poppets deform less, but they provide a poor seal with high backing pressures. The poppet material is teflon, which offers good durability and sealing ability, although the poppet must be replaced after about 20 – 24 hours of use. A leaking poppet manifests itself with a greatly increased count of ions in the mass-spectrometer and is therefore associated with a strong degradation of any type of ion signal collected. Large oscillations in the ion gauge readings of source chamber pressure may also eventually appear.

After some time of use a black powder was observed inside the solenoid body that holds the poppet in place. The accumulating powder can compromise the seal of the valve and regular interventions must be scheduled in order to check if the poppet needs replacing. The source of the powder is not clear.

A pulse driver system (IOTA ONE) controls the valve opening and shut off. This unit can be triggered both internally or externally (also in single shot mode) via a TTL pulse. It allows for valve opening times ranging from few hundred microseconds to minutes and the delay between triggering and effective opening of the valve can be adjusted too.

4.2.2 Laser Vaporization

The principle of a laser ablation setup that produces metal vapour plumes with acceptable reproducibility is illustrated in Fig. 4.4. According to Smalley [54], a metal can efficiently be vaporized out of its surface into a gas stream with a laser. To avoid that the crater formed by laser interaction digs deeper into the material from shot to shot, thereby changing the shape of the plume of ejected material, a fresh portion of the surface has to be used for every laser light pulse. This can be achieved using a rod of the material under investigation that revolves around and translates up or down along its cylindrical symmetry axis. A schematic drawing of the design we adopted for the vaporization source is shown in Fig. 4.5. Our goal was to realize a versatile source that could be easily modified. The source is placed within a vacuum chamber where a pulsed laser is used to ablate material from the target surface of a rod. The rod moves inside a stainless steel block containing bores in a way that the plume of ablated material is confined within a 2.5 mm diameter bore from where it is blown out into vacuum by a carrier gas.

In typical operation the rod movements are continuous so that the laser light impinging

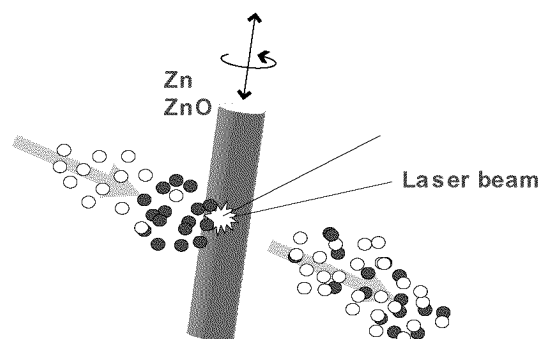


Figure 4.4: A focused laser beam impinges on a zinc/zinc oxide rod that revolves around and translates up and down along its cylindrical symmetry axis. The plume formed is entrained in a noble gas pulse, optionally mixed with oxygen donor molecules.

on its surface hits a different spot on every shot. The rod is actuated by a DC-mini-motor (Series 15A, Faulhaber) that has very compact dimensions (max diameter=16 mm, height=60 mm) and a negligible outgassing. It is installed within the vacuum environment, with a tubular motor holder (H) attached to the main source piece (S), as shown in Fig. 4.5. We wanted to avoid an external motor and a rotary feedthrough to move the metal target inside the vacuum vessel. The mini-motor is coaxially mounted with the sample rod. The holder (H) simplifies the source to be serviced by making the motor easier to be dismantled. The geometry of the main body (S) of the source can be modified to optimize the efficiency of the source. Motor drive and ancillary adaptors for changing the bore diameters can be retrofitted into the main body. A tool similar to a screw-driver is connected to the motor shaft and acts on a threaded nut which holds the zinc rod. The nut runs with a 15 turn/cm pitch through a thread inside the motor holder. When the motor runs, the screw driver rotates at a constant rate of 0.5 rpm and the nut with the attached rod is thus screwed up or down along the cylindrical axis of symmetry of the motor holder.

Two different designs for the main source block (S) of the ablation source were implemented.

In both cases, the stainless steel block has overall dimensions 40 mm × 40 mm × 30 mm. Two identical metal slabs (12.5 mm × 40 mm × 3 mm) extend the area of the block face which has to be placed frontally to the valve. Each slab has a bore. The main block of the source is fastened, together with the valve, to a common support via a pair of screws. In both geometries the main block is characterized by a 30 mm through-hole crossing the center of the block. When the block is fastened to the support, the axis of the bore is collinear with the one of the valve. Because this bore extends the path of the gas introduced by the valve, we sometimes refer to it as the “gas channel”. The 1 mm output nozzle of the

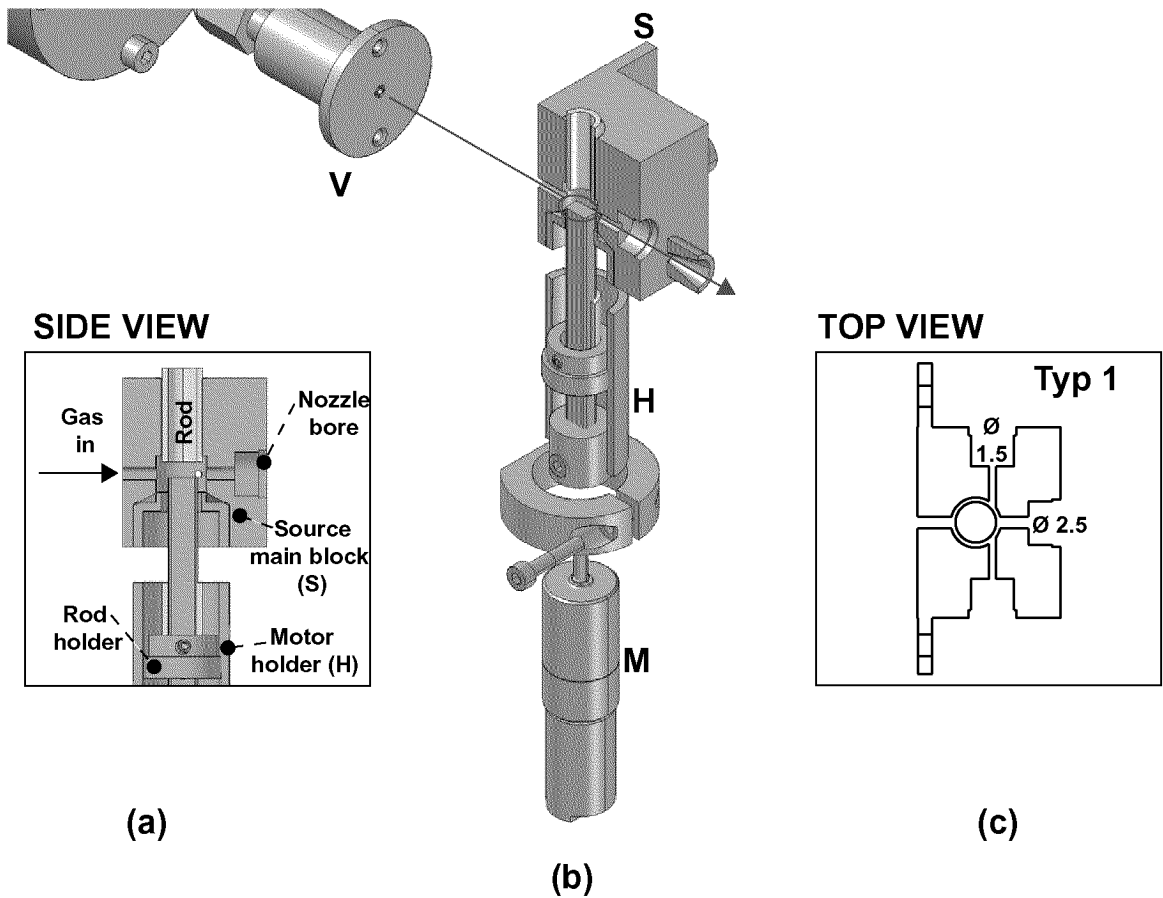


Figure 4.5: Sketches of the vaporization source with the first design of the main piece (S) (Typ 1). (b) Three dimensional drawing with a cutaway showing a cross section of the vaporization source comprising the main piece (S) and the motor holder (H). The pulsed valve (V) and the mini-motor (M) are also shown. The insets (a) and (c) illustrate respectively a side and a top view (Typ 1) of the vaporization source mid sections.

valve is surrounded by a Viton o-ring which seals the joint between the vaporization source and the valve against the vacuum. Hence the gas expanding from the valve can only flow off into vacuum through the gas channel of the vaporization source with negligible escape. A three dimensional drawing with a cutaway showing a cross section of the source is depicted in Fig. 4.5(b). The main piece (S) of the vaporization source, the motor holder (H), the pulsed valve (V) and the mini-motor (M), all marked in the sketch, are represented in the actual orientation in the vaporization assembly. In the sketches (a) and (c) of Fig. 4.5, a side and a top view of the vaporization source mid sections are shown respectively. The characteristics of the first geometry (Typ 1) we adopted for implementing the main piece of the vaporization source can be drawn from them. Three transversal through-holes meet each other close to the center. The thinnest hole is the laser channel (diameter=1.5 mm). This channel passes not exactly through the center, but a few millimeters away. It is terminated with two stainless-steel inserts that can be installed into a thread. This allows

to choose the bore width or to mount windows. They can be easily replaced to fit the experimental conditions. Also the nozzle, mounted at the exit of the gas channel (2.5 mm of diameter) can be changed. This is an important adjustment parameter as the length of the chamber and the shape of the nozzle affect the ratio between monomers and clusters formation.

The gas channel, 24 mm long, is bored coaxial to the valve (V). It crosses the channel, mutually perpendicular to the other two, comprising the target rod which has a 8.5 mm diameter. The biggest hole (diameters of 17.5 mm recessed to 8.5 mm through) is drilled through the 1.5 mm channel directly after the point of bisection with the 2.5 mm channel. The portion of the bore with 17.5 mm diameter provides housing for the motor block which consists of the mini-motor, its holder, the rod and all parts that actuate the rod movements. The remaining part of the bore, having diameter of 8.5 mm, acts as a guide for the rod and defines with it two $1 \times 2.5 \text{ mm}^2$ channels for the carrier gas, which flows around the rod. The focused laser beam enters through the laser channel and impinges on the rod's surface almost tangentially. The generated plasma plume expands normal to the rod in a skew direction (skew angle $\sim 30^\circ$) with respect to the gas channel axis. Thus the plume propagates towards the output channel and not directly into the laser entrance bore.

The second geometry (Typ 2) we implemented for the main block of the ablation source is

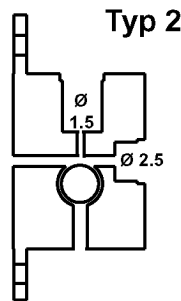


Figure 4.6: Top view of the vaporization source main piece with the second design (Typ 2) we adopted in our experiments. The gas pulse introduced by the valve flows into vacuum through the 2.5 mm diameter bore. A focused laser light enters the source piece from the 1.5 mm diameter opening on its side to ablate the rod surface.

shown in Fig. 4.6. The gas channel which is bored again in the middle of the source main piece, transversally to the other bores, does not intercept anymore the rod cavity right in the middle but rather tangentially. The vapour plume generated inside the gas channel is transported by a gas pulse 5 mm along the bore, reaching an interchangeable cylindrical or conical nozzle from where it expands into vacuum. The gas pulse is actuated by a valve with its orifice of 1 mm diameter coaxially connected to the 24 mm long bore of the

Smalley source. The metal plume enters the bore 12.5 mm downstream from the valve output nozzle.

The length of the gas channel from the point of vaporization to free expansion can be extended by the insertion of nozzles with the desired geometry. Besides the choice of its length (waiting room), this approach allows to affect the expansion characteristics by varying the opening angle of the nozzle. The nozzles which were implemented could be used in combination with both source geometries. In particular with the Smalley Typ 2 we tested nozzles having opening angles of 0° , 15° , 30° , 70° and lengths of 20 mm, 20 mm, 10 mm, 15 mm, respectively.

The assembled ablation source is placed on the front of the pulsed nozzle of the valve as

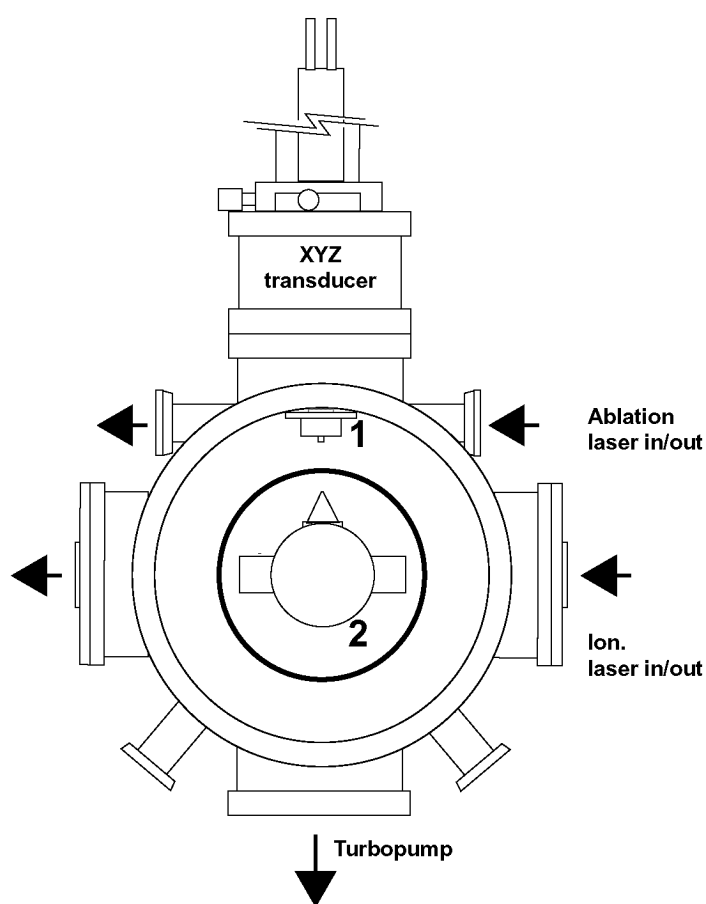


Figure 4.7: A side view of the source-chamber. Parts labeled as 1 and 2 are the vaporization source and the ionization stage of the mass spectrometer respectively. The latter is wrapped in a metallic shroud with a conical diaphragm (skimmer) screwed on top of it. The skimmer is coaxial with the gas channel of the vaporization source positioned a few centimeters above.

shown in Fig. 4.5. The valve is fastened to a metal assembly protruding into the vacuum chamber from its top flange. The assembly comprises several parts forming a vacuum tight “arm,, of adjustable-length. The vaporization source, positioned at one extremity of the

arm, is introduced into the vacuum chamber to fit the geometry defined by the ablation laser beam and the mass spectrometer. At the opposite side of the arm, a XYZ transducer enables the adjustment of the assembly position via three micrometer stages placed outside of the main vessel. Figure 4.7 illustrates the vacuum chamber with the XYZ transducer and the ablation source in place. The transducer provides a way to change the vaporization source placement within the chamber under vacuum. The length of the assembly is chosen according to the required distance between the output of the ablation source and the skimmer. When the the source chamber was open for servicing the apparatus, we temporary removed the rod to adjust the ablation laser. The focused laser light of the laser then entered the chamber from one side port to exit from an opposing opening, after having passed through the laser channel in the main block of the vaporization source.

A molecular beam (MB) was selected from the expanding gas with a 1 mm diameter, 30° conical skimmer. Typically, the skimmer and the ablation source nozzle were about 30 mm apart.

4.2.3 Laser systems

Three commercial pulsed laser systems were used in the experiments performed in this work. Their physical layout on the optical tables is shown in Fig. 4.2.

The 2nd harmonic output beam of a Spectra Physics Nd:YAG laser, Indi-20, operating at a fixed 20 Hz repetition rate, was used for the material ablation.

When used in Q-switched mode, the rep. rate is driven externally via a positive 20 Hz ($\pm 1\%$) TTL pulsed signal given as input to the corresponding flash lamp, and a 10 Hz Q-switch positive TTL pulse is fed to the Q-switch high voltage pulser. The delay between the rising edge of the lamp and Q-switch pulse must be of 210 ns to get the maximum output power.

While the Indi-20 is capable of producing over 150 mJ per 8-10 ns pulse at 532 nm, the pulse energy required to start the detachment of the material via ablation is typically ten times smaller. Excess energy may manifest itself in an increased kinetic energy of the ablated atoms. The formation of weakly bonded molecules is then hampered.

The Indi-20 laser has the best shot-to-shot stability when operated at 90% of the maximum

output power. In order to control the pulse energy, a beam attenuator was used. With the attenuator, the laser pulse energy impinging on the rod could be varied deliberately smoothly below 30% of the maximum output energy per pulse, in accordance with the attenuation we determined in Fig. 4.32. The laser beam exhibits a uniform round shape with diameter of roughly 8 – 9 mm diameter.

Our setup also comprises of a Spectra Physics Nd:YAG laser, model DCR-2A, to generate a 266 nm beam for mass spectrometer calibration or ablation. This laser has a fundamental wavelength of 1064 nm and is equipped with second (SHG @ 532 nm), third (THG @ 355 nm), and fourth harmonic generator (FHG @ 266 nm) crystals. The measured maximum output energy at the used wavelength is 15 mJ per pulse. This system was also triggered externally. Three 10 Hz TTL pulses were provided in sequence to control the amplifier and oscillator flash lamps, and the Q-switch. The delay between Q-switch and oscillator lamp was 210 ns, while the firing of the amplifier flash lamp occurred about 3 ms in advance. We determined the Q-switched laser pulses to have a 6 – 8 ns pulse width, using a 200 ps response time photodiode. The laser output is still a combination of the fundamental wavelength and its harmonics when emitted by the system. We therefore installed three dichroic mirrors for selecting the 266 nm component. A beam dump is needed behind some of the mirrors to absorb the other wavelengths that pass through.

For the DCR-2A, the beam profile is a doughnut with outer diameter of 7-8 mm. The laser housing for the crystals was purged during operation with N₂ and the automatic temperature control of crystal THG was disabled.

A Clark MXR Ti:sapphire laser system, was used to generate transform limited output pulses that have a duration of 100 fs and a repetition rate of 100 Hz. A description of this system is given in the following paragraph.

The pulse energies were varied between 10 and 250 μ J at a wavelength centered around 800 nm. The femtosecond pulses were focused into the source chamber to a diameter of less than 1 mm to give an approximated intensity in the order of 300 GW/cm². The pulses intersect the supersonic molecular beam containing the ablated material seeded in He, Ne or Ar with some oxidizer. The extremely short pulses allow a precise assignment of the time of birth (TOB) of the ions in the ionization stage of the mass spectrometer, and make the contribution to the broadening of the signal due to spread of initial ion flight times negligible. The femtosecond-laser system consists of a continuously pumped, Kerr-lens-mode-locked titanium-sapphire oscillator, which is pumped with the 3 Watt output beam of

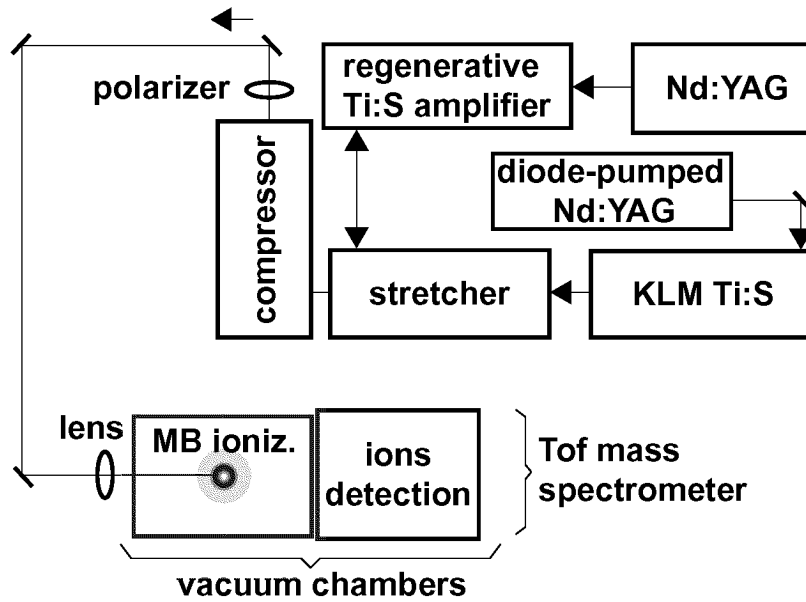


Figure 4.8: Experimental setup with : Ti:S, Ti:sapphire; KLM, Kerr-lens mode locked.

a diode pumped YAG laser (Spectra Physics, Millennia V).

The output of the oscillator is temporally stretched by passing a confocal 4-grating configuration twice. The stretched pulses are further amplified by a Nd:YAG-pumped (ORC 1000/ 8 Watt/ 1000 Hz) titanium-sapphire regenerative amplifier system. After amplification the pulses are re-compressed to ~ 100 fs duration. The 800 nm output of the compressor was used for ionization.

4.3 Time-of-Flight Mass Spectrometry

Time-of-flight mass spectrometry (ToF-MS) is a well established technique for determining ions masses and their relative concentrations. Introduced by Cameron and Eggers in 1948 [63], ToF-MS begins with gas-phase ion formation and then involves ion acceleration through an electric field into a field-free drift region. The acceleration voltage, giving all ions the same kinetic energy, propels the ions at different velocities based on their specific mass-to-charge (normally singly charged species are produced) ratios. Subsequently, the ions are allowed to drift in a field free region where they separate spatially as a function of their individual kinetic energies. Lighter ions will move faster than heavier ions. Following ion detection, “peaks” representing ion-packets each having the same mass comprise the mass spectrum, and the time needed to travel the length of the drift region (the “time-of-flight”) can be related to the mass of the ion.

4.3.1 Jordan Re-ToF-MS: Dimensions and arrangement

Instrumental Design

Measurements were performed on a Jordan angular reflectron Time-of-Flight Mass Spectrometer (model D-850) [64], assembled with a laser ionization chamber. The Re-ToF-MS, oriented orthogonally to the molecular beam from the vaporization source, is operated in positive-ion detection mode, with polarities chosen accordingly for ion extraction (positive extraction voltage), acceleration and detection (negative bias). The mass spectrometer design allows for either linear mode or reflectron mode operation.

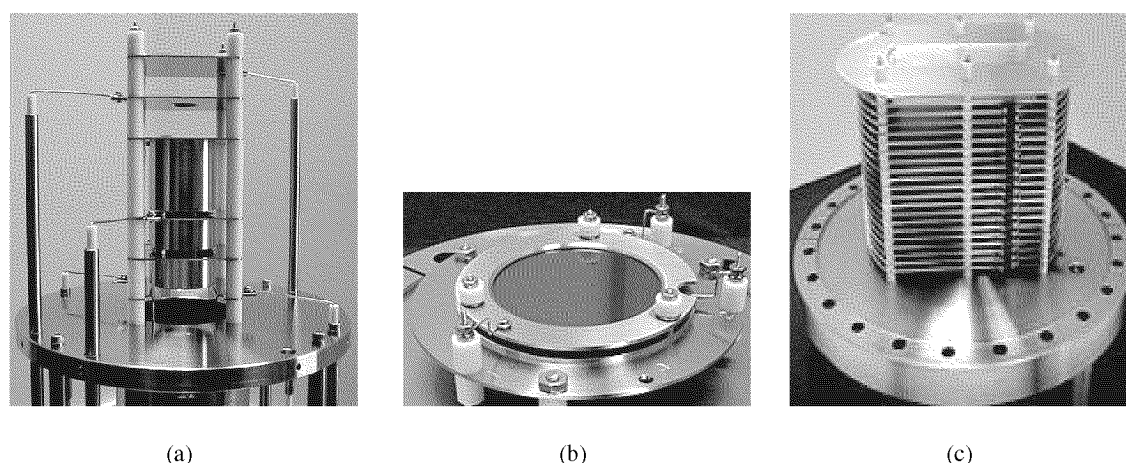


Figure 4.9: Picture 4.9(a) illustrates the ion source assembly of the Jordan Re-ToF-MS without the shroud holding the skimmer, that usually hides it. The assembly that protrudes in the ionization chamber (see Fig. 4.11), consists of repeller plate, extraction grid, acceleration grid, Einzel lenses and steering plates. The 40 mm dual microchannel plate detector is visualized in picture 4.9(b). It is mounted on a offset adaptor that fits the geometrical constraints. It provides high gain (10^6 to 10^7) with sub-nanosecond rise time on a 50 ohm output. The reflectron assembly is shown in picture 4.9(c) with an entry grid that we used at ground. Behind this, a set of several plates give a uniform repelling field. Together they form the so called repeller grid.

In the first case, detection occurs through the inactive reflectron with a MCP-detector placed behind it. The second operation mode, with the reflectron on, is characterized by ions flying back in the flight tube toward their starting position, where they are detected with a MCP mounted slightly off-axis in order not to obstruct the pass of incoming ions. Overall, the instrument can be considered a system of several regions, the ionization stage, the focusing ion lens and mass gate, the free field flight tube, the reflectron and ion detectors. The Jordan Re-ToF-MS is schematically represented in Fig. A.3 with the electrode voltages and relative distances indicated. The actual values for electrode distances are noted in Table 4.3.1.

	d_1	d_2	δ	Δ_x	Δ_y	D_1	d_g	Δ_r	D_2
[inches]	0.5	0.5	2	1	1	39.88	0.47	3.81	25.43
[cm]	1.27	1.27	5.08	2.54	2.54	101.3	1.18	9.67	64.6

Table 4.1: Mass spectrometer distances in inches and cm. The names refer to the nomenclature introduced in Fig A.3.

A ion flight length of 1.8 m is expected [65] for this type of mass spectrometer (as could be inferred from the values of Table 4.3.1, referring to Fig. A.3).

The design employed by R.M. Jordan Co. is based on the original suggestions of Wiley and McLaren [66]. In this design, the ion flight time is relatively insensitive to the exact point of ion formation in the extraction region. This technique, called “space focusing” allows high mass resolution and relative simplicity of construction [67]. The readers, interested in the mathematics behind the space-focusing criterion, are referred to the review by Guilhaus [68].

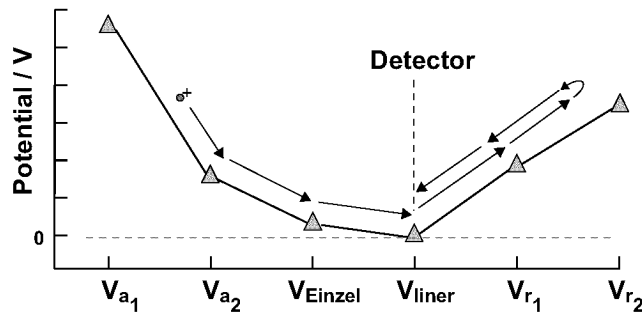


Figure 4.10: Schematic plot showing the typical potentials used for the Jordan ToF-MS. The ions are accelerated in the extraction/acceleration region towards the drift region. Ions with a constant speed enter the reflectron where they are decelerated and, after ion velocity reversal, accelerated back towards the detector.

The optimum operating voltages for the experiments were computed with the approach described in appendix A. In our experience, these voltages could be used in a number of ion detection experiments with only small tweaks. The voltages themselves were provided by six DC high voltage power supplies, model NHQ-233M (Iseg Spezialelektronik GmbH). Each unit has two independent high-voltage outputs that can be inverted in polarity and are protected against overload and short circuit. Its maximum output voltage is 3 kV with a 4 mA peak current limit. In the experimental setup, values of output current were limited to range between -10% and $+10\%$ of the nominal maximum current.

Vacuum System

A vacuum of less than $\sim 10^{-7}$ mbar, and that of 10^{-5} mbar while operating the molecular beam source, is achieved by a two-pump system.

A Pfeiffer turbo-molecular pump (TPH 520, 520 l/s N_2 pumping speed), connected to the main source chamber through its bottom port (DN 160 ISO-KF), is used in conjunction with an Alcatel 2100 fore pump. The rotor of the pump is separated from the volume of the source chamber by a gasket comprising a metallic grid. The grid A second turbo pump (Pfeiffer, TPH 240) is attached to the port (DN 63-CF) devised in the drift tube of the mass spectrometer (Jordan, Sideport Tee C-687). The turbo pump is connected to a mechanical rotary vane pump (Alcatel 2012 A). Flexible metal tubes KF40 and KF16 are used to connect the turbo pumps and their mechanical roughing pumps. Both fore pumps were provided with an oil mist eliminator stage to trap exhausted oil from the pump and return it back. Each turbo pump is driven by a 2-phase controller (TCP 380) that can adjust the turning speed of the pump rotor according to the torque it experiences. Vacuum pressure is monitored in both source and detection chambers by a combination of Pirani and Penning gauges (or cold ionization gauges) which provide a full range coverage which cover the entire range from 10^3 mbar down to 10^{-8} mbar. The controller switches automatically between the two device readings when the pressure drops from the active range of one gauge to the other. The Pirani gauges were attached to the hoses which connect the turbo pumps with the mechanical vane pumps, sensing thus the fore vacuum conditions. A cold ionization gauge measured the pressure in the mass spectrometer flight tube through a CF63 port. Another Penning gauge was mounted in a side port of the main source chamber to monitor its pressure. The controller was also used to read the signal of an additional Pirani gauge in the source chamber, determining the actual pressure at low vacuum conditions.

During measurements, the flight tube pressure was maintained between 5×10^{-7} mbar and 5×10^{-6} mbar, while the fore pump pressure typically ranged between 3.5×10^{-3} mbar and 2.0×10^{-3} mbar. The base pressure with no gas load was typically 10^{-7} and 10^{-8} mbar for the source and detection chambers, respectively.

For a typical gas load at 5 bar (back pressure) introduced from the pulsed nozzle at 10 Hz, the operating pressures in the source and detection sides were $\sim 10^{-5}$ mbar and lower than 10^{-7} mbar respectively.

Tof Ionization region

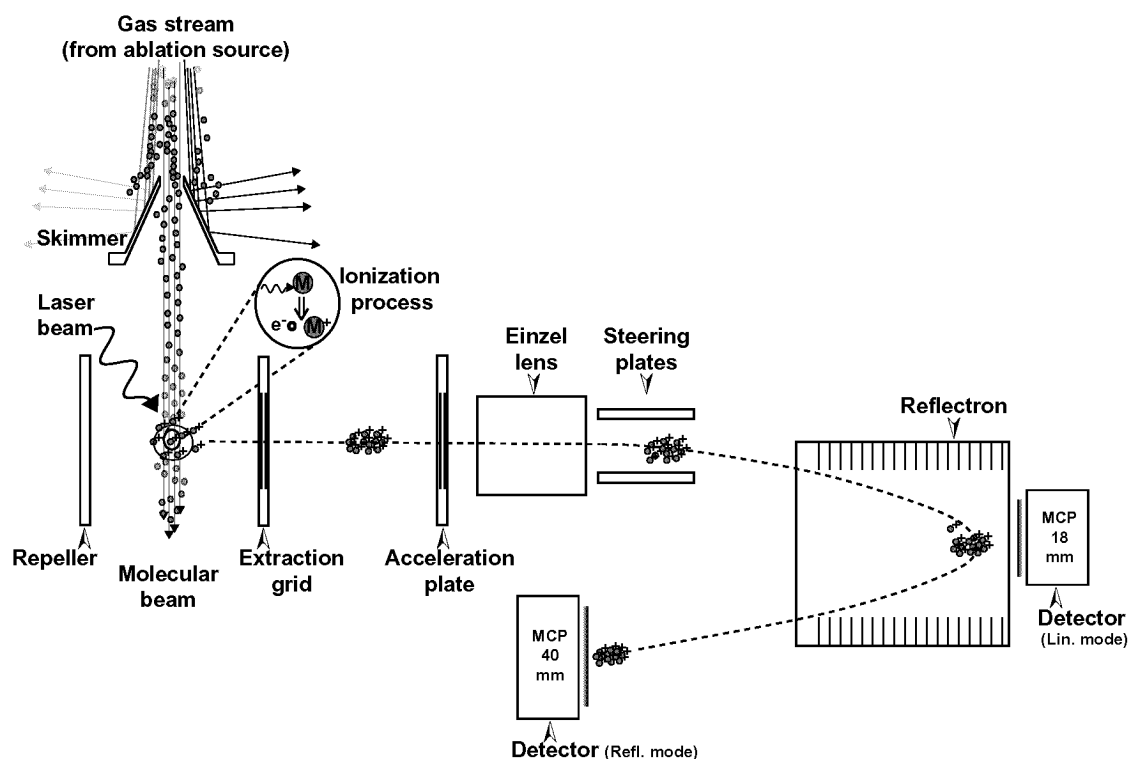


Figure 4.11: The molecular beam produced by the ablation source is skimmed to select the central part within a small solid angle. Finally the remaining beam reaches the ionization stage of the mass spectrometer where it crosses, transversely, a focused laser beam. The laser ionizes the molecules dispersed in the molecular beam. Emerging ions are accelerated by the DC voltage difference applied across a couple of plates, called repeller and extraction grid. A second stage (acceleration stage), where another field is applied, propels the ions further away towards the drift region, where no field is present. Ions with higher masses take more time to reach the detector.

The ionization or interaction region of the Jordan mass spectrometer is defined by two plates, a “repeller” and an extraction grid. After extraction, an ion is accelerated by a field established between extraction grid and another electrode, the accelerator plate. A sketch which illustrates all stages of ion mass detection, from ion formation and extraction to its detection, is shown in Fig. 4.11.

A thick gold-plated copper shroud encloses the ionization space (see Fig. 4.12), which allows an efficient differential pumping.

The molecular beam enters through a skimmer between the ion extraction plates where the ionization laser beam strikes the molecules orthogonally from the side. After ion formation, the static positive extraction voltage difference propels ions out of the ionization region and transmits them through the extraction grid (Ni mesh) into the acceleration region. The acceleration plate is set to a constant bias which accelerates ions into the field-free drift tube.

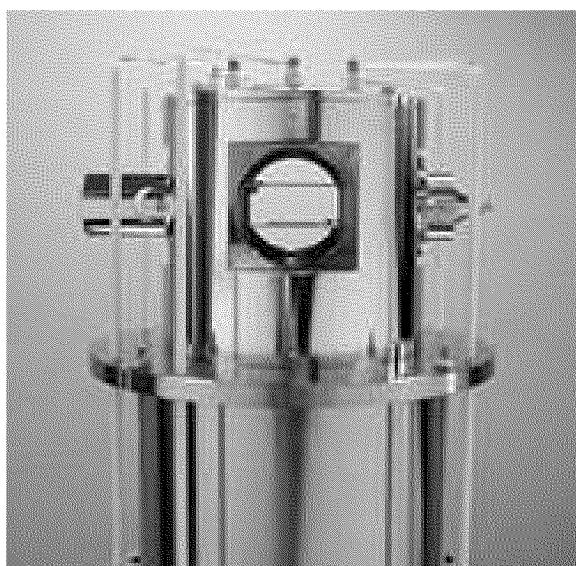


Figure 4.12: Detail of the ionization stage of the mass spectrometer from Jordan. A Ni skimmer is installed on a shroud enclosing the dual-stage ionization and acceleration section of the Re-ToF-MS.

Ion deflection and mass cutoff

A couple of steering plates, called mass gate, are located at the entrance of the field free flight tube. They are used to reject a range of ion masses from the mass spectrum by deflecting their trajectories. They can also be used to compensate for transversal speed components that could cause the ions to drift away from the axis of the flight tube. The

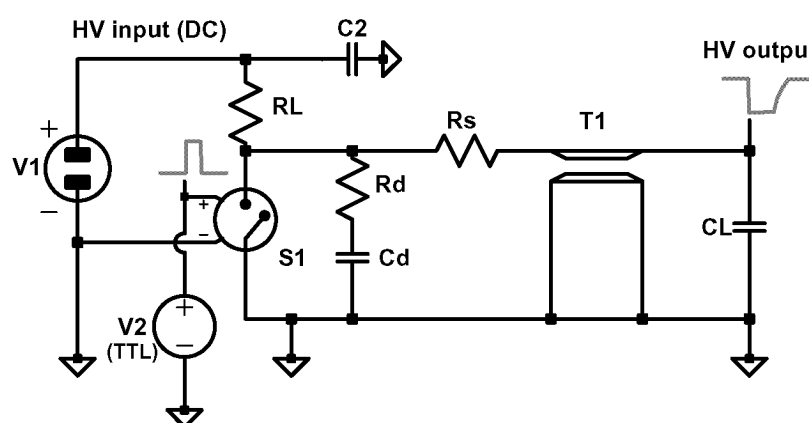


Figure 4.13: Schematic of the HV pulse circuitry driven by a TTL signal.

presence of ions with low masses potentially represents an obstacle in detecting higher masses with less abundance. In particular, if the electrical pulse generated exceeds the maximum current sustainable from the MCP (nominally $400 \mu\text{A}$), the signal saturates the device and makes it relatively insensitive to subsequent masses arriving within a short time interval. Typically a mass selection among the detectable ions is achieved by applying a

pulsed voltage across the mass gate plates.

The mass gate is switched on for the time during which unwanted masses pass along it, and they are then kicked off the trajectories reaching the detector. Alternatively, the detector itself, the MCP, can be switched on and off. However this option is much more difficult to realize electronically [69]. We thus used the mass gate to preselect the masses to be measured. A driver, providing an active low 500 V pulse with a fall time of ~ 20 ns, was used to set the mass gate off. We built a pulse generator from a Behlke fast high voltage

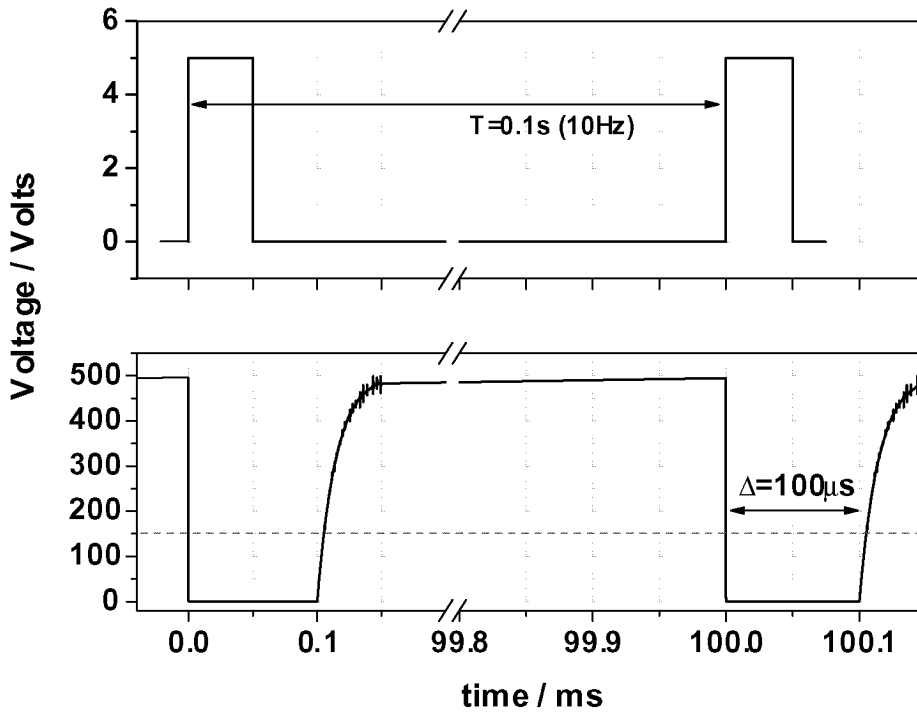


Figure 4.14: Voltage vs time for the driving TTL pulse (upper trace) and the corresponding HV voltage applied to the steering plates of the Jordan Re-ToF-MS. The

transistor switch (model HTS-30, $100\ \mu\text{s}$ on time extension) providing a switching voltage adjustable between 0 V and ± 3000 V and a peak current of 30 A. The Behlke switch was installed in a metallic box and connected to a DC voltage supply as shown in Fig. 4.13. The electronic components used in the circuit were impedance matched to the mass gate load to suppress ringing.

The performance of the pulse generator is illustrated in Fig. 4.14. When a trigger pulse (upper trace) is given as input to the switch, it commutes very quickly from the power rail (500 V) to reference. The voltage difference then rises back to its original value after roughly $100\ \mu\text{s}$ with a slope not as steep as during the previous switching phase. The high voltage signal, acquired on the oscilloscope with a $1\ \text{M}\Omega$ probe, is shown along with the

expected behavior in Figure 4.15. The rates of the falling and rising edges for the high voltage pulse are also reported there.

The pulse generator allows us to reject ion masses below a certain mass threshold. With the electronics tuned for best performances, we achieve an effective cut off for masses below 60 Da with an uncertainty of about 5 Da. The accuracy is limited by the mass separation that is established after a travel of about 250 mm from the ionization region to the mass gate.

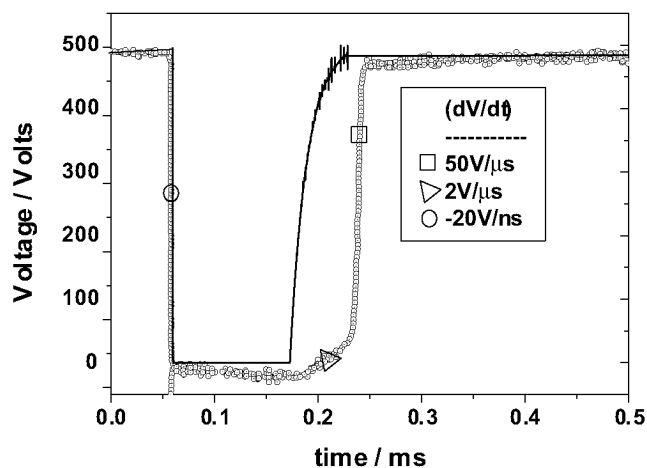


Figure 4.15: Computed (line) and measured output signal (circles) of the Behlke fast switch versus time. Switching speeds are indicated for three instances (symbols).

Liner

Inside the detection chamber, rolled stainless steel cylinder of 18 cm diameter surrounds the drift region and electrically isolates the ions from the ground potential of the flight tube. It is mounted on insulating spacers and can be removed. A gridded opening allows improved conductance to the pumping side-port in the detection chamber. The cylindrically symmetric shield, also called “liner”, can be biased to a potential (V_g , according to Fig. A.3) of a few hundred volts, but is usually held at ground (ie $V_g = 0$ V).

Reflectron

The Jordan ToF spectrometer comprises a dual stage reflectron which is shown schematically in Fig. 4.11. This is composed of an entry grid which is normally at ground or flight tube potential. Behind is a grid, followed by a set of several plates equally spaced. Contiguous plates are not isolated but there exists a high impedance of $1\text{ M}\Omega$ between each pair

of them exists. Only the voltages of the entrance and exit plates of the reflectron must be set to give a uniform repelling field. In Fig. A.3 the reflectron voltages are indicated as V_{r1} and V_{r2}). When they are set equal to the liner potential ($V_{r1}=V_{r2}=V_g$), the ions can pass through the reflectron plates and be detected, in linear mode, by a MCP.

The reflectron was introduced by Mamyrin [70] in 1973. After traversing the flight tube, ions enter a retarding field defined by a series of grids (reflectron), and are turned around and sent back through the flight tube. The principle of the reflectron (or ion mirror) is that an ion with higher energy will penetrate the retarding field more deeply, will spend more time turning around, and will just catch up with a slower ion (of the same mass) at the time they both reach the detector.

The reflectron results in some loss of secondary ion signal. In part this is due to the introduction of additional grids. However, the loss in secondary ion signal (particularly that due to molecular ions) is also due to the fate of metastable ions, which decompose in the field-free region prior to entering the reflectron.

Ion detectors

Two dual micro-channel plate detectors (Burle Electro-Optics, Inc., Part#30220-30392) with active diameters of 18 and 40 mm respectively, are used in combination with the Jordan Re-ToF-MS. Both MCPs are characterized by a gain of 10^6 and sub-nanosecond rise time [71]. A grid, 1 cm in front of each MCP stack, is held at liner potential to allow a field-free drift region for ions in the flight tube. Details, on how two MCP plates can be placed in series to increase MCP stack gain and to suppress ion feedback effects, could be found in the article by O. Almen et al. [72].

When in linear operation mode, the ions catch up at the 18 mm detector following the flight tube, and the 40 mm detector is reached after reflection, back in the flight tube, when in reflectron mode (See Fig. 4.11). The electronic configuration does not preclude simultaneous use of both detectors. Each of the MCP detectors is operated for positive-ion detection. A Divider box provides the three voltages necessary for a dual MCP detector. Two identical boxes were used to divide the high-voltage input and supply the required electric field to the MCP stack. Following impact by the positive ion, the first plate produces an electron output which is subsequently amplified to more electrons to provide a gain on the ion signal. The detector gain is governed by the potential applied to the plates (0 kV to -3 kV). For detector potentials of -1000 V to -2000 V, the nonlinear gain profile is between 10^4

and 10^5 [71]. Considerable signal ringing and poor signal quality are characteristics of operating voltages close to -3000 V on the detector. Therefore, with most experiments we employed potentials between -1600 V and -2500 V. The gain selected is determined by the intensity of the ion signal observed on the oscilloscope, and signal saturation is avoided by lowering the detector voltage. The detection efficiency of the MCP varies considerably based on the velocity of the impinging ions. For positive ions with acceleration potentials of 1500 to 2500 eV, the efficiency is approximately 20% to 60% [71]. The output of the detectors is an electron current that is transmitted to the oscilloscope and terminated in a 50Ω resistance.

Interlocks

An electronic interlock system utilizing voltage relays was designed to prevent, or at least minimize the danger of jeopardizing the apparatus and its auxiliary equipment in case of a catastrophic failure.

In order to set an upper limit for the pressure achievable in the apparatus, a relief valve was installed. It lets the gas flow out of the system if the pressure exceeds 1.5 bar.

An electro-actuated valve is used to flush the system with Nitrogen when the turbomolecular pumps come abruptly to a rest (e.g.: power failure, leaks, pump mechanical failure, etc.). This may cause the higher vacuum to come in direct contact with a lower one in the pump, which might cause the oil in the backing pump to be sucked into the vacuum chamber.

Ionization

In time of flight mass spectrometry, ion masses are marked as different according to the time the ions need to reach a detector placed at a fixed distance. Neutral species cannot be detected unless they are previously ionized. Generally any desorption process that produces ions is likely to produce neutral species in numbers that are orders of magnitude higher. Unfortunately the ionization efficiency is rather small. In our experiment in particular, we concentrate our attention on the neutrals that might originate from the combination of ions and neutrals in the plasma plume with oxidizing molecules seeded in the noble gas. Ionization can be brought about by electrical discharge, laser light, electrons or another charged particles, but it usually leads to fragmentation of the molecules. In this work we

restrict our attention to laser light ionization. Under this broad category, we shall distinguish between single photon ionization (photo-ionization processes) and double or multi-photon ionization.

Advantages of femtosecond lasers

Femtosecond laser ionization is a sensitive and selective analytical technique in mass spectrometry. The high intensities ($> 10^{12}$ W/cm²) of the ultra short light pulses greatly enhance the probability of multi-photon absorption, leading to a much higher ionization yield. Further, in nanosecond ionization, intermediate dissociative states may cause fragmentation of laser irradiated species upon multi photon absorption. In contrast, using a fs excitation, the ionization process is completed within the pulse duration and there is not enough time for significant fragmentation of molecules. An additional advantage is that multi-photon ionization processes are easily saturated, leaving the molecules in the interaction region ionized. This provides an uniform sensitivity of the detection and a robustness to moderate laser intensity fluctuations. Having different molecular species in the ionization region, the fs multi photon process enables their simultaneous detection.

However, the intense femtosecond pulses are not always of advantage. In fact, one has to be careful to avoid strong field effects. Strong electric fields may deform the molecular potentials and a n-fold multi photon ionization process does not correlate to a power of n intensity dependence. Consequently, a straightforward interpretation of the results would be difficult in this situation. The laser intensity in the experiments was limited to 1500 MW/cm², thus keeping strong field effects as small as possible.

4.4 Time delay schemes for triggering

The Spectra-Physics DCR-2A Nd:YAG laser is the rate limiting device in our apparatus. The frequency of data acquisition cannot exceed 10 Hz. During experiments several events must be synchronized:

- Opening of pulse valve;
- Laser firing for photo-ablation;
- Laser firing for ionization;
- Start of detectors' signal recording (data acquisition);

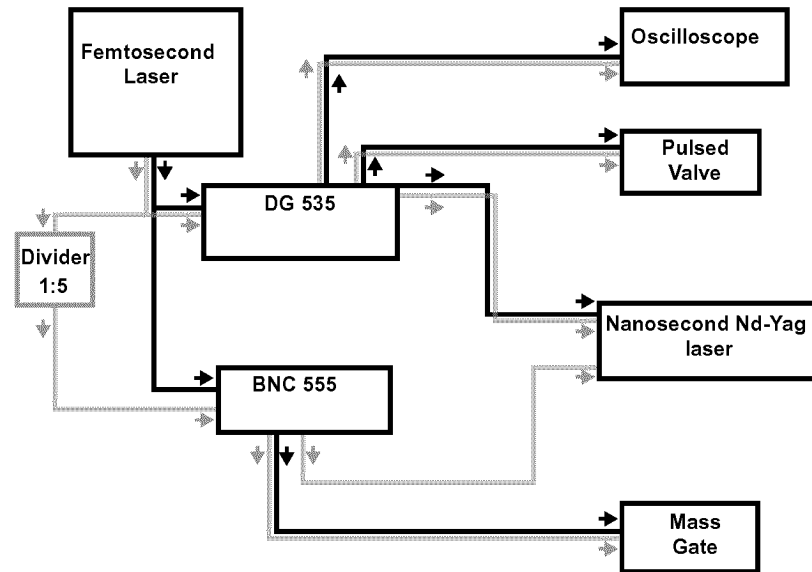


Figure 4.16: Schematic block diagram of the connections for events synchronization in the experimental setup. The connections between devices and delay units we used in combination with the DCR- and Indi- triggering schemes and described in this section, are indicated with black and grey lines respectively. Directions of arrows show whether trigger signals are given in input or are generated by a device.

- Extraction pulse for ion masses to be rejected (mass gate).

The master timing diagrams in Fig. 4.17 and Fig. 4.18 summarize the events occurring for the two different triggering schemes we exploited. The two schemes allowed us to use two distinct laser systems for material ablation in combination with the experimental setup. One triggering scheme (Indi-scheme) sets the appropriate timing of the Indi-20 laser firing with respect to the other events (see section 4.2.3 for reading about the characteristics of Indi-20 laser system). The other scheme (DCR-scheme) does the same for the DCR-2A laser, described in section 4.2.3.

The timing of the events listed above are controlled by two programmable delay generators (Stanford Research Systems model DG 535 and Berkeley Nucleonics model BNC 555). These devices play a key role for the experiments.

In Fig. 4.16 a schematic block diagram shows the connections between the delay generators and the other parts of the experimental setup. Connections indicated by black and grey lines in Fig. 4.16 are typical for the DCR- and Indi- triggering schemes, respectively. Arrow directions show whether a signal is used to trigger (inward arrow) a device or originates from it (outward arrow) to drive other equipments. A 100 Hz TTL pulsed signal (*master signal* in Fig. 4.17) is generated by the femtosecond laser system 0.587 μ s in advance with respect to the laser firing. The *master signal* triggers the DG 535 unit. Output signals,

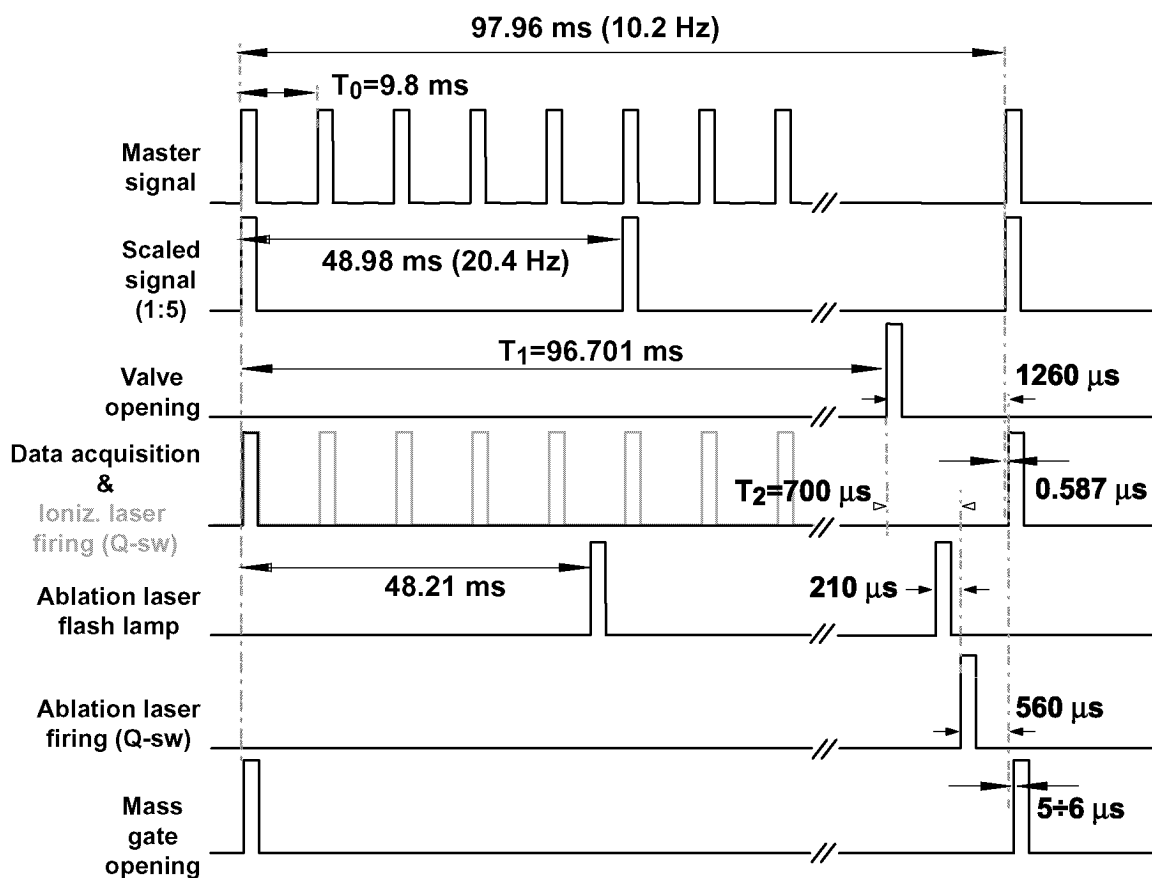


Figure 4.17: Master system timing diagram when the Indi-scheme is used. Ten complete acquisitions occur per second. T_0 is the period of the master clock for the DG 535 delay generator. The timing of all signals maximizes the yield of Zn with Ar, at 4 bar, as noble gas and a distance ablation source nozzle-skimmer of 4 cm.

opportunistically delayed from the trigger, are generated by the Stanford device to:

- open the valve (the closing time is regulated by the controller described in section 4.2.1);
- trigger the oscilloscope to start a data acquisition (which lasts for the oscilloscope capture time typically of a hundred μs);
- make the ablation laser fire and intersect the gas stream let in by the valve.

In the Indi-scheme, the *master signal* is also directed to an electronic divider which transmits a pulse each five to generate a 20 Hz signal (*scaled signal* in Fig. 4.17) with at most 2 ns jitter. The *scaled signal* is given as an input to the BNC 555 delay generator. The BNC 555 uses the 20 Hz TTL pulses as triggers to generate two signals, indicated in Fig. 4.17 as *ablation flash-lamp* signal and *mass gate signal*, respectively. The 10 Hz *mass gate* signal, whose delay is manually adjusted, controls the switching of a high voltage pulser (see section 4.3.1) that kicks unwanted ions off their ideal trajectory by applying a high voltage

difference across the Re-ToF-MS steering plates. The *ablation flash-lamp* signal represents

Zn maximized, ablation source-skimmer= 3.5 cm (no nozzle)			
Ablation-laser: Spectra Physics Indi-20			
DG 535	Ar+1%O ₂ 2 bar	Ar+1%O ₂ 4 bar	He+1%N ₂ O 4 bar
Ch A	0.097201 s	0.09701 s	0.097268 s
Ch B	0.000000587 s	0.000000587 s	0.000000587 s
Ch C	0.000550422 s	0.000645422 s	0.000614022 s

Table 4.2: Delay settings on the DG 535, used in the Indi-scheme. For assigned noble gases, pressures, and geometry these settings grants the best yield of zinc.

the trigger for the flash lamp of the ablation laser. Its timing is set accordingly with the occurrence of the Q-switch in order to keep the interval between their pulses constant at 210 μ s. This condition, required to obtain the best stability for the ablation laser throughput, is achieved by adjusting the two delay generators generating the required pulses.¹

ZnOH, N ₂ maximized, ablation source-skimmer =4 cm (no nozzle)			
Ablation-laser: Spectra Physics DCR-2A			
DG 535	Ar+1%O ₂ @ 4 bar	Ne+1%O ₂ @ 4 bar	He+N ₂ O @ 4 bar
Ch A	0.096860 s	0.096930 s	0.09702 s
Ch B	0.000000587 s	0.000000587 s	0.000000587 s
Ch C	0.000474554 s	0.000595022 s	0.000574022 s

Table 4.3: Some example of delays that maximize the intensity of ZnOH and N₂ for the geometry, gas type and pressures indicated.

In combination with the Spectra Physics DCR-2A Nd:YAG the triggering scheme (DCR-scheme) is simplified. This laser can be triggered with a TTL pulse given in input to its oscillator that controls the arming of high voltage at the flash lamp ends. Each pulse of

¹The DG 535 by construction cannot generate 20 Hz TTL pulses when it is already used to provide signals with smaller frequencies. A limitation that the BNC 555 delay generator does not have, since each of the device's 4 output channels can supply, independently, TTL signals with frequencies that are fractions of the frequency corresponding to the triggering signal. However we decided to use both the delay devices because of the following considerations: (1) the jitter of signals generated by the BNC 555 is of the order of few nanoseconds, which is not negligible with respect to the detection time uncertainty of ion masses with tens of Da (the jitter value for the DG 535 is two order of magnitude smaller); (2) in each delay device the number of available channels is smaller than needed.

the triggering signal has to occur about 3 ms in advance with respect to a flash lamp burst and subsequent Q-switching (the last two events occurring 210 μ s, as in the Indi-scheme). We operated the DCR-2A laser with the triggering approach described and measured with a photodiode, a jitter of laser shots with respect to the oscillator signal given externally, shorter than 1 ns. In our experiments the uncertainty on the measurements is a few tens of nanoseconds, and the jitter due to the triggering approach contributes to this error in negligible way.

It is useful to compare the DCR-scheme with the Indi-scheme and underline the following differences: the pulsed valve, the ionization and ablation lasers are completely controlled by one delay device, DG 535, while the BNC 555, triggered directly by the *master signal* from the femtosecond system, divides the signal by ten. The resulting 10 Hz signal is delayed manually of a few microseconds (the delay depends on the voltages across the ionization and acceleration stages of the mass spectrometer) to control the high voltage extraction pulse. Figure 4.18 shows the timing diagram with values corresponding to the delay settings that we found successful with Ne at 4 bar and a distance ablation source nozzle-skimmer of 3.5 cm. This set of values maximizes the yield of ZnOH. The input power of the ablation laser is attenuated to 4 mJ.

The output signal from the MCP assembly (see section 4.3.1) at the end of the ToF-MS is monitored by a 1 GHz digital oscilloscope (LeCroy model WavePro 950). The data are visualized on the oscilloscope display to guide fine tuning of the signals delays, and logged for off-line data analysis. A computer program, written by Dr. Radi and modified to be compatible with this experimental setup, sends commands to the GPIB bus on the oscilloscope and the delay device DG 535 through a GPIB controller card (National Instruments \sharp GPIB-ISA). Instructions and data were also exchanged with the BNC 555 delay generator, via its serial port. The existing software to drive the device remotely, was also modified to fix some code errors (causing switch off/on and channel parameter resets to be inconsistently controlled) and to adjust the unit settings within a unique environment. The program allows to vary the occurrences of the events listed above, each independently from the others or keeping fixed the time interval between a pair of them (for example, we can modify the time at which the ablation laser fires with respect to the occurrence of ionization laser shot, while the time interval between the valve opening and ablation laser q-switch does not change). The delay is varied until a given mass peak reaches a maximum as seen on the oscilloscope.

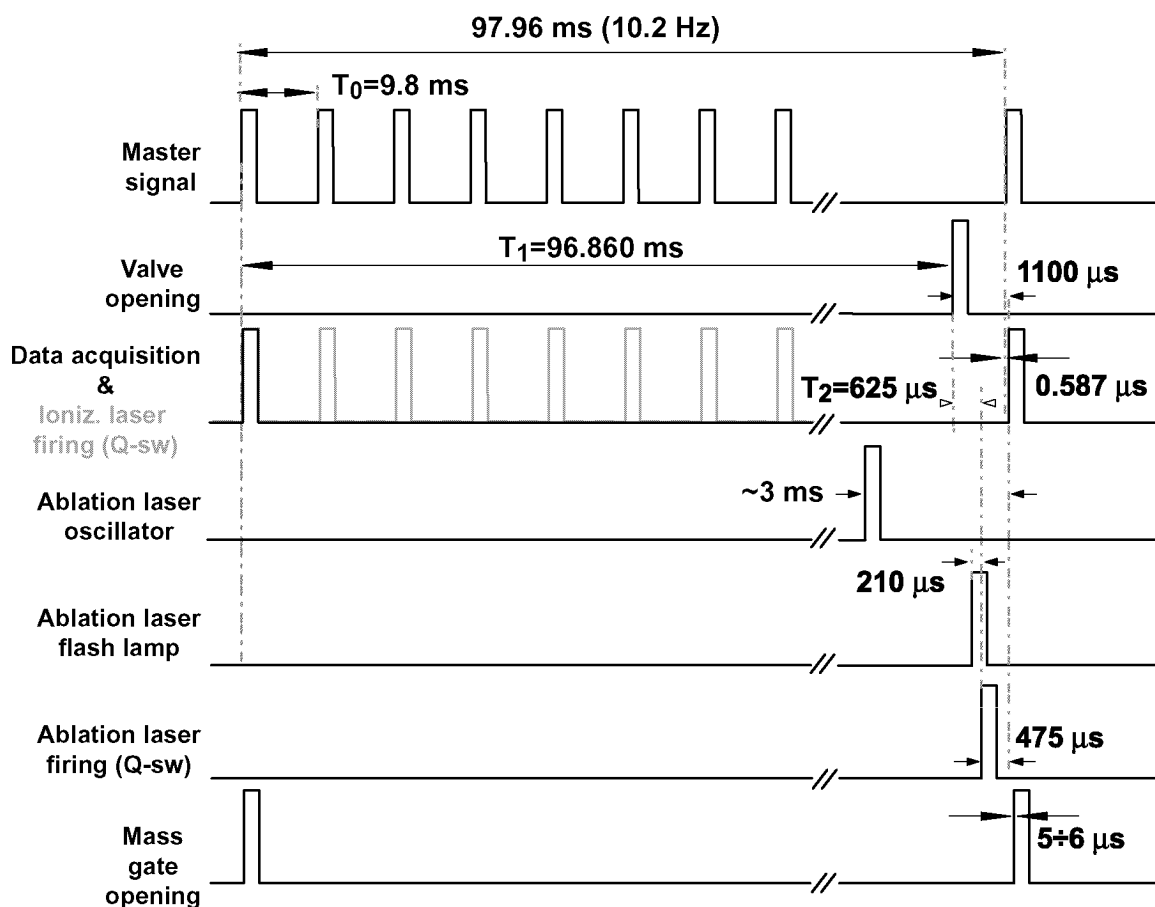


Figure 4.18: Master system timing diagram when the DCR-scheme is used. The delays indicated are for Ne, at 4 bar, as noble gas and a distance ablation source nozzle-skimmer of 3.5 cm. The yield of ZnOH is maximized in correspondence to this set of values.

A semi-automatic scan mode is available: it allows to independently control the timing of events with the option to keep some of the delays fixed. The program then requires to set the desired time scale on the oscilloscope for the channels to be detected, and the interval of interest. The averaging of N subsequent acquisition has to be specified as well, choosing an appropriate value for N . Figure 4.19 shows several plots of the intensity versus time obtained for the He+1%N₂O gas mixture at 4 bar. The time settings given in table 4.2, that maximizes the yield of zinc, are used to initialize our setup. The first plot on the bottom of Fig. 4.19 is obtained by keeping the valve opening time fixed with respect to the ionization laser occurrence and by varying the time at which the ablation laser fires. The other plots, from bottom to top, are collected for decreasing ionization laser energies per pulse, 150 μ J, 130 μ J, 90 μ J, and 65 μ J respectively. The traced intensities are for Zn, N₂O, N₂, and C. The C and N₂ intensities were measured only at lower pulse energies of the ionization laser, i.e. for 130, 90, 65 mJ and for 90, 65 mJ respectively. The events of ablation laser firing and valve opening are shifted together with respect to the occurrence of ionization laser firing,

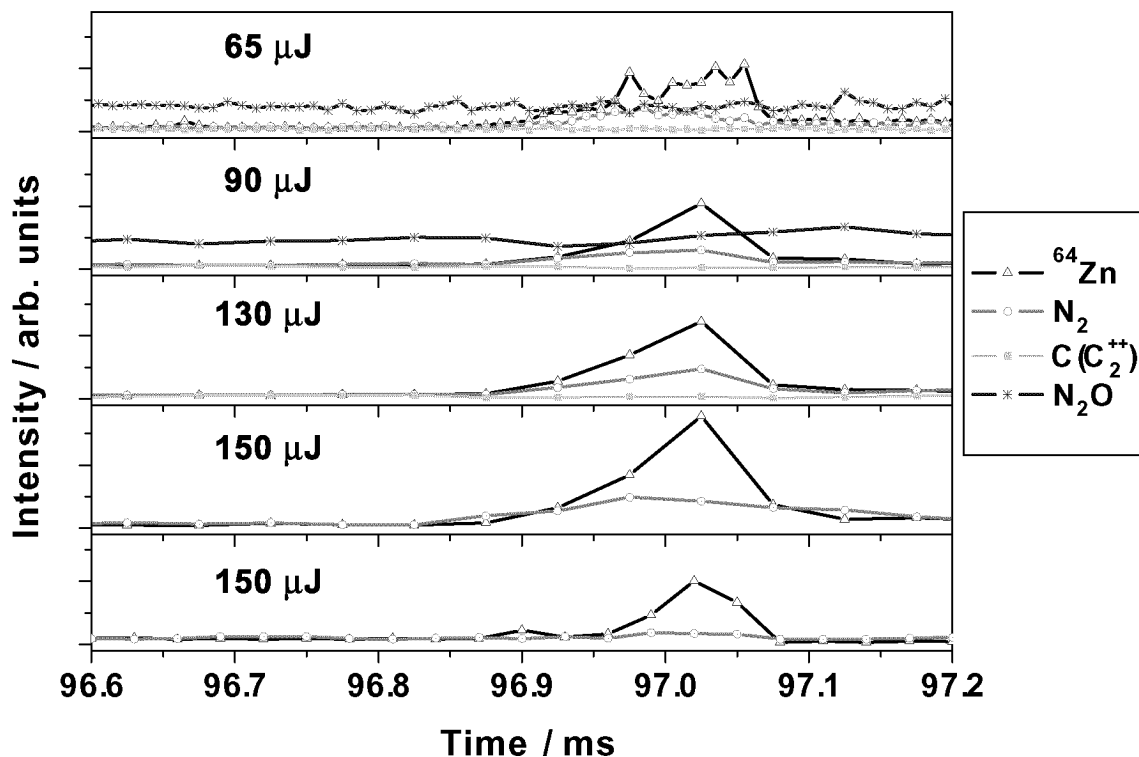


Figure 4.19: Intensity of ^{64}Zn , N_2O , N_2 and C versus ablation laser firing time for different ionization laser energies per pulse. With the overall timing conditions in table 4.2, from bottom to top the energies are 150 μJ , 150 μJ , 130 μJ , 90 μJ and 65 μJ .

keeping constant the time delay between them. In the second plot from top, the peak of N_2 corresponds to a slight minimum of the intensity of N_2O as we might expect if we assumed that a fraction of the N_2 detected results from N_2O dissociation.

We can use the same system to evaluate the advantage of increasing the opening time of the pulsed valve and measure the valve response. For the configuration just described, we scan over the occurrence of ablation laser firing (with zero corresponding to the time settings in table 4.3). Data acquired for increasing values of the valve opening time are summarized in Fig. 4.20. The intensity reach a maximum and drops again probably due to the degraded vacuum conditions. In our conventional approach we measure the pulse energy of the femtosecond laser output beam only before an experiment is started. Then a reference or background spectrum is determined prior to acquire a full spectrum. Only during subsequent data analysis a subtraction of the two spectra can be operated.

Since experiments are repeated at 10 Hz while the femtosecond laser fires at 100 Hz, one laser shot from ten is used for data acquisition of the Re-ToF-MS. When passing through the vacuum chamber, only this laser shot intercepts the molecular beam expanding from the va-

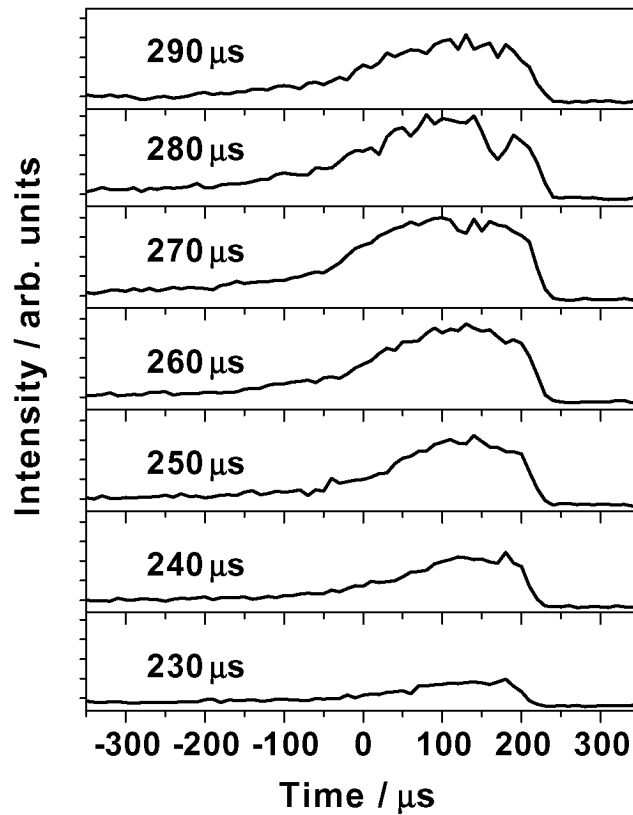


Figure 4.20: Intensity of the ^{64}Zn isotope versus delay between ablation laser and valve opening. Parameter for the curves is the aperture times of the pulsed valve. Conditions are the same as in Fig. 4.19.

porization source. Each of remaining fs-laser shots transiting the vacuum chamber ionizes the residual chemical species. The corresponding signal measured with the Re-ToF-MS can be used as a reference spectrum (spectrum-0) determined within a short time interval (as low as T_0) from the molecular beam spectrum (spectrum-MB). The sequence mode of the Lecroy oscilloscope is suitable to measure these two spectra in parallel and observe their subtraction on the screen. In Fig.4.21, a spectrum, obtained by subtracting spectrum-0 from spectrum-B using the oscilloscope sequence mode, is plotted. The subtracted spectrum is averaged over 300 acquisition.

The main advantage of this measuring approach is to avoid changes due to a variation of the ionization yield. Unwanted species polluting the system are present with equal intensities in both the parallel spectra acquired and their signal is perfectly suppressed in the subtracted spectrum.

However, two serious drawbacks must be taken into account:

- more oscilloscope memory is used, limiting the achievable sampling rates;
- the oscilloscope operating in sequence mode stores the data of each spectrum in a

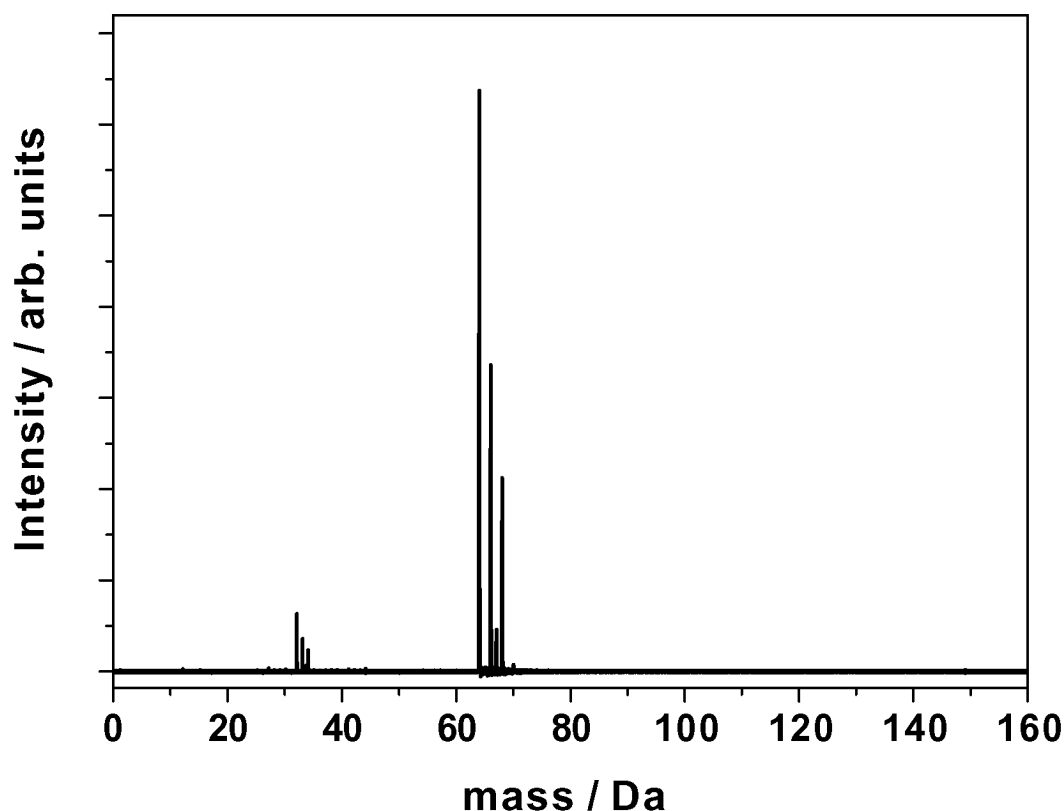


Figure 4.21: A mass spectrum obtained using the capabilities of the digital oscilloscope and the high repetition rate of the fs-laser firing with respect to the frequency of data acquisition. The signal of chemical species always contained in the vacuum chamber, being equal in both the molecular beam spectrum and its reference acquired in sequence, can be removed by subtraction. Due to some drawbacks, described in the text, it has not been adopted for the measurements.

separate memory region. There, data points exceeding the voltage scale are not retained and assume random values. This may appear with visible (but hard to interpret) artifacts in subtracted spectra.

This acquisition scheme, although interesting, after a short trial period was abandoned in favor of the more conventional ones, DCR- and Indi- schemes.

4.5 Instrument characterization

A calibration mass spectrum, obtained with the Jordan time of flight mass spectrometer, is presented in Fig. 4.22. Para xylene (p-xylene or p-xylol) was used, having a molecular mass of 106 Da. P-xylene is producing a range of fragments and is highly fragmenting when ionized with laser light at 266 nm. Many products differing by single hydrogen mass are formed, particularly suited to check the response of our instrument.

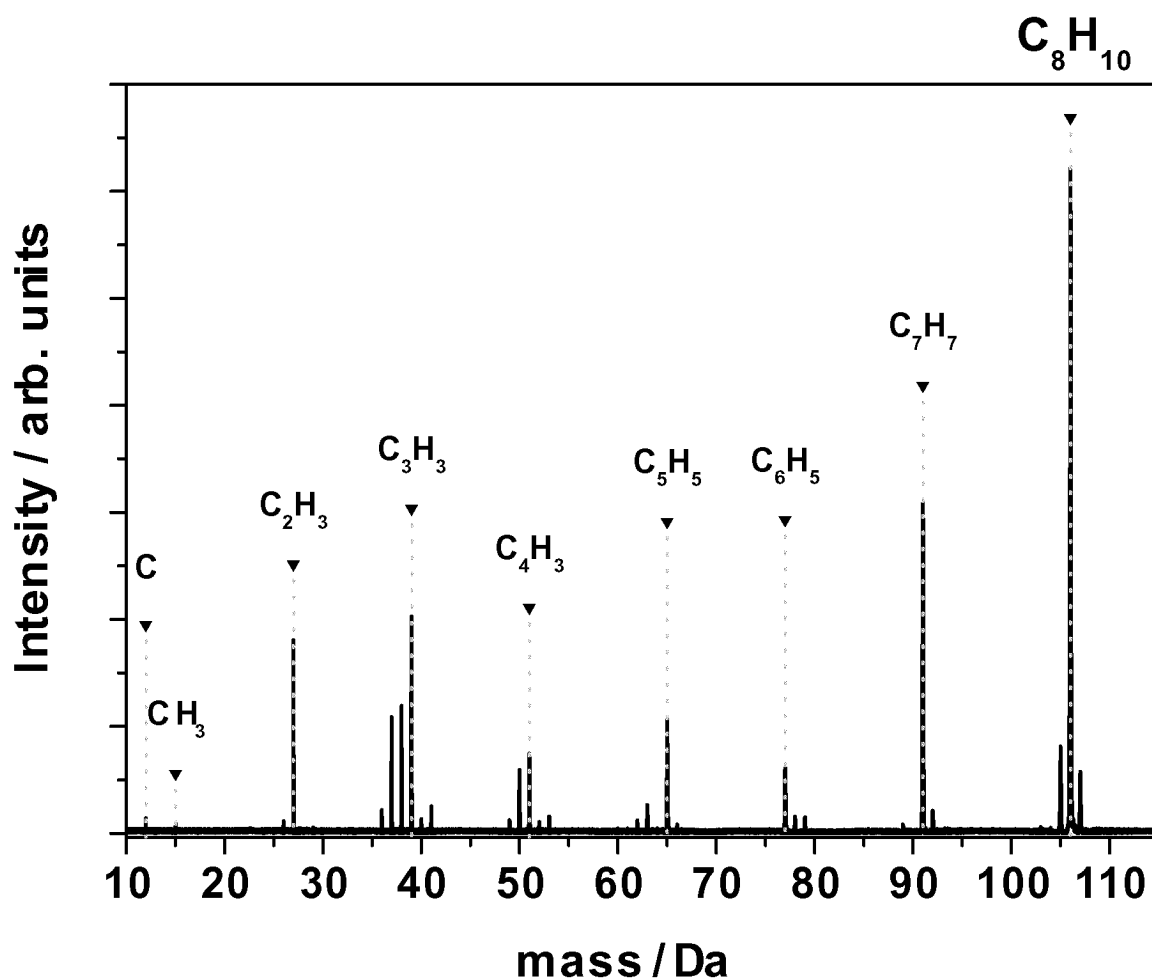


Figure 4.22: The para-xylene mass spectrum obtained by ionizing the molecular beam with a 266 nm laser beam (≈ 150 mJ/pulse). The spectrum was averaged over a hundred of consecutive acquisitions occurring at 10 Hz. The p-xylene is seeded in Ar with a pressure of 2 bar.

4.5.1 Mass calibration

In a Re-ToF-MS instrument the signal measured represents the intensities of the detected ions vs time. An approximate correspondence between mass-to-charge ratio and detection time (time-of-flight) of ions could be determined directly in an “External Calibration” fashion from equations in section A.3 if the exact drift lengths, acceleration and reflectron potentials are known. In practice this approach for the calibration of the mass spectrometer is rarely used.

In most cases, calibration for ToF-MS is performed from empirical determination of the times-of-flight of several known masses. Subsequently, a calibration line is drawn, according to equation

$$\frac{M}{Z} = a(t + b)^2 \quad (4.2)$$

where M is the ion mass (in Da), Z represents the ion charge (in electron charge units), a and b are the calibration constants, and t is the experimental time-of-flight. The calibration constants a and b are determined through a least-squares regression which fits the equation 4.2 with the known pairs of times-of-flight and masses. The result is often more

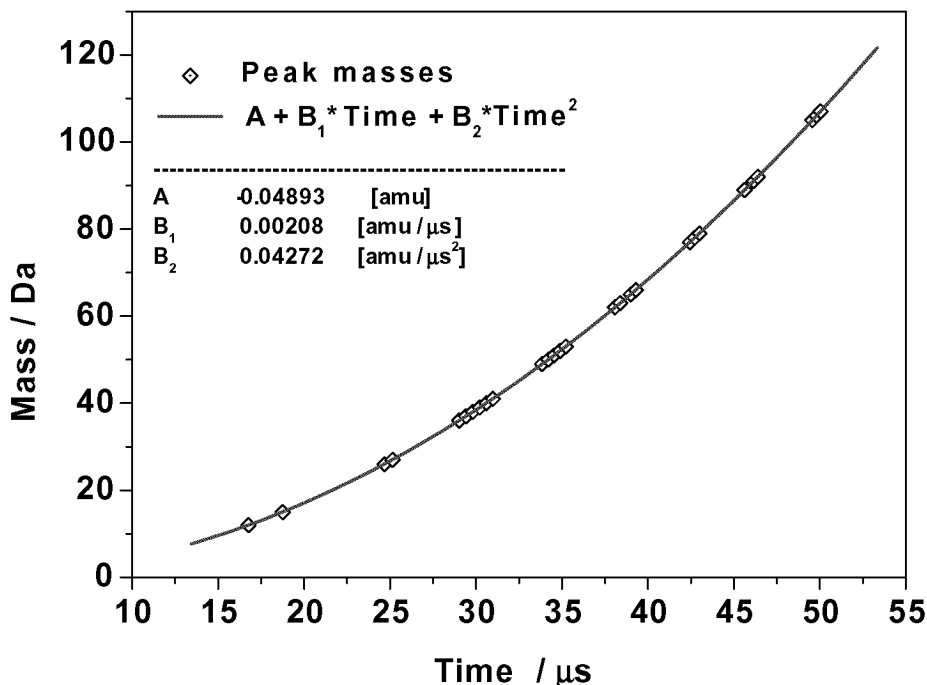


Figure 4.23: Mass versus time plot used for Re-ToF-MS calibration. (M_i, t_i) data points (rhombi) are obtained by guessing peaks occurring at time t_i in the signal by the Re-ToF-MS to be originated by M_i ion masses. Continuous line is a quadratic polynomial which give the best fit to the points.

accurate “Internal Calibration” fashion. After calibration, any experimental time-of-flight can be converted to a M/Z value to identify the unknown ions. Fig. 4.23 shows the curve obtained with internal calibration of the signal acquired using P-xylene (as described in previous section).

Mass calibration with Zn and ZnO samples was straightforward, since zinc provided an appreciable signal with the characteristic isotopic pattern shown in Fig. 5.6. In addition, impurities still present in vacuum, such as H_2O , O_2 , and N_2 could be identified in the signal from the mass spectrometer.

4.5.2 Re-ToF-MS Resolution

Broadly defined, resolution is the ability to distinguish two ions of different masses, and is usually scaled to the mass range under consideration, such that

$$R = \frac{M}{\Delta M} \quad (4.3)$$

where R is the resolution, ΔM is the difference in mass of the species, and M is the average mass of the two ions. Referring specifically to (Re)ToF-MS and assuming a single charge

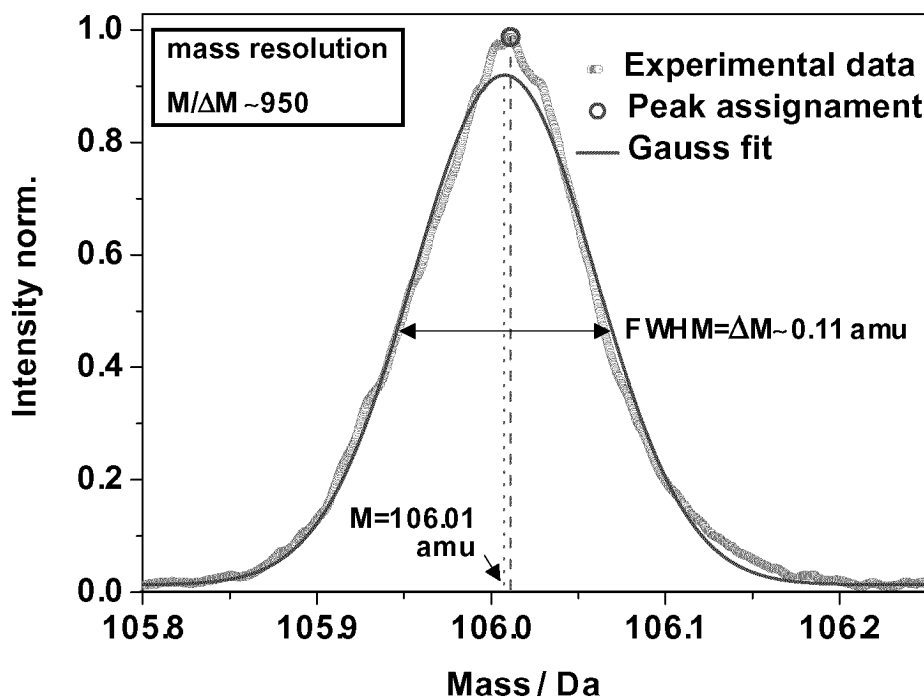


Figure 4.24: Gaussian fit of the peak at 106 Da in Fig. 4.22. The parameters used for the resolution calculation are determined.

on the ion, the resolution equation can be rearranged to yield the equation:

$$R = \frac{t}{2\Delta t_{FWHM}} \quad (4.4)$$

where the Full Width at the Half-Maximum (FWHM) of the signal peak, Δt_{FWHM} , has replaced the masses of the two separate ions. This enables resolution estimates for any given mass based solely on the time-of-flight and peak width.

From equation 4.5.2, it is clear that an increased time-of-flight, t , (long drift length and/or low acceleration potential) or narrowed peak width (Δt_{FWHM}) maximizes resolution. Ideally, this could be done simultaneously, but system parameters usually affect t and Δt_{FWHM} in opposite manners, and all peak-widening factors must be considered to select the parameters for ToF-MS operation. The peak corresponding to the mother molecule of P-xylene which has a mass of 106 Da (see Fig. 4.22), is shown in Fig. 4.24. In order to determine the resolution the mass at which the signal reaches is maximum (M) and the broadening of the peak, ΔM_{FWHM} are also indicated in Fig. 4.24. A resolution of about 1000 is achieved.

4.5.3 Gas Pulse

In order to check how the valve was operating we studied the gas beam expanding into vacuum. We performed measurement with 1% N₂O seeded in Ar. The back-pressure was 4 bar. The N₂O molecules were ionized in the mass spectrometer interaction region with the light at 800 nm of the femtosecond laser system. Assuming that the amount of ions produced

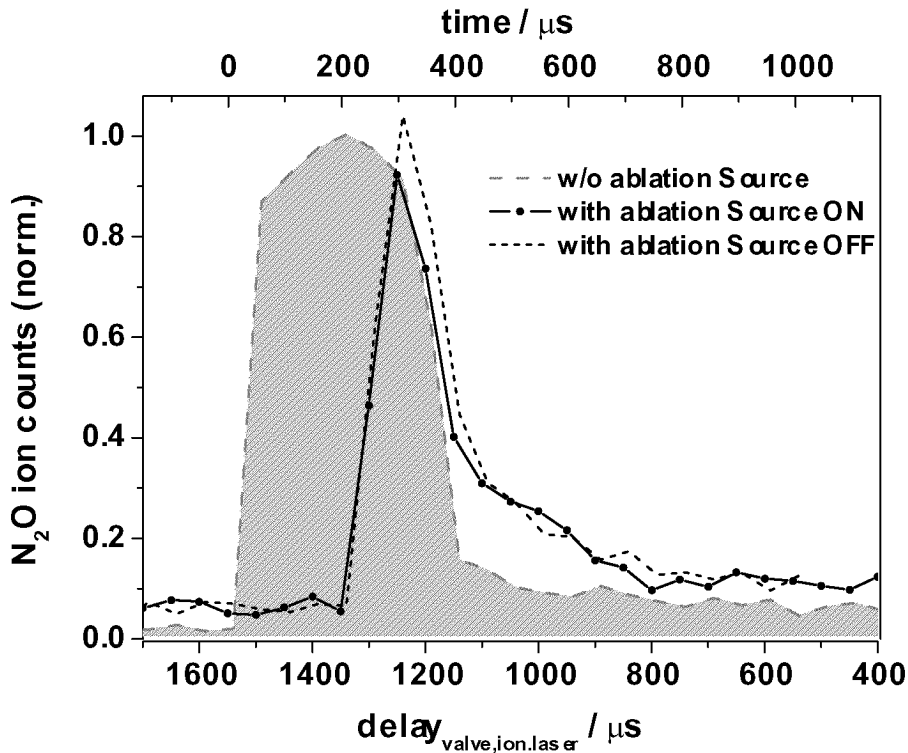


Figure 4.25: Ion intensity of N₂O versus time delay between valve opening and laser ionization (upper thick marks). The measured signal is proportional to the gas density. The scale on the bottom gives the time in microseconds, starting from the rising edge of the shadowed signal.

is proportional to the total amount of atoms and molecules in the beam, we measured the ion signal depending on the delay between the valve opening and the ionization laser shot. In Figure 4.25 we show the resulting traces obtained with the vaporization source mounted but not working (dotted) and working (continuous with circle symbol) respectively. The shadowed trace corresponds to the signal obtained with the bare valve, i.e., the vaporization source removed.

If the measured signal is proportional to the actual gas density in the interaction region, we can draw the following conclusions from Fig. 4.25:

(1) the valve opening time, determined as the full width half maximum of the shadowed trace, is slightly larger than the nominal setting of the valve driver (approx 320 μ s instead of 280 μ s);

(2) The tails of traces obtained with the vaporization source in place (either active or not) are more intense than without; Higher ion signals are observed due to the slower gas removal after the gas pulse. The vacuum degrades when the vaporization source is installed: Because of longer path in the vaporization source, pumping takes more time and the final vacuum, that was reached without Smalley source, cannot be achieved anymore between two gas pulses.

(3) Traces determined with the source and without have rising edges, occurring one after the other, about $250 \mu\text{s}$ apart. The presence of the vaporization source causes the rise of N_2O intensity to start later though the subsequent steep fall does not seem affected. The decay occurs immediately after the maximum is reached. In particular the trailing edge is higher when the source is not active than in the other way round.

4.5.4 H_2O , Ar_xO_y clusters

With the vacuum conditions specified in par. 4.3.1 we checked whether clusters were formed without the vaporization source in place. The system was tested in combination with the Fs-laser. We injected a gas mixture of Ar with 1% O_2 at 4 bar. The valve opening time was $220 \mu\text{s}$ and the femtosecond laser was used. The distance from the skimmer to the nozzle output was set to 5 cm. A mass spectrum, acquired in the region between 75 Da and 600 Da by averaging 1000 times, is presented in Fig. 4.26. Pure argon clusters as well as other aggregates obtained by the addition of O_2 and H_2O could be identified in the mass spectrum (All marked according to legend). It represents the evidence that the vacuum conditions achieved were suitable for cluster formation and very cold conditions could be realized during gas expansion. The strong gas rarefaction that extends the mean free path of contained species beyond the physical dimension of our setup, enables weakly Van-der-Waals bound aggregates as Ar_n to survive, until they are ionized in the interaction region of the mass spectrometer. In order to verify that clusters could be formed in presence of the vaporization source we acquired a spectrum using a water “bubbler” (gas saturation assembly) to make moist the $\text{Ar}+1\%\text{O}_2$ mixture with 2 bar. The bubbler is a device used to seed the vapour above a liquid sample into an inert gas. The gas bubbles through the liquid entraining its vapour.

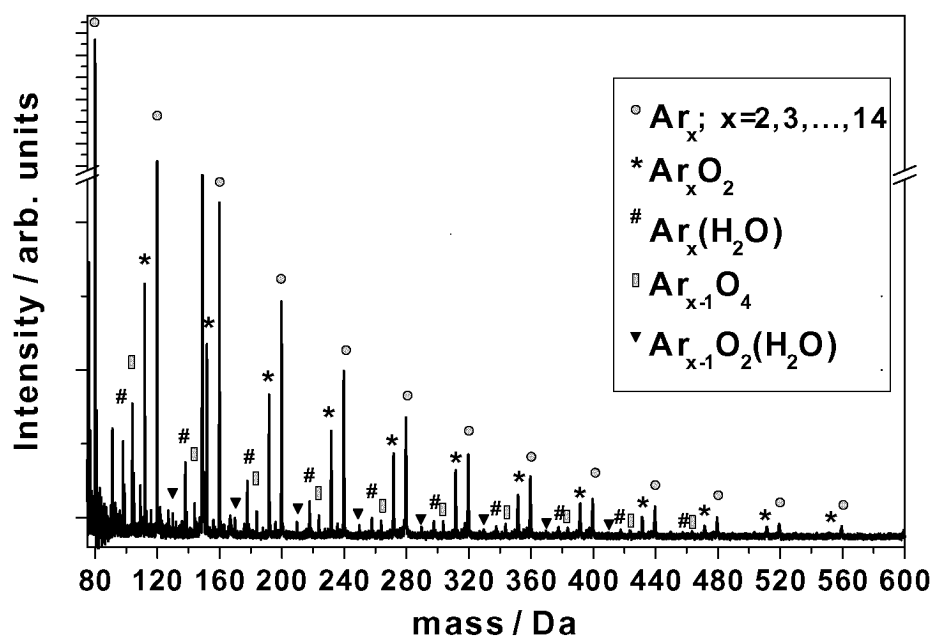


Figure 4.26: Mass spectrum acquired in the region between 75 Da and 600 Da using a gas mixture of Ar with 1%O₂ at 4 bar with the vaporization source not yet installed.

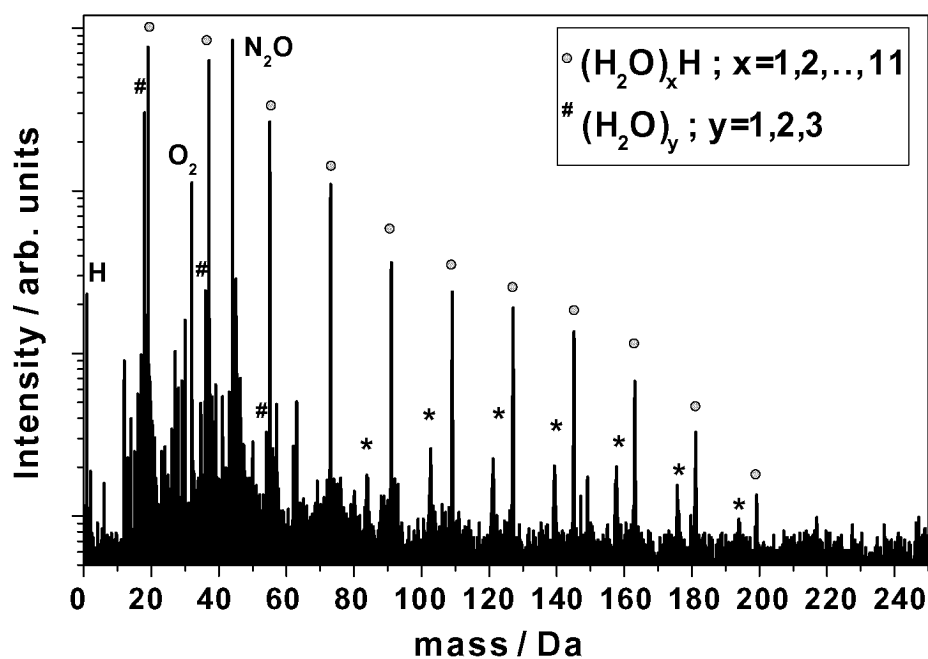


Figure 4.27: Spectrum acquired using a moist Ar+1%O₂ mixture with 2 bar between 1 Da and 250 Da.

In Figure 4.27 we show a portion of the full spectrum, with masses ranging between 1 Da and 250 Da. The exit of the source nozzle was set 30 mm away from the skimmer and water clusters. The most abundant species are protonated water clusters which were also observed in former experiments [73].

4.5.5 Ablation laser energies

The used ablation laser energies per pulse were chosen based on the ease of ablation for the particular samples. Care is taken to avoid signal saturation effects and damage to the multichannel plate detectors. To measure the pulse laser energy, a power-meter with a detection head optionally intercepts the laser beam at the entrance of the vacuum chamber. The observed pulse energy at this location is reduced to account for the $\sim 8\%$ attenuation of the quartz window on the vacuum chamber. For most analysis, the pulse energy ranged between 0.25 mJ and 5 mJ, after the laser attenuation described in section.

To control the beam focused on the sample, an adjustable lens is installed to maximize the ion yield (proportional to the observed signal on the oscilloscope, see section 4.5.7). The beam size is viewed on a white card and measured with a Vernier caliper at the position of the 35 cm focal length lens. The beam radius depends on the laser energy used, as higher laser energies produce a larger beam radius (~ 0.95 cm) and lower energies yield a smaller radius (~ 0.80 cm). For typical analysis with an energy setting of ~ 2 mJ, the radius is approximately 0.85 cm to 0.90 cm. The measured radius at the lens can be used to approximate the beam spot size at the focal point assuming Gaussian beams:

$$d = \frac{4f\lambda}{\pi d_0} \quad (4.5)$$

where d represents the beam diameter at the focal point of the lens, f represents the lens focal length, λ is the wavelength of the laser light, and d_0 is the beam diameter as measured at the lens. The beam size at the sample surface thus translates to a diameter of $13 \mu\text{m}$ to $14 \mu\text{m}$, yielding an area of $136 \mu\text{m}^2$ to $153 \mu\text{m}^2$. Laser energy densities when using 2 mJ are then calculated to vary between 13 and 15 J/mm^2 .

4.5.6 Zinc desorption

The evaporation rate of zinc ablated by laser pulses at 266 nm was determined by measuring the weight loss of the zinc rod after N laser shots. We injected Ar+1% O₂ at 5 bar through the valve with a opening time of 250 μs . The 266 nm light emitted by the Nd:YAG laser with pulse energy of 2.5 mJ was used. The values for consecutive sets of measurements are reported in table 4.4. Figure 4.28 shows the weight loss per shot (net mass ablation) with the corresponding number of laser shots. In order determine the weight loss corresponding to N laser shots, we proceeded to weight the rod of zinc before starting an experiment. With

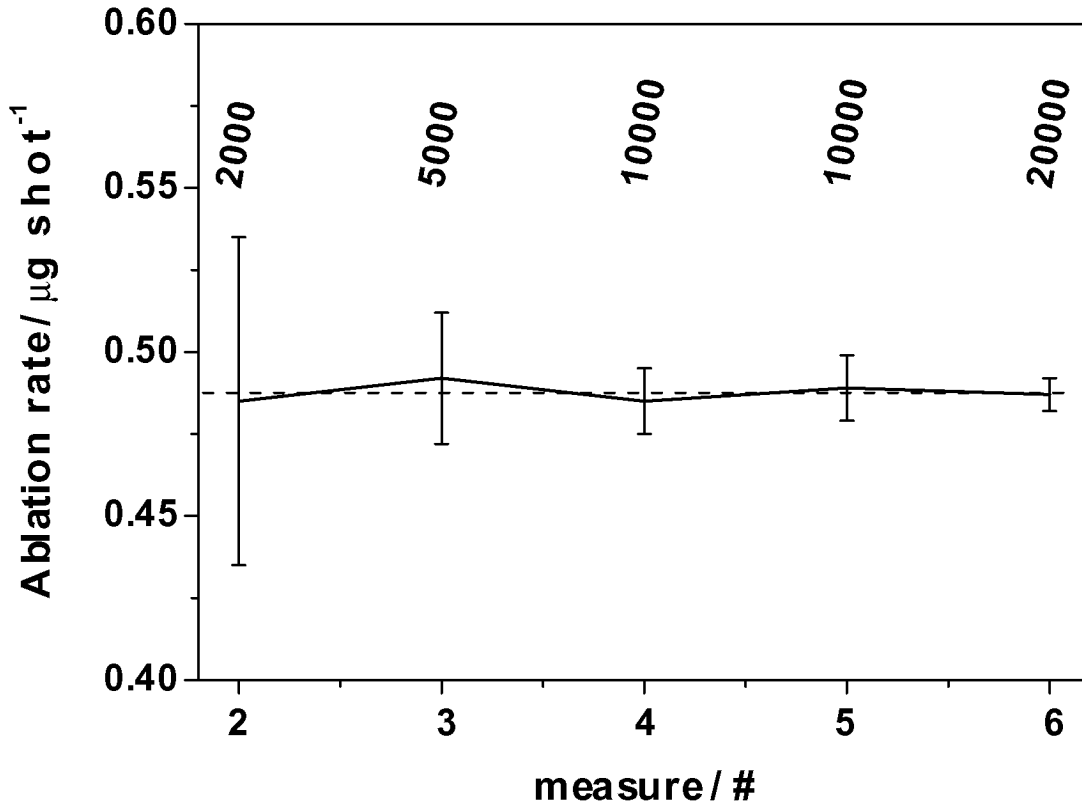


Figure 4.28: Mass ablation per laser fire as determined in a series of measurements for the number of laser shots indicated at the bottom. The resulting yield of zinc per shot is of about $0.5 \mu\text{g}$.

the rod back in the apparatus, we switched the pumps on to reach the typical high vacuum conditions of our experiments. After half an hour, we checked the alignment of the ablation laser and let it fire with power attenuated to 25 mW. A train of TTL pulses, as described in the timing section 4.4, was generated by the BNC 555 pulser unit triggering the ablation laser. Furthermore the laser shots were monitored on the oscilloscope via a photodiode. The oscilloscope was used to count the number N of times the photodiode signal had raised above a certain threshold value during an experiment. The value of N determined coincide with the number of laser shots that effectively occurred.

From data obtained in table 4.4 we can infer for zinc an evaporation rate of $0.5 \mu\text{g}/\text{shot}$ in the given experimental conditions. The number of evaporated ^{64}Zn isotopes ($N_{64\text{Zn}}$) per second is computed from equation:

$$N_{64\text{Zn}} = f \frac{N_A}{A} N_{\text{Zn}} \quad (4.6)$$

where f is the ^{64}Zn relative isotopic fraction, N_A is the Avogadro's number, A is the Zn atomic weight, and N_{Zn} represents the estimated Zn rate. Values of $N_{64\text{Zn}}$ in the order of 10^{15} isotopes are obtained. In Fig. 4.29 three photos of the zinc/zinc oxide rods, taken

# of shots (N)	Initial weight [g] $\pm 5.00 \times 10^{-5}$	Final weight [g] $\pm 5.00 \times 10^{-5}$	Weight loss [g shot ⁻¹]
1	-	-	-
2000	8.99758	8.99661	$(4.9 \pm 0.5) \times 10^{-7}$
5000	8.99661	8.99415	$(4.9 \pm 0.2) \times 10^{-7}$
10000	8.99415	8.9893	$(4.85 \pm 0.10) \times 10^{-7}$
10000	8.9893	8.98441	$(4.89 \pm 0.10) \times 10^{-7}$
20000	8.98441	8.97467	$(4.87 \pm 0.05) \times 10^{-7}$

Table 4.4: Table of the weight loss of a Zn rod determined after N laser light shots with the conditions described in the text.

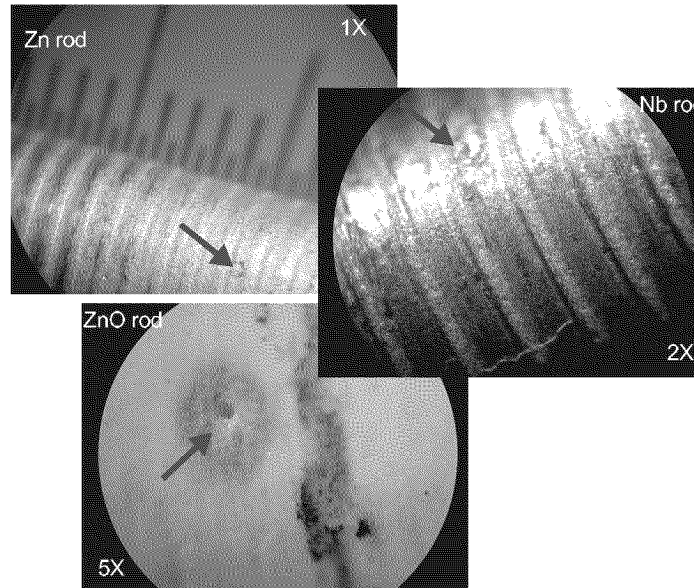


Figure 4.29: Three photos of Zn and ZnO rods are shown. They are shots of a camera used in combination with a microscope. The photos were taken with various magnification of the microscope: 1X, 2X for Zn and 5X for ZnO, as indicated by the labels on each photo.

with a microscope, are shown. They illustrate the digging marks produced by the laser ablation action on the surface of Zn and ZnO rods at various magnification (1X, 2X, 5X). For reference, the photo at 1X was recorded with a ruler in the background. The ruler exhibits a graduated scale with 0.5 mm increments. Continuous helicoid trails are visible at the Zn surface in both photos taken at 1X and 2X. They are produced by the focused laser output beam impinging on the surface of a rod, repetitively screwed up and down along its own revolving axis of symmetry (see section 4.2.2).

A surface mark was produced by 10 pulses of laser light impinging over the same spot.

In all photos of Fig. 4.29 the corresponding craters are indicated by arrows. The craters obtained on Zn and ZnO surfaces have about 150 μm diameters. These dimensions are ten times larger than the ones of the Gaussian beam waist computed at the rod surface, where the laser beam is focused by a lens 350 mm away. Therefore, the area of the beam at the focal point is 100 times larger than expected (see section 4.5.5). Accordingly, when we use a beam with 2 mJ pulse energy, the laser energy densities assume values up to few hundreds of mJ/mm^2 .

4.5.7 Number of ions detected

Peak area data obtained after integration experimentally estimates the number of ions detected. The output from the multichannel plate detectors, an electrical current, is directly related to the number of ions that strike the multichannel plate. By knowing the termination resistance (R) and the gain of the detector (G), the following relation estimates the number of ions associated to a given peak [74]:

$$V_p = R \times i_p = R \frac{GNq}{\Delta t} \quad (4.7)$$

where V_p and i_p are the peak voltage and current respectively, Δt is the peak width (FWHM), q is the charge of an ion, and N represents the number of ions detected. Integration of the area under the peak gives therefore $V_p \times \Delta t$ which is proportional to N . In our experiments G varied between 10^5 and 10^6 while Zn peaks of few hundreds of mV (V_p) were observed on the oscilloscope with $R = 50$ ohm. Their widths were typically of 20 ns (Δt). Using these values in eq. 4.7, N is found to range between 500 and 5000 ions.

4.5.8 Contaminants

During our measurements we recognized that some features appearing in our spectra could be attributed to the presence of polluting species in the experimental apparatus. Traces of these unwanted species were determined by measuring the mass spectrum when the vaporization source was either not in place or installed but not working. Interesting information could also be derived from the analysis of the mass spectra when the valve was shut off.

The mass spectra measured from 1 Da to 175 Da with (upper trace) and without (middle trace) the vaporization source are shown in Fig. 4.30. The rod in the vaporization source was made of zinc.

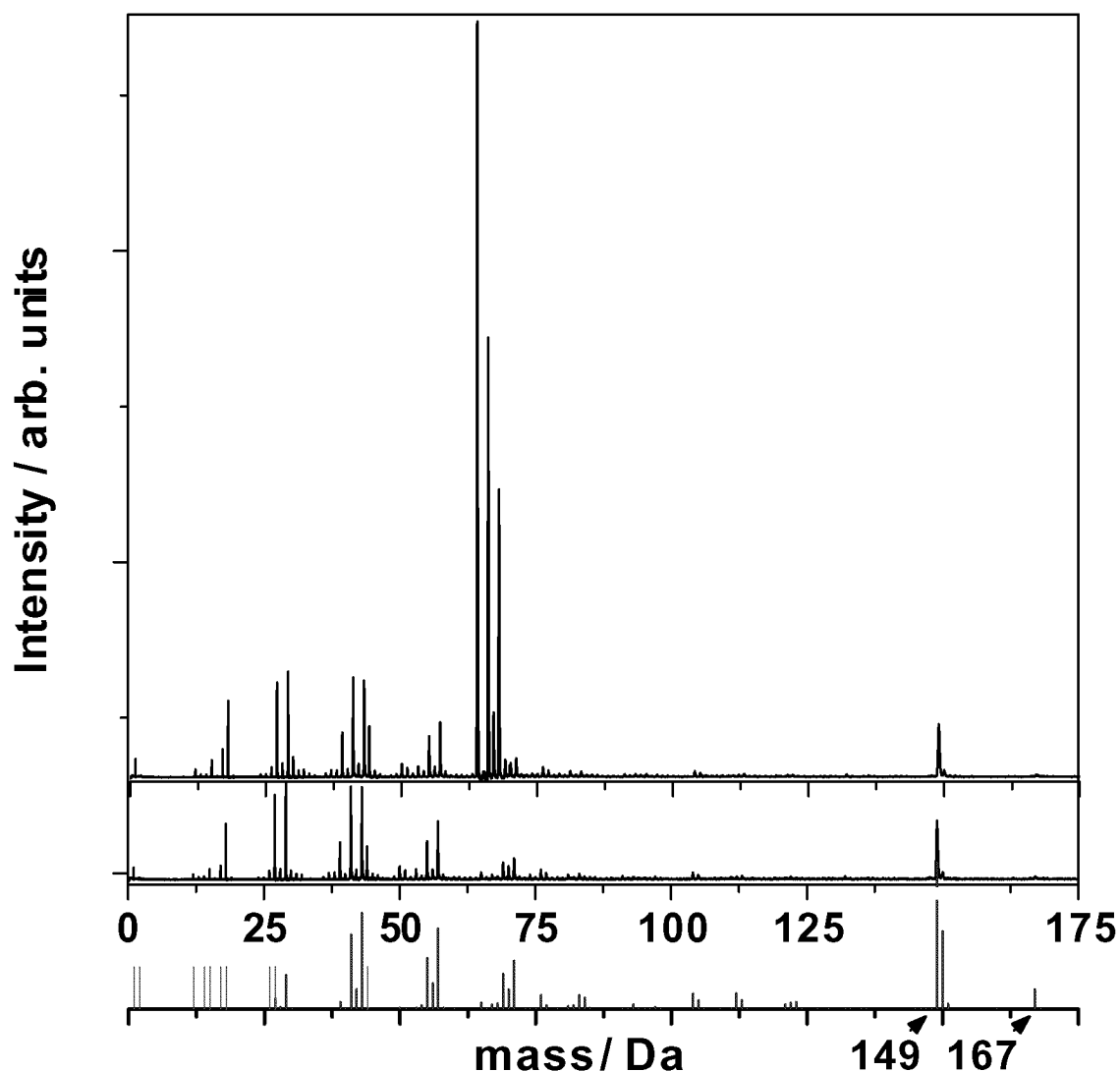


Figure 4.30: Mass spectra obtained in a mass range from 1 Da to 175 Da with (upper trace) and without (intermediate trace) the vaporization source running. Peaks occurring at the same masses in both the spectra, are found mostly similar (also in the intensity distribution) to those characteristic of a contaminant, Di-n-octyl phthalate, whose mass spectrum from NIST is shown at the bottom.

The power of the ablation and the ionization laser beams was 30 mW and 2 mW respectively. Helium, with a back-pressure of 3 bar and seeded with 1% N_2O , was injected through the valve. The opening time of the valve was $260 \mu s$. The distance between the exit of the nozzle from the skimmer was 30 mm. Identical peaks in both spectra can not be assigned to any of the species introduced during the experiments in the vacuum chamber. However, the observed peaks in the spectra could be rather attributed to one or many contaminants. It is difficult to determine which are the parent molecule giving rise to the manifold of ions observed. However from a search of typical contaminants in high vacuum we found a plas-

ticizer such as the Di-n-octyl phthalate ($C_{24}H_{38}O_4$) to be a good candidate. In Fig. 4.30 the mass spectrum taken from NIST database (lower trace) is shown together with the peak positions of water, N_2O , C_2O , and their fragments (indicated with the same intensity). All together their contribution gives a reasonable explanation for many of the peaks visible in the experimental spectra (middle and upper traces in Fig. 4.30).

The characteristic pattern was evident in many of our mass spectra but not in all of them. It seemed to appear when the vaporization source assembly was installed into the vacuum chamber. But we could not clearly identify with which part of the assembly the contaminants were introduced (electrical wire isolation, gear fay, etc.).

4.5.9 Zn yield versus experimental parameters

The spectra we collected using our experimental setup were dependent on several experimental parameters.

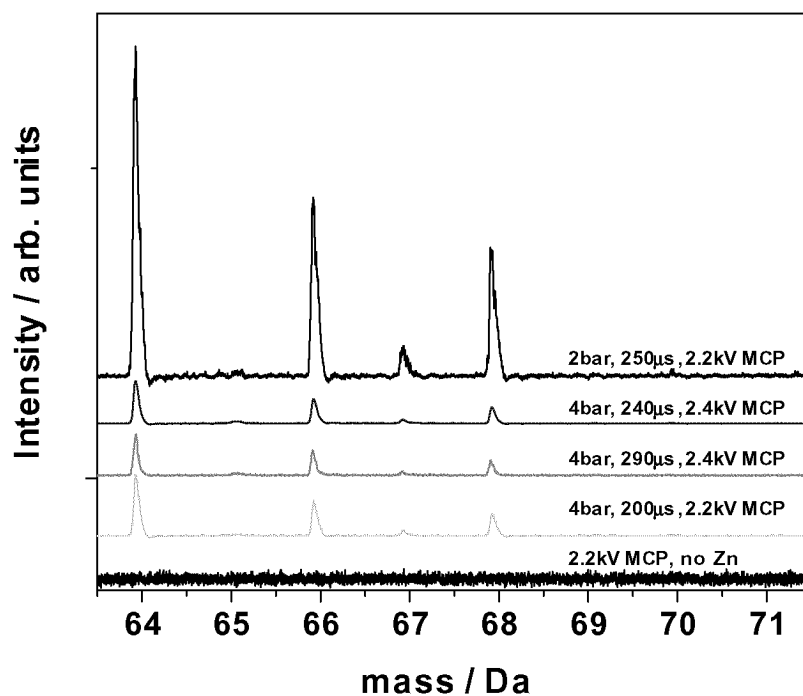


Figure 4.31: Optimization of Zn^+ signal. A range of measurements are shown for different back pressures of Argon, valve aperture times and detector sensitivities.

The effect of some of this parameters is illustrated in Figure 4.31 where Zn spectra were measured in the mass interval between 63 Da and 72 Da, while Ar back pressure, valve aperture time, detector sensitivity, were changed.

A multivariate analysis would be useful to determine how each parameter affects the spectral features. This approach would require to compare the spectra obtained for different parameters in a multidimensional space. Out of this we performed our measurements with parameters values chosen to maximize a single feature, e.g. the Zn yield. After a set of parameters was identified, a restricted analysis could be executed by tweaking parameters one after the other (parameters sweeps).

Zn vaporization and ablation laser intensity

The output light emitted by the ablation laser was dimmed using an optical unit, the “beam attenuator”. The beam enters the attenuator unit through a 1 cm diameter aperture on one side and exits with reduced intensity from an opposing aperture with same sizes. The ratio between intensities of the beams emerging and entering the attenuator, represents the attenuation factor (usually expressed as a percentage).

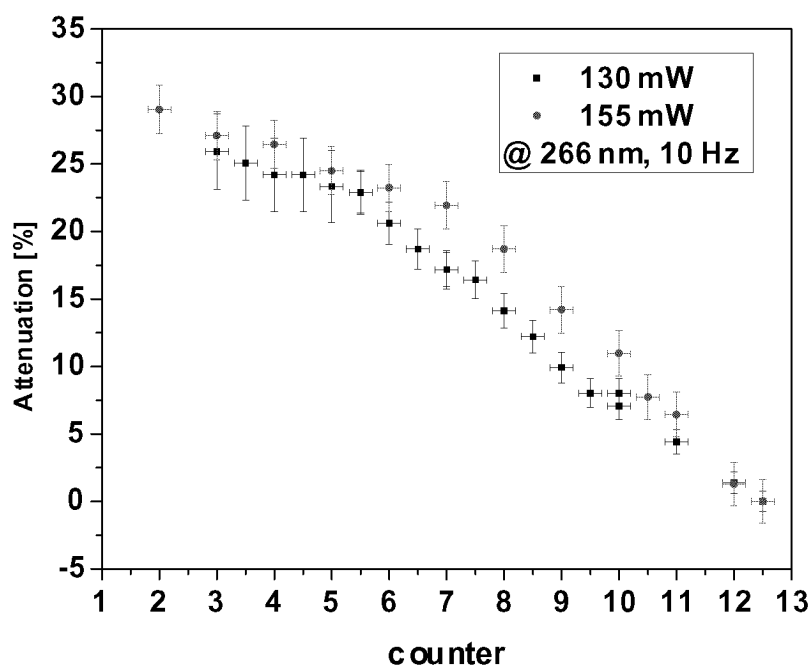


Figure 4.32: The intensity fading obtained by turning a graduated knob is represented in this plot for two different input laser powers (155 mW: red circles, 130 mW: black squares). The attenuation counter ranges from 2 to 12.5.

The attenuation factor can be modified by acting on a knob. The position of the knob is associated to a scale ranging from 0 to 14 with thick marks every 0.5. In the following we refer to the knob positions as the values of the attenuation counter.

The attenuation factor was measured for a 266 nm output beam delivered at 10 Hz by the

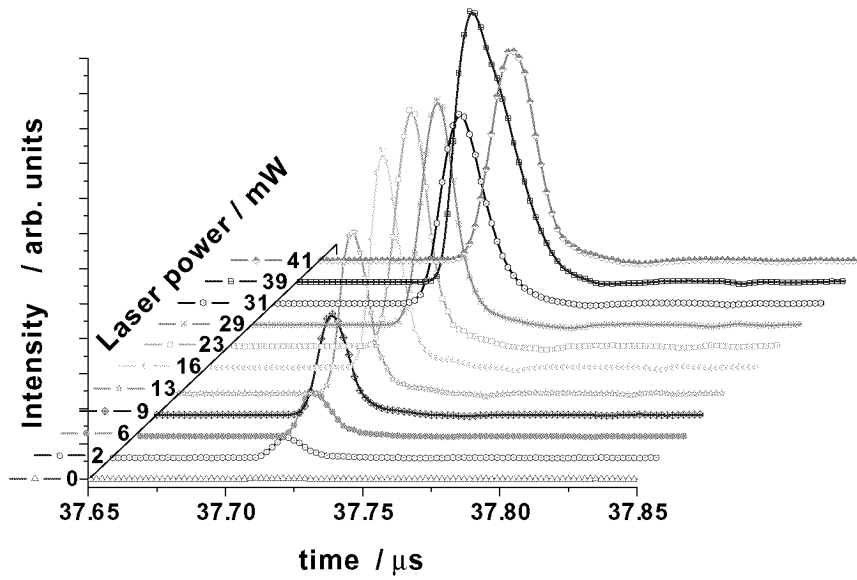


Figure 4.33: ^{64}Zn intensity measured with the mass spectrometer in the ion detection time domain. In a pseudo-3D plot are shown the data obtained for some power values of the ablation laser output beam, ranging from 0 mW to about 41 mW.

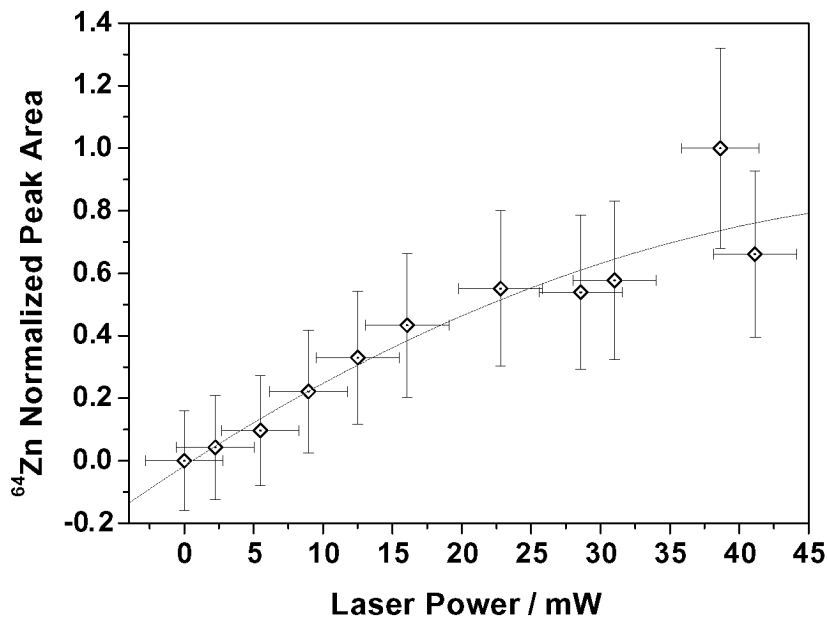


Figure 4.34: Areas beneath ^{64}Zn peaks of Fig 4.33, normalized to their maximum value, are plotted versus the power of the ablation laser output beam.

Spectra Physics Nd:YAG DCR-2A laser. Two initial values of power were considered for the incoming laser beam: 155 mW and 130 mW. The first value corresponds to the the maximum value of power achievable with the laser fourth harmonic output. The second value represents the regime output power of the laser beam attained by power weakening after extended time of laser usage.

In Fig. 4.32 the results corresponding to 155 mW (red circles) and 130 mW (black squares) are plotted versus the attenuation counter values. The errors on the abscissa were assumed equal to the reading error of the knob scale.

Laser system	type	Pulse Energy [mJ]	λ [nm]
DCR-2A	Nd:YAG	3	266
Clark MXR	Fs-Laser	8×10^{-2}	790

Valve aperture time [μ s]	Gas Mixture
270	4 bar Ar+1%N ₂ O

Lens, Grid, Plate	Operating potentials [V]
Extraction (Repeller) plate	1700
Acceleration grid (V_{A2})	625
Liner (VG)	0
Ion focusing lens	250
Deflection plates (Mass gate)	150
Reflectron front/entrance lens	750
Reflectron rear/exit lens	1250
MCP	-2200

Table 4.5: Experimental conditions used for measurements we performed to characterize the initial kinetic energy of zinc ions (see in the text).

The uncertainty on the values of the attenuation factor was computed via error propagation

using the power-meter reading errors (varying between ± 1 mW and ± 2.5 mW according to the power-meter scale).

For each of the beam powers, the values of the attenuation factor decrease monotonically as the attenuation counter increases, ranging from about 30% to 0. The values of the attenuation factor in the two cases differ by up to 30%.

Attenuation counter values above and below 6 exhibit distinct linear behaviors with a slope that become steeper at higher values.

In order to qualitatively characterize the Zn vaporization with increasing laser beam intensity, we determined the zinc mass spectrum for fluences ranging from 0 J/cm^2 to 12.5 J/cm^2 , with measurement conditions summarized in table 4.5.

Figure 4.33 shows the signal associated to ^{64}Zn peak, plotted versus time for different

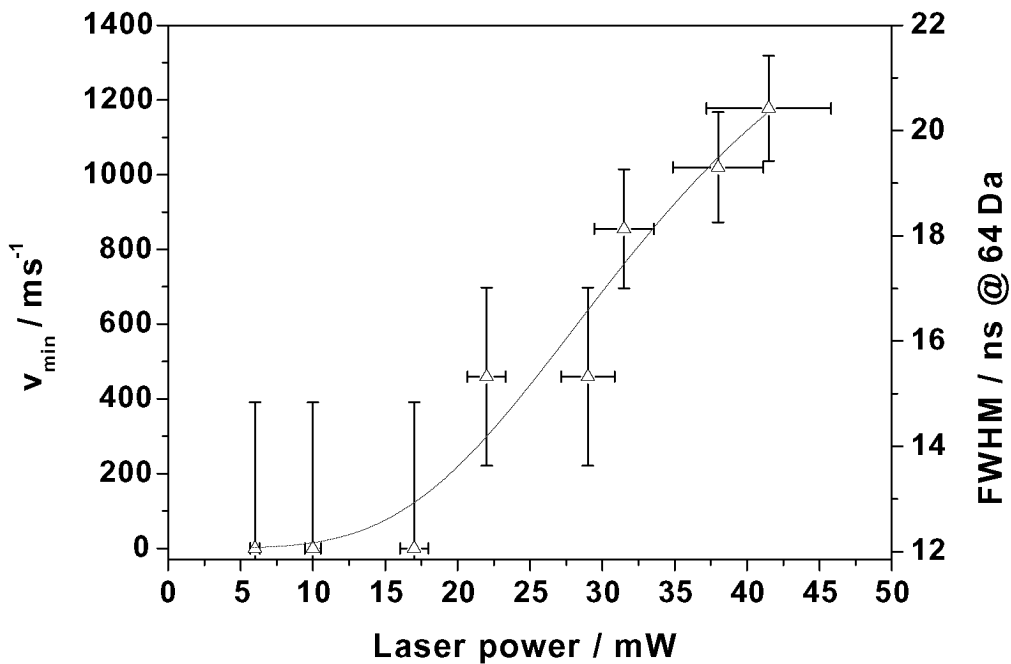


Figure 4.35: FWHM of ^{64}Zn peak (right y-axis) versus ablation laser power of the 266 nm output beam with 10 Hz frequency. Each measured peak broadening with indicated FWHM value could result from a contribution of the ion initial velocity distribution with values in the interval $[-v_{min}, v_{min}]$. The ordinates on the left axis show the computed velocities, v_{min} for the values of FWHM indicated on the right-hand-side.

powers of the ablation laser. Multiple traces, corresponding to increasing values of power for the ablation laser output beam, are illustrated along the oblique axis. Intensities of each spectrum were normalized to the area beneath the peak associated to N_2O .

The area beneath the ^{64}Zn peaks was determined. The corresponding values are shown as a function of the laser beam output power in Fig. 4.34, with intensities normalized to the

highest value of area computed.

For a given set of voltages applied across the electrodes of the Jordan Re-ToF-MS, the ^{64}Zn isotope broadening increases when the impinging laser power steps up. Figure 4.35 shows the full width half maximum (FWHM) of ^{64}Zn peak (ordinate axis on the right hand-side) versus the output power of the ablation laser. The FWHM of the peaks can be related to the minimal kinetic energy of measured ions. In Fig. 4.35 the velocity (left y-axis) is estimated by comparison between the FWHM of the peaks and the response function of the detection system (see Appendix A, section A.4).

Chapter 5

Results

The results of mass spectrometric detection of species formed in a molecular beam obtained by expanding laser ablated zinc (Zn) and niobium (Nb) together with H₂O, O₂ or N₂O seeded in a rare gas (Ar, Ne, He) are summarized in this chapter. All measurements were performed with the ToF-MS setup described in the previous chapter, which allowed us to sample ions with masses ranging from 1 to 800 Da.

For zinc ablation, we used light at two different wavelengths (532 nm and 266 nm), in order to observe a potential influence of the excitation of zinc atoms on the ZnO formation. Nb was ablated by the second harmonic (532 nm) output beam of the DCR-2A laser operating at 10 Hz. In our experimental apparatus we were able to determine the presence of Zn and Nb oxides though marked differences in their abundance were evident. The poor ZnO signals obtained in the mass spectra suggest that the oxidation of Zn is quite exceptional when compared to that of other metals eg. Nb.

Several gas mixtures ranging from pure (99%) O₂ and N₂O to their lean dilutions in He, Ne, and Ar have been used for expansion of the zinc plume. The possible impact of the laser power on the cooling of zinc after expansion has been characterized quantitatively by relating the broadening of zinc peaks with the transversal thermal velocity (section 4.5.6). Zinc compounds containing oxygen could be observed only with lean mixtures of a few percent of seed gas in a noble gas.

We could show that neutral ZnO and ZnOH is produced in our experiment. Due to the characteristic Zn isotope distribution, the zinc containing compounds, ionized with a 100 fs laser pulse (for a description of the laser system, see section 4.2.3), could be unambiguously be identified with the time of flight mass spectrometer (section 4.3.1).

5.1 ZnO sample

Spectra were also recorded using a rod of poly-crystalline ZnO obtained by hot deposition (Goodfellow, ZN529300, 99.9% zinc oxide-sputtering target). We did not find out the ZnO rate of desorption quantitatively as we assumed ZnO ablation was well exceeding the Zn one for the yield of material. After laser ablation, the surface of the ZnO sample exhibited deeper craters than those produced on the Zn surface for the same pulse energies of the impinging laser beam.

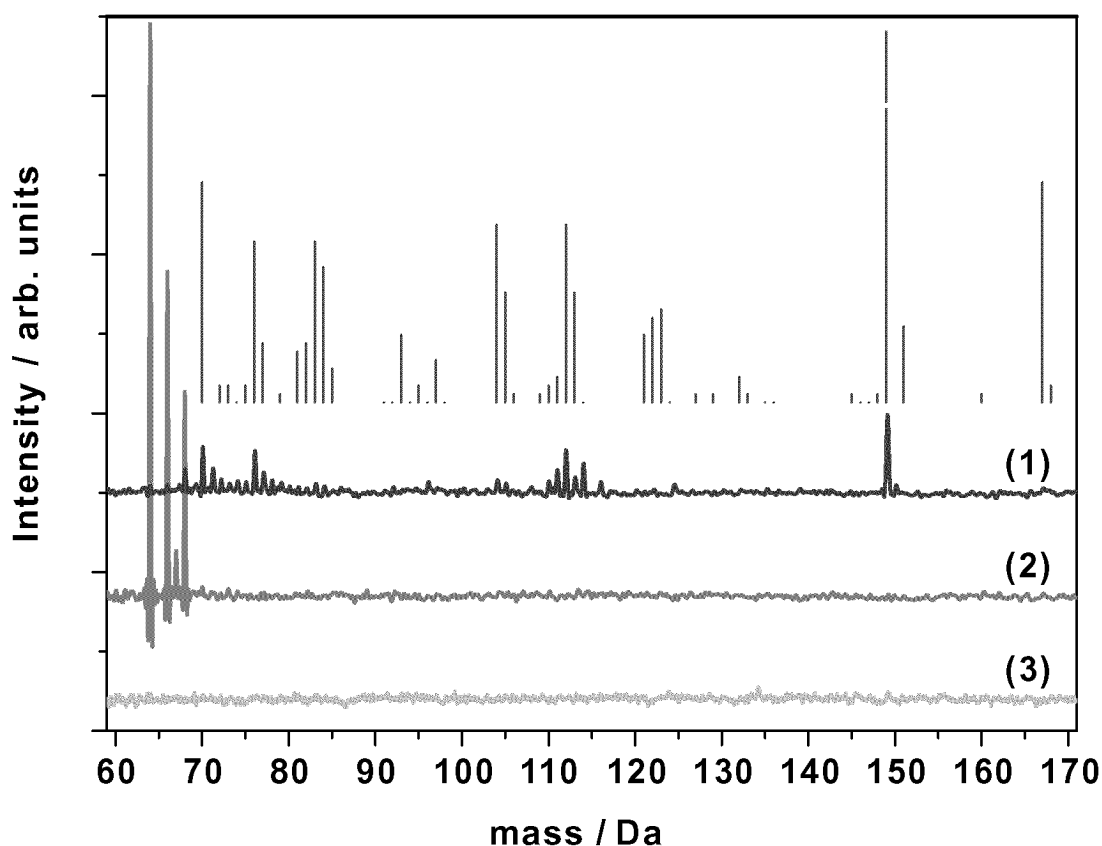


Figure 5.1: Mass spectra measured in the interval between 60 Da and 170 Da. When ablating the ZnO sample, the valve let enter Ar at 4 bar back pressure. Results were not appreciably modified by the addition of 1% N₂O (O₂). (1) MCP highest sensitivity and the mass gate activated; (2) MCP intermediate sensitivity and mass gate off; (3) MCP intermediate sensitivity, without ablation laser and mass gate off. Vertical lines indicate the intensities and relative positions of the C₂₄H₃₈O₄ contaminant fragments.

Accordingly the energies of the ablation laser output at 266nm were varied in a more restricted interval, ranging from 3 mJ to 5 mJ. We first performed the measurements ablating ZnO in an argon gas stream. Subsequently we seeded the entraining gas with 1% of O₂ or N₂O, in order to study how the ZnO compounds were affected. The back pressures

were changed from 2 bar up to 5 bar in an attempt to increase the signal of Zn and O compounds observed in the spectra. The aperture time of the valve was set to $260 \mu\text{s}$ and slightly adjusted around this value in order to enhance the signal of eventual ZnO clusters in the molecular beam. We used the vaporization source with Typ 2 geometry, sketched in Fig. 4.6). The vaporization was positioned in the vacuum chamber, 3.5 cm away from the skimmer.

Despite all efforts, no clear traces of neutral ZnO compounds were evident in the spectra collected. We could not find a condition in which the combination of the parameters enhanced the Zn and oxygen reaction yielding ZnO compounds in the molecular beam. Furthermore, the addition of oxygen containing molecules to argon did not result in significant changes either. In Figures 5.1 and 5.2 we show the spectra collected globally between 1 and

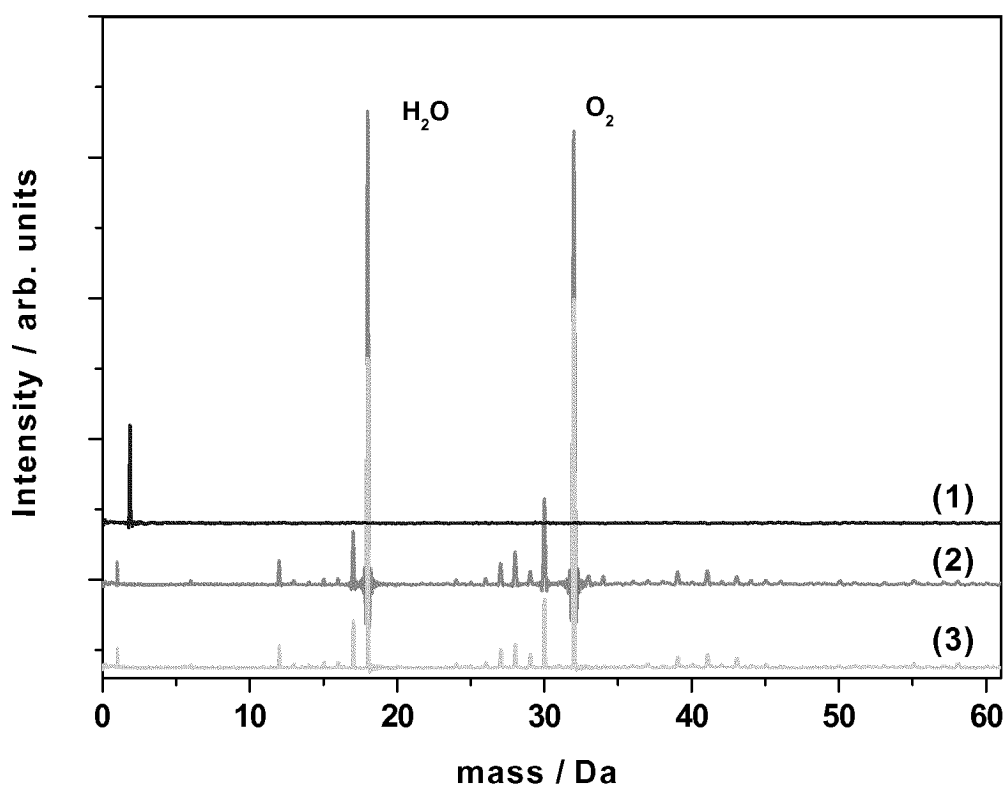


Figure 5.2: Mass spectra obtained in the range of 1–59 Da by the ablation of ZnO in Ar at 4 bar back pressure. Results were not appreciably modified by the addition of 1% N_2O (O_2). Conditions for obtaining traces (1), (2), and (3) are those of Fig. 5.1

170 Da with the ablation of ZnO in Ar at 4 bar back pressure. Three traces are shown from top to bottom. They correspond to the mass spectrometer signals acquired with: (1) the photomultiplier set to the highest sensitivity and the mass gate activated to cut low masses (below 70 Da); (2) intermediate sensitivity of the photomultiplier and mass gate off; (3)

intermediate sensitivity of the photomultiplier, ablation laser not running and mass gate off. The data measured in case (3) are used as a reference spectrum to analyze the other spectra. All traces showed in Fig. 5.1 were smoothed by adjacent averaging of 15 samples. Vertical lines, also depicted in Fig. 5.1, give the mass positions and relative intensities of the $C_{24}H_{38}O_4$ contaminant fragments.

From the analysis of the mass features in Fig. 5.1 we could not assign any of them to ZnO compounds due to the unfavorable signal to noise ratio. The peaks that are observable between 106 Da and 116 Da could be determined by the presence of cadmium Cd, a known impurity (0.0005% max) of the ZnO sample, together with some of the $C_{24}H_{38}O_4$ fragments. A fit of the measured spectrum (1), with using variable concentrations of Cd, $C_6H_6O_2$, $C_6H_7O_2$, and $C_6H_8O_2$, and $C_6H_{10}O_2$ was performed in the given mass interval. The result that best describe the experimental data were obtained for the following relative abundances of species: Cd(81%), $C_6H_{10}O_2$ (7%), $C_6H_8O_2$ (4%), and $C_6H_7O_2$ (7%), with $C_6H_6O_2$ and $C_6H_9O_2$ accounting for the remaining 2%. However, in Fig. 5.2, comparing the two lower traces, we observe that, as expected, the incidence of O_2 is augmented by the ablation of ZnO.

5.2 Nb_xO_y clusters

In contrast to a poor yield of oxygenated compounds with zinc, we obtained good signals when ablating niobium, which was used as a control for the proper functioning of our setup. Experiments by other researchers [75, 76], demonstrate that Nb readily forms oxidized clusters in similar conditions as we used in our experimental setup. Niobium is a transition metal of group V and has an electronic structure of $[Kr]4d^45s^1$. Nb forms clusters that exhibit strong directional chemical bonds that results in well defined structures [77]. Stable oxides are Nb_2O_5 and Nb_2O_3 . The former is an ionic compound, in which the niobium atom donates all five valence electrons to oxygen, and both niobium and oxygen ions have completely filled s and p shells [78]. Accordingly, Nb_2O_5 , NbO_2^+ , and $Nb_3O_7^+$ are expected to be stable species too, and indeed these species were observed in a molecular beam experiment [79]. Solid niobium oxide with Nb_2O_5 stoichiometry finds applications along with ZnO as insulation material in solar cells and is not the object of current research. However the experimental work of Heiz et al. [76] with a laser ablation source suggests a strong presence of Nb_xO_y molecules without stoichiometric constrictions if rapidly

stabilized in a molecular beam by cooling. The oxidation of Nb is also found to occur by the adsorption of oxygen to a niobium clusters, either pure or containing molecules like CO or H_2O . An analysis of the kinetics of reaction $\text{Nb}_n + \text{O}_2$ can be found in [80]. Calculations for predicting the electronic structure of Nb_n with $n=2$ to 23 have been performed, allowing the correlation of the stability of individual molecules with respect to their reactivities [81].

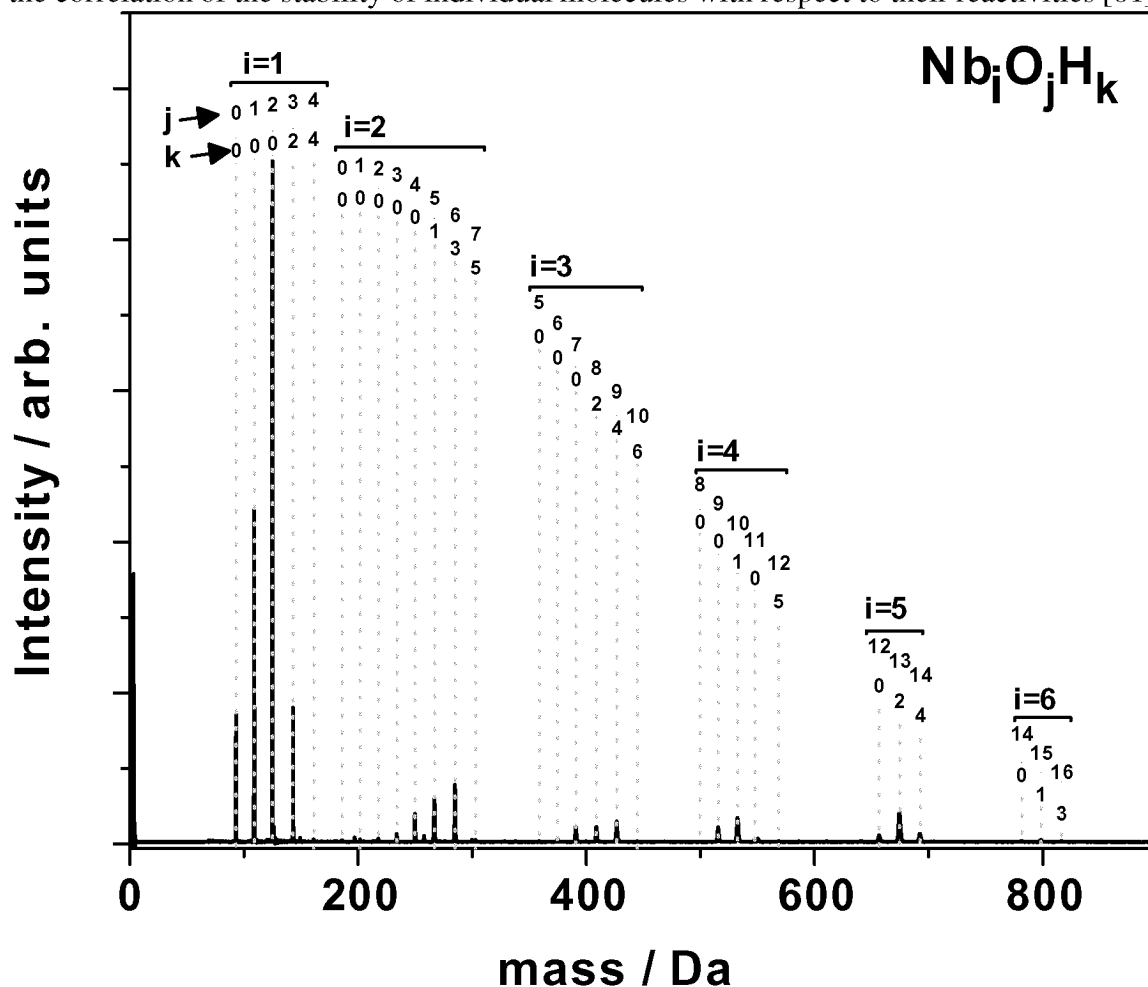


Figure 5.3: Distribution of niobium oxide clusters produced from a laser-induced plasma reaction of niobium with oxygen.

The ablation source with design 4.6 was used to generate niobium and niobium oxide clusters in our experiments. A rod of niobium with high purity (Goodfellow, 99.9%) was used and Nb ablation was performed with 2nd harmonic output of the DCR-2A Nd:YAG laser pulse of energy up to 35 mJ. The femtosecond laser system was set to 1.5 μJ per pulse. The high voltage pulser was used to reject all ions with masses below 80 uma from detection. We injected 1% O in Ar through the pulsed valve. The nozzle through which the gas expanded into vacuum had a length of 2 cm and outer diameter of 8.5 mm. The end facing vacuum opened as a cone of 60°. The distance between the skimmer and the nozzle of the

ablation source was set to 3 cm.

The spectrum, obtained by averaging over 5000 acquisitions is shown in Fig. 5.3. The peaks observed between 1 and 900 Da can be attributed to Nb compounds. It exhibits several peaks corresponding to high clusters of niobium oxides and hydroxides. The rapidly de-

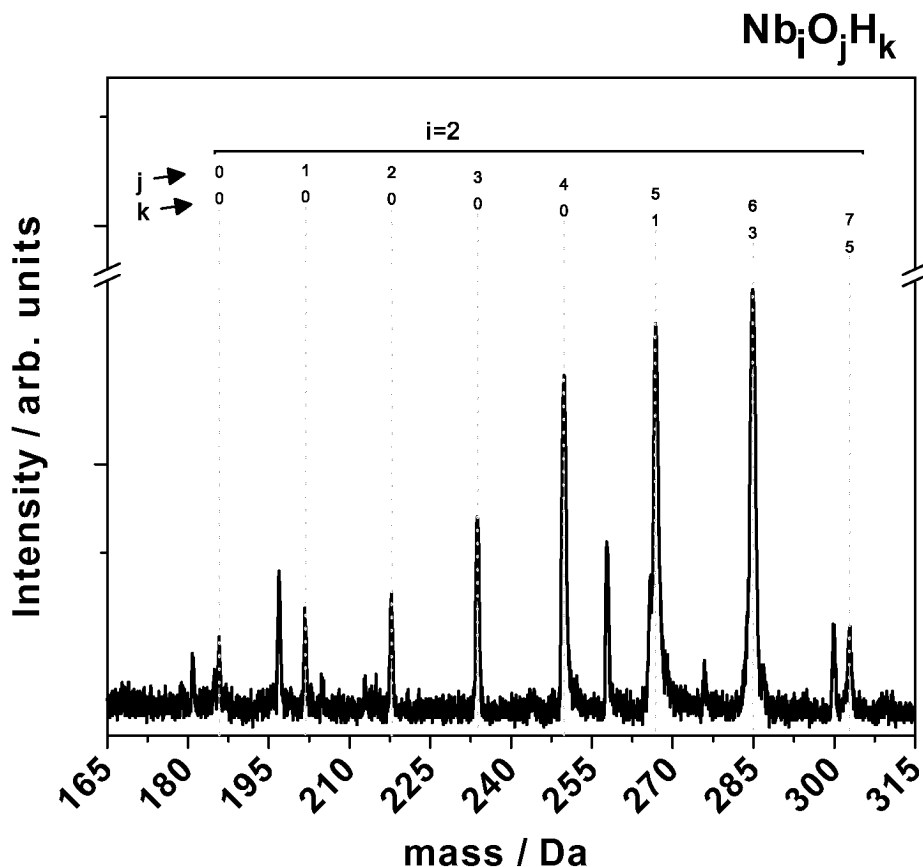


Figure 5.4: An enlarged view of the data presented in Fig. 5.3. The masses of niobium clusters containing two atoms of Nb are visible.

creasing peak intensity with increasing mass of clusters indicates, according to Athanassenas et al. [82], that the length of the nozzle "waiting room" is short. Bigger clusters of niobium could be formed when source nozzles were longer. However $\text{Nb}_i\text{O}_j\text{H}_k$ clusters in Fig. 5.3 were abundant when compared with the pure Nb peak, considering the difference of ionization energies. The nominal positions of the $\text{Nb}_i\text{O}_j\text{H}_k$ peaks corresponding to the assigned number of atoms $\{i,j,k\}$, are taken from NIST mass spectral database and represented as dashed vertical gray lines. Figures 5.4 and 5.5 contain identical experimental data as Fig. 5.3. The 165-315 Da and the 345-450 Da regions mainly show $\text{Nb}_2\text{O}_j\text{H}_k$ and $\text{Nb}_3\text{O}_j\text{H}_k$ clusters. The sequences of peaks in both mass domains exhibit similar characteristics: the intensity of Nb-oxide clusters exceed that of pure Nb clusters (start of the series and indicated only in Fig. 5.4). This behavior is enhanced when clusters involving some

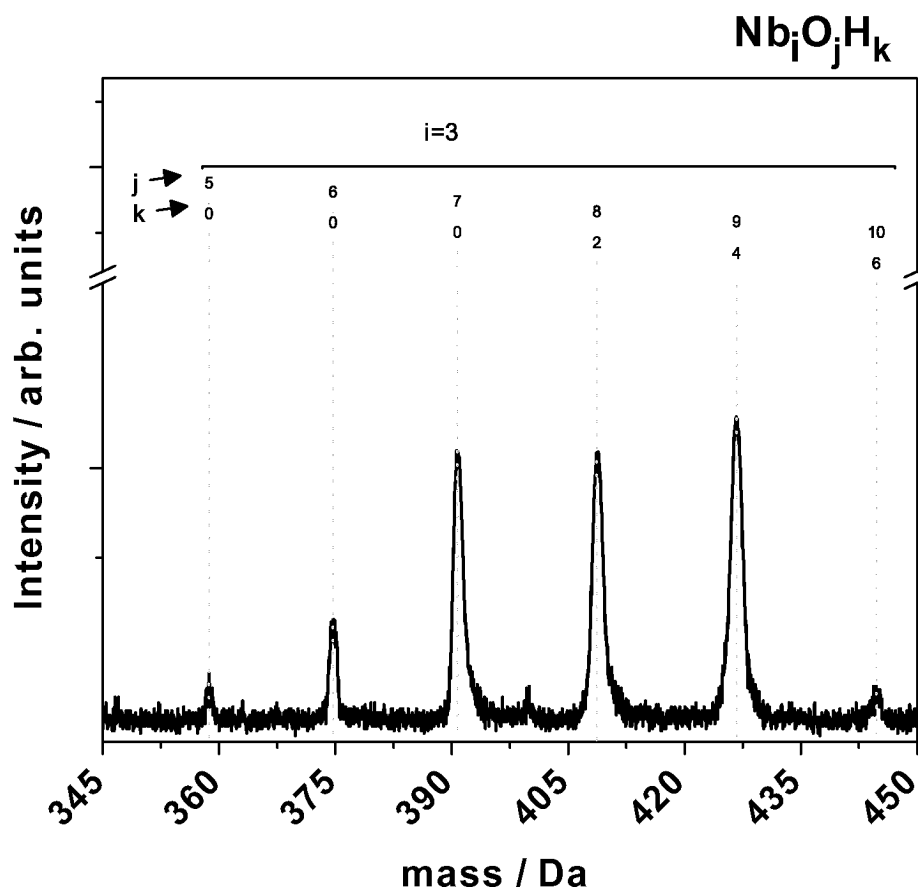


Figure 5.5: A detail of Fig. 5.3. Masses of niobium clusters with three atoms of Nb are shown.

hydrogen are formed. The peak corresponding to Nb_2O_5 , appears as a weak shoulder aside the more intense signal of $\text{Nb}_2\text{O}_5\text{H}$.

5.3 Production and observation of Zn compounds containing oxygen

To achieve optimal production of zinc compounds the following parameters were varied: pressure of background gas (Ne, Ar, He), the volume fraction of seed gas (H_2O , O_2 , N_2O), the nozzle configuration, and the timing of the ablation pulse with respect to the gas pulse. The temporal evolution of the gas pulse and its Zn doted portion were monitored by observing the mass spectrometric (MS) peaks of the carrier gas and Zn atoms while incrementing the delay between valve opening and the ionization pulse. Typically the MS signal due to zinc atoms exceeded all other signals above 64 Da as shown in Fig. 5.6. These spectra were taken with Ar as carrier gas containing an admixture of 1% (vol.) O_2 at a back pressure

of 5 bar. The large peaks of Zn (lower trace) appeared when the mass gate was disabled and detector sensitivity was reduced (MCP operating voltage: 2.0 kV). The upper trace, scaled up by a factor ten with respect to the ordinate, represents a spectrum obtained with the mass gate set to suppress masses < 70 Da. For this trace the sensitivity of the detector was increased by decreasing the MCP operating voltage to -2.6 kV (see Ion detectors in section 4.3.1). Apart from the expected time of flight, Zinc was easily identified by its typical isotope distribution (^{64}Zn : 48.5%, ^{66}Zn : 27.9%, ^{67}Zn : 4.1%, ^{68}Zn : 18.8%, ^{70}Zn : 0.7%). Best results were obtained with a 70° cone, 15 mm long nozzle, and the following timings: the ablation plume was initiated 0.7 ms after valve opening, i.e., at the time about which the carrier gas pulse reaches its maximum density at the locus where the plume emerges; the ionization laser was fired 1.26 ms after valve opening, shortly after the highest observed zinc density in the interaction region. The masses appearing at 81, 83, 84, 85 and 87 Da clearly show the signature of the Zn isotope distribution and can be assigned to zinc mono-hydroxide (ZnOH) with an accuracy better than 0.2 Da. In comparison to this relatively strong ZnOH signal, only low ZnO molecule concentrations have been observed in this experiment as shown in Fig. 5.7. Zinc oxide would yield peaks at 80, 82, 83, 84 and 86 Da. Weak peaks appearing at positions 80, 82 and the increase at 86 Da correspond to ^{64}ZnO , ^{66}ZnO , and ^{70}ZnO . The ZnO contributions from other zinc isotopes are buried under the ZnOH signals. The appearance of peaks attributable to ZnO depends delicately on the experimental conditions. Considering only ZnO and ZnOH contributions, a non linear least squares fit to the integral peaks between 80 and 87 Da yields that less than 10% of the signal originates from ZnO. The isotopic pattern is therefore not clear for peaks attributable to ZnO.

Conspicuously, the contribution at 86 Da in Fig. 5.7, is much larger in comparison with those at 80 Da and 82 Da, to be identified as $^{70}\text{Zn}^{16}\text{O}$. Combinations with ^{18}O hardly contribute to the observed variations, with the natural abundance of ^{18}O amounting to less than 0.25%. The interpretation of weak signals in this mass domain is somewhat difficult as contributions from hydrocarbon impurities are observable. The spectrum shown in Fig. 5.7 (lower trace) was registered without an ablation laser pulse, thus, without zinc vapour. Small peaks appear at all instances of ZnOH and that at 86 Da probably stemming from hydrocarbons and their fragments. However, no impurities are found at 80 Da and 82 Da. The corresponding peaks in a measurement with zinc vapour (upper trace and inlay of Fig. 5.7) could therefore, with some confidence, be attributed to ZnO. Taking into ac-

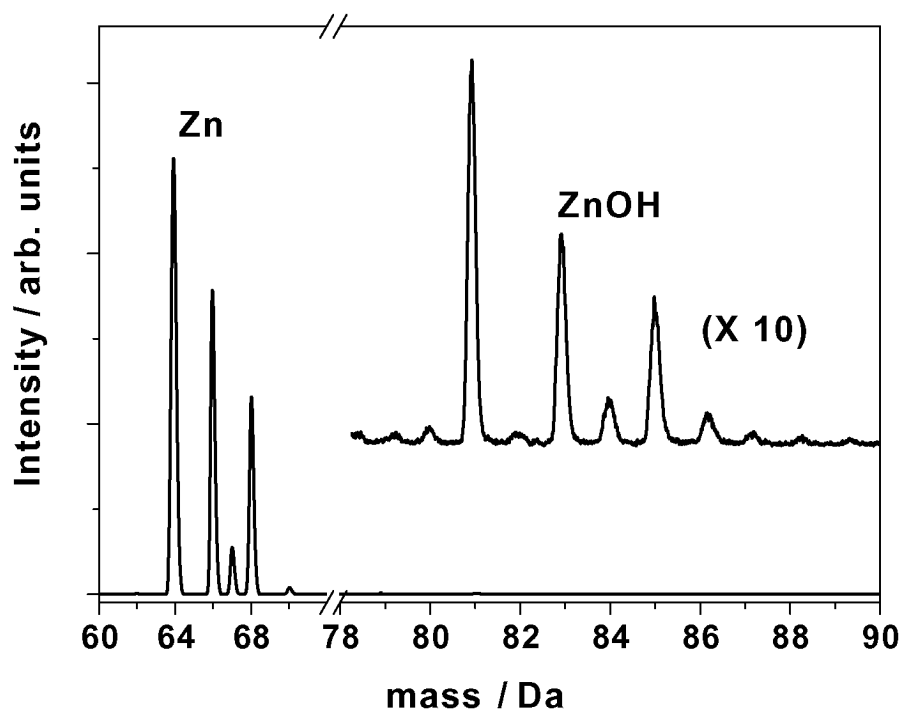


Figure 5.6: Mass spectrum with Zn vapour in Ar and 1% O₂. Back pressure is 5 bar. The intensity of the upper trace between 78 Da and 90 Da, is magnified 10 times for comparison.

count again the distribution of zinc-isotopes, the increase of signal at 86 Da is still too large compared to the peaks at 80 Da and 82 Da, rendering its interpretation as ZnO doubtful. Peaks at 93 Da and 94 Da could not yet be assigned. The sharpness of the observed peaks i.e. the temporal width of ~ 10 ns correspond to the temporal resolution of the Jordan ToF and suggests that the signals do not originate from fragments of larger masses dissociated during the ionization process. Fragmentation in the ionization step would produce masses carrying excess kinetic energy and result in broader peaks. The ion optics simulation of the Jordan ToF with our settings and the resolution of our ToF-measurement indicate that broadening effects would be observable for kinetic energies exceeding 0.2 eV. A maximum formation efficiency of zinc compounds was obtained with ablation pulse energies of ~ 5 mJ at a wavelength of 266 nm, corresponding to ~ 1.75 J/cm². The signals indicating the formation of ZnOH could also be produced with unseeded noble gases. Spurious water admixtures seem sufficient to produce ZnOH molecules and surprisingly, small water impurities produce much more ZnOH than ZnO in spite of the sizable admixture of O₂. Freezing out the water with a cold trap in the gas supply reduced the ZnOH signal to the noise level. Hence, the experiments so far do not allow a definite conclusion regarding the formation of ZnO from O₂ as precursor. The weakness of the ZnO signals could be explained by

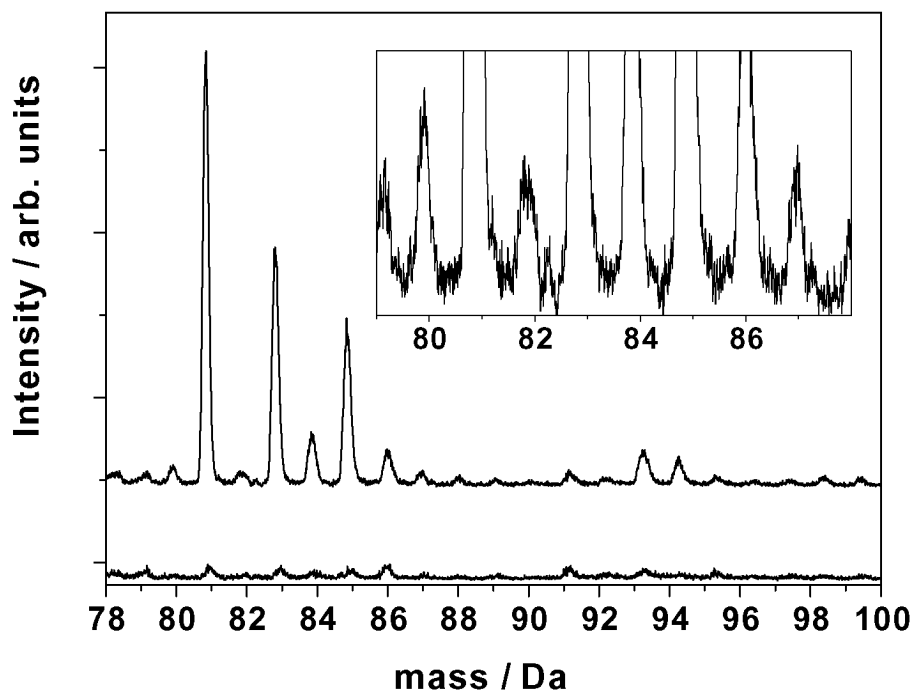


Figure 5.7: Mass spectrum obtained at the same conditions as in Figure 5.6 with (upper trace) and without (lower trace) laser ablated zinc plume. Peaks corresponding to ZnOH are evident with operating ablation source. The small peaks found at 80 and 82 Da might be related to ZnO (expanded inset).

either poor ZnO formation, less efficient ionization or ion fragmentation. If ZnO would be dissociated in the ionization step, the signals of Zn and O ions may be affected. However, with our experimental settings, small changes of the huge Zn peaks could not be quantified. Atomic oxygen yielded a weak and broad peak, possibly due to direct dissociation of O₂ in the ionization step, and was not quantifiable either.

Weak signals attributable to zinc compounds (Zn_xX_y, X = O, OH, N), could not be measured together with the overwhelming zinc ions signal close to the saturation level of the MCP detector. Zinc ions were therefore kicked off the ToF trajectory by a mass gate provided in the Jordon ToF. The mass gate is described in paragraph 4.3.1.

Avoiding water contamination in our system to get rid of the ZnOH we attempted to obtain a clear evidence for direct ZnO production from zinc vapour and an oxygen donor. Several gases ranging from pure (99%) O₂ and N₂O to their lean dilutions in He, Ne, Ar have been used for expansion of the zinc plume. Only with lean mixtures, a few percent of seed gas in noble gas, zinc compounds could be observed. Figure 5.8 shows the result obtained for 1% N₂O diluted in Ar. In Fig. 5.8, the peaks observable in the mass spectrum between 76 and 86 Da, are interpreted in terms of zinc combinations with nitrogen, carbon and hydrogen.

The histogram representing the best fit of the integrated peaks for varying concentrations of ZnC, ZnCH, ZnN, ZnNH, ZnO and ZnOH is shown together with the mass spectrum. Nitrogen is present in our experiment in the form of N₂O. In addition, the occurrence of hydrocarbons and water in our measurements indicates the presence of unwanted contaminations. Features of the mass spectrum in Fig. 5.8 were interpreted as contributions of several Zn containing species in combination, each with a given abundance. The best result in fitting the measurement corresponds to the following speciation: ZnC(12%), ZnCH(7%), ZnN(48%), ZnNH(12%), ZnO(22%) and ZnOH(0%). With N₂O as an oxygen donor, a clearly measurable yield of neutral ZnO can be observed, whereas with O₂, ZnO peak intensities hardly exceed noise levels. To avoid water contamination in our system and get rid of the ZnOH, we attempted to obtain a clear evidence for direct ZnO production from zinc vapour and an oxygen donor. The zero contribution of ZnOH indicates a successful

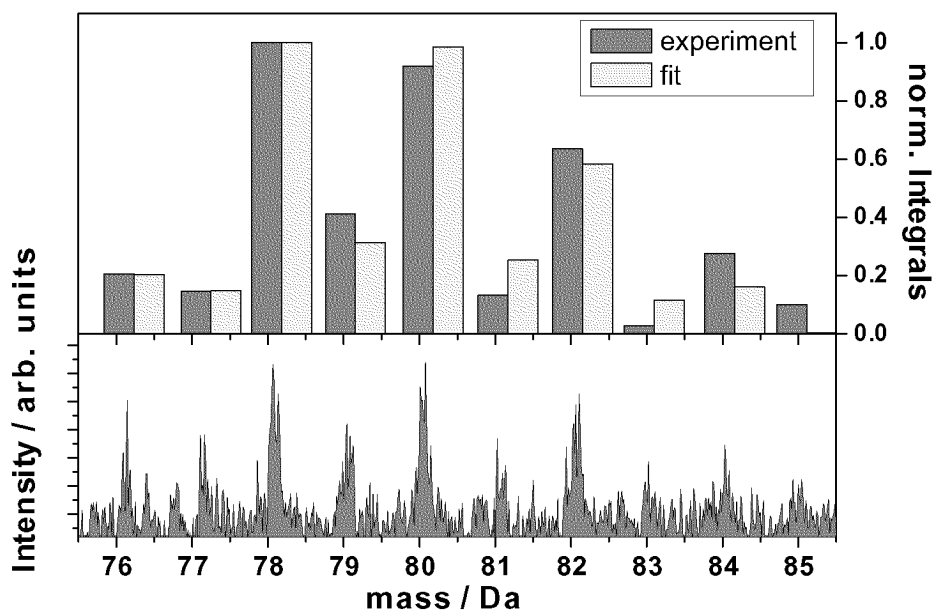


Figure 5.8: Mass spectrum of the molecular beam obtained by the expansion into vacuum of Ar and 1% N₂O, at 5 bar back pressure, seeded with Zn vapour. A histogram of the integrated measured peak intensities between 76 and 86 Da (dark grey) is shown above the spectrum. In the given mass interval the observed peak pattern could be determined by the simultaneous presence of ZnC, ZnCH, ZnN, ZnNH, ZnO and ZnOH in the molecular beam. The best fit of the histogram (light grey) determines for each molecules the relative abundances, respectively 12%, 7%, 48%, 12%, 22% and 0%.

suppression of water admixture in our experiment. The use of N₂O as an oxygen donor results in ZnN and ZnO production in parallel. Zinc carbide (ZnC) most probably results from residual hydrocarbon in the vacuum chamber, but contributes less than 10% to the mass spectrum.

5.4 Evidences of Zn_2X compounds ($X=O, OH, N$)

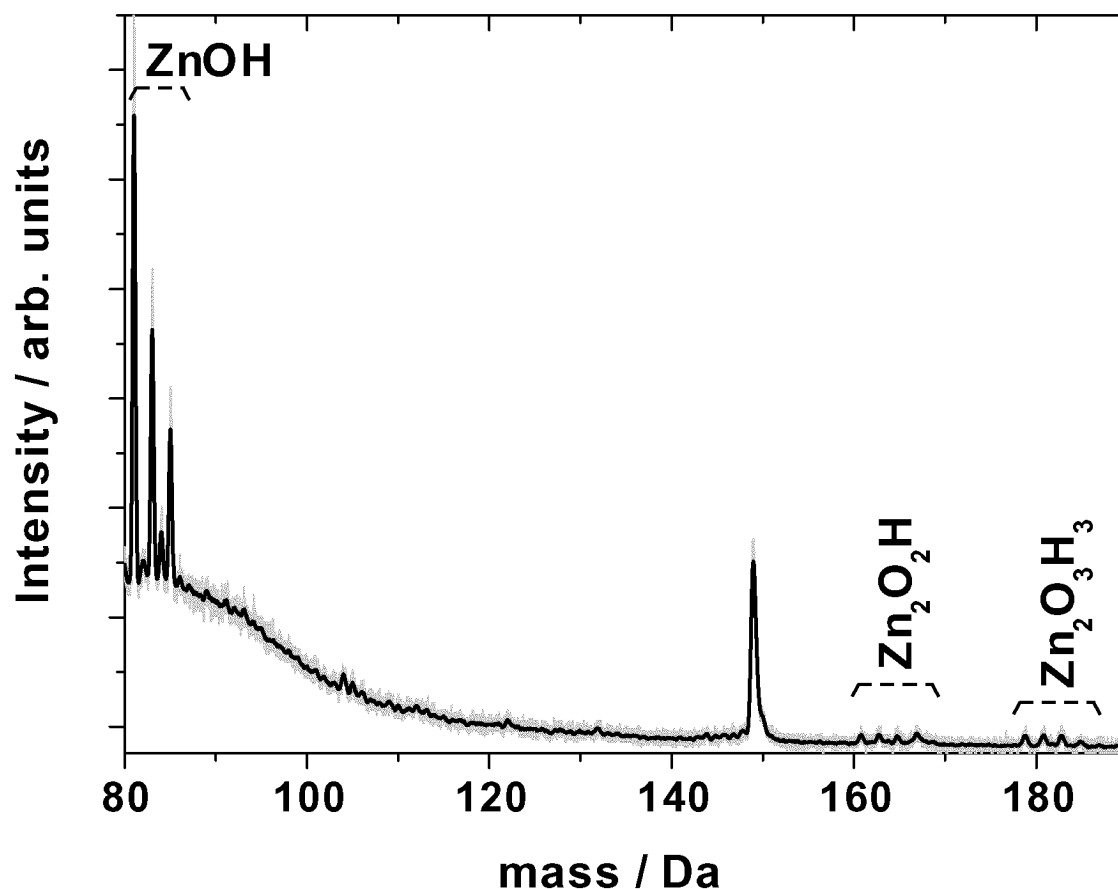


Figure 5.9: Mass spectrum (and smoothed trace) between 79 and 189 Da in Ne+1% O_2 at 5 bar(back pressure). The smoothed trace obtained by averaging 25 adjacent samples, is superimposed to the measured spectrum (gray). Peaks referred to ZnOH, $(ZnO)_2H$, and $Zn_2(OH)_3$ presence are marked accordingly.

In addition to ZnOH and ZnO we observed two stable dimeric compounds of zinc, $(ZnO)_2H$ and $Zn_2(OH)_3$ (Fig. 5.9). Though these signals are weaker than the one for ZnOH, the expected isotope distribution, shown as simulated MS-spectra in the upper halves of the Figures, is fairly well reproduced. Due to the absence of contributions from impurities, (hydrocarbons fragments do not show up in this mass range¹) the obtained signals are significant in spite of their low intensities (6 hours acquisition). However the signals are too weak to allow a clear interpretation of their peak width. Accordingly, it is not clear whether these compounds originate from a fragmentation of even larger Zinc compounds.

The mass spectrum measured between 159 and 190 Da using a 5 bar mixture of Ne with 1% O_2 is shown in Fig. 5.10. The smoothed trace (black), obtained by averaging 25 adjacent samples, is superimposed on the gray lined spectrum plotted at the bottom. The peaks

¹With the exception of a fragment at 167 Da.

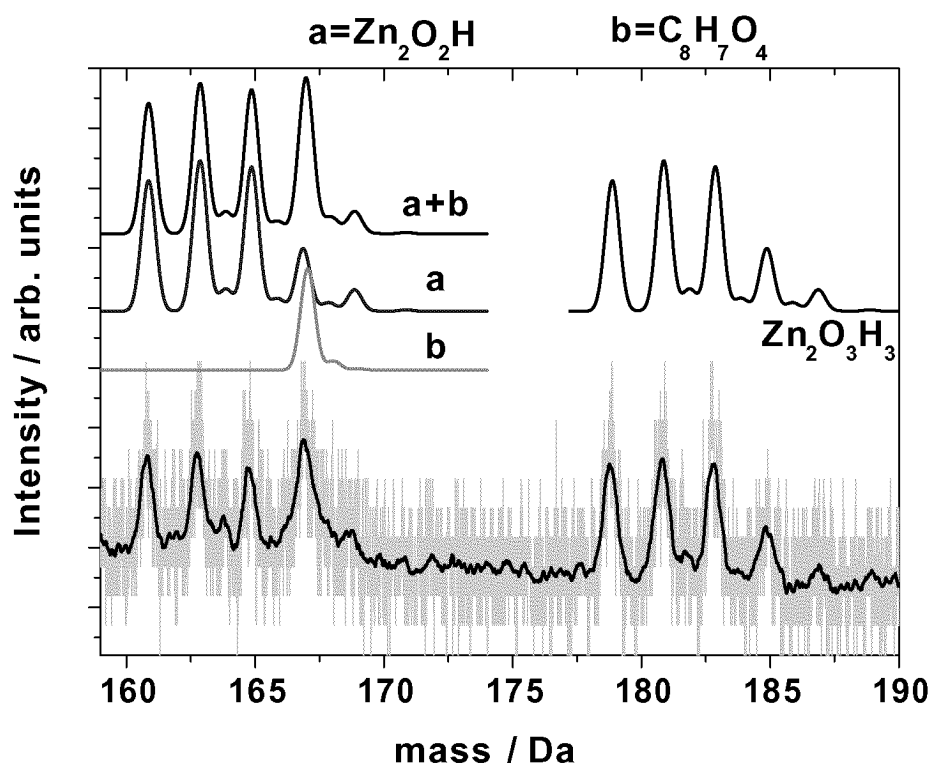


Figure 5.10: Mass spectrum (and smoothed trace) between 160 and 190 Da in Ne+1% O_2 at 5 bar(back pressure). Bottom: the smoothed trace obtained by averaging 25 adjacent samples is superimposed on the measured spectrum (gray). Top: the synthetic isotopic mass abundances of a contaminant, $(ZnO)_2H$ and $Zn_2(OH)_3$ are traced on two parallel lines one above the other. The sum of the traces is eventually plotted on a third line above the other two.

observed in this mass region could be attributed to $(ZnO)_2H$ and $Zn_2(OH)_3$.

In Fig. 5.11 and 5.12 two expanded views of the spectrum 5.10 in the intervals 159.5 Da to 171.5 Da and 176 Da to 190 Da are shown respectively. Immediately above the spectrum the synthetic spectrum considering the isotopic mass abundance of the $C_8H_7O_4$ (trace **b**), a fragment of the plasticizer $C_{24}H_{38}O_4$, is plotted in the mass interval from 159 to 174 Da, taking into account the resolution of our mass spectrometer. At the top, the synthetic mass spectra of $(ZnO)_2H$ and $Zn_2(OH)_3$, obtained by considering the zinc isotopic pattern, are plotted and identified by labels (trace **a**). Trace **c** gives the combination of the lower synthetic traces between 59 and 174 Da. Comparing the synthetic and acquired spectra in Fig. 5.11, the measured peak at 166 Da is found to be larger and higher than expected assuming $(ZnO)_2H$ to be the only chemical compound detected in the given mass range. The difference has to be attributed to additional chemical products which contribute to the spectrum, changing the natural isotopic intensity pattern of $(ZnO)_2H$ otherwise expected.

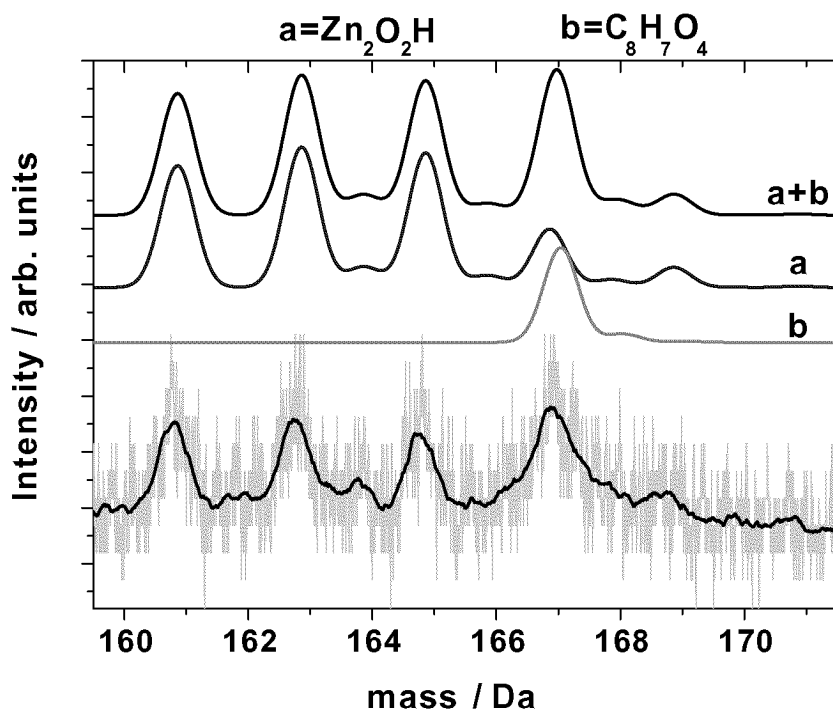


Figure 5.11: Mass spectrum (and smoothed trace) between 160 and 170 Da with Zn vapour in Ne and 1% O_2 at a back pressure of 5 bar. The peaks can be attributed to $(\text{ZnO})_2\text{H}$. The upper trace shows a synthetic mass spectrum of $(\text{ZnO})_2\text{H}$ taking into account the isotopic pattern of zinc and the resolution of our Re-ToF MS.

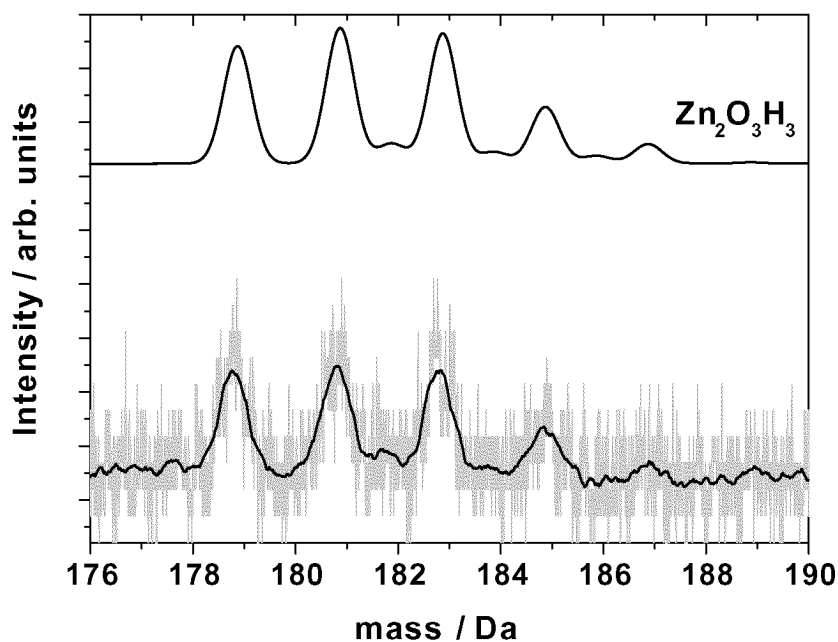


Figure 5.12: Mass spectrum (and smoothed trace) between 178 and 188 Da with Zn vapour in Ne and 1% O_2 at a back pressure of 5 bar. The peaks can be attributed to $\text{Zn}_2(\text{OH})_3$. The upper trace shows the corresponding synthetic mass spectrum of $\text{Zn}_2(\text{OH})_3$ reflecting the isotopic pattern of zinc.

5.5 Summary of experiments

We have shown, that neutral ZnO, ZnOH, ZnC, ZnN, ZnOH-ZnO and ZnOH-ZnO-H₂O compounds can be observed in a molecular beam derived from a laser ablated plasma of zinc reacting with gas mixtures containing H₂O, O₂ or N₂O. The yield for most of the mentioned species with the exception of ZnOH is rather poor and Zn_xO_y clusters were not observed in our experiments so far. The precursor for the production of ZnOH could clearly be identified to be water. Without water, a clear evidence of neutral ZnO formation is obtained with N₂O seed gas. In this case ZnN appears together with ZnO. The production yield is much less for both species compared to ZnOH production from small water impurities. No clear traces of neutral ZnO compounds were evident in the spectra collected when a ZnO solid target was ablated by the 266 output beam of the DCR-2A laser. In these measurements, we could not identify any combination of experimental parameters which enhanced the Zn and oxygen reaction yielding ZnO compounds in the molecular beam. Furthermore, the addition of oxygen containing molecules to argon did not result in significant changes either.

In order to prove that the difficulties in the production of neutral ZnO molecules in the gas phase were not dependent on the functionality of our molecular beam setup, we performed experiments with Niobium. Under conditions similar to those used for the experiments with zinc, Niobium readily produced all types of clusters. In these experiments, the strongest dimeric Nb compounds besides the oxygenated Nb₂O_{1...5} complexes were Nb₂O₅H and Nb₂O₅H•H₂O when small water impurities were present.

Chapter 6

Discussion and Outlook

The results of the experiments presented in the last chapter indicate that ZnOH and ZnO can be produced in a molecular beam. We could identify, without ambiguity, traces of ZnOH and ZnO when expanding ablated zinc together with 1% N₂O. To our knowledge this is the first direct evidence of neutral diatomic zinc oxide and zinc hydroxide in the gas phase [15, 83, 84, 85]. Hydrogen, for the formation of ZnOH, is donated by water present in first experiments as contaminant in our set-up. Subsequent experiments in which water was deliberately added or water contamination was avoided indicated clearly that water indeed is the H donor.

In our test measurements we could observe oxides of niobium as well as Nb_n clusters. This confirmed our experimental set up to be suited to metal oxidation, cluster aggregation and detection in a broad mass interval ranging from 1 to 800 Da. However, traces of Zn compounds were much weaker in intensity and their formation was critically dependent on the experimental conditions, such as the intensity and wavelength of the ablation laser, the concentration and type of oxygen donor seeded in the noble gas, and pressures values.

Previous studies on metal ablation plumes at laser powers of $\sim 10^7 - 10^{10}$ W/cm² have shown that neutral metal atoms can acquire a kinetic energy of about 10 eV. Kinetic energy ten times greater can be observed with ions. A high amount of cations and anions in the plume region could give rise to ion-ion recombination reactions, such as e.g. $\text{Zn}^+ + \text{O}^- + \text{M} \rightarrow \text{ZnO} + \text{M}$, that might contribute or even dominate the ZnO production via neutral channels.

The details of the laser induced surface breakdown are very complex and dedicated experiments will have to be conceived for the determination of the actual formation path. The production of zinc compounds is found to be rather inefficient in accordance with earlier

attempts [20]. Laser ablated Zn atoms must provide a sufficient amount of excess energy (kinetic and/or electronic) to enter the strongly endothermic reaction with oxygen to form ZnO. Consequently, the augmentation of thermal energy in the plasma plume was expected to yield more ZnO. With ablation laser pulse energies above 5 mJ/pulse no further increase of ZnO or ZnOH production could be observed in our system. Improvement of the ZnO formation was however achieved upon changing the ablation laser wavelength from 532 to 266 nm.

A much more efficient reaction is expected with electronically excited Zn than with Zn in its electronic ground state [86]. Photo excitation from the 4^1S_0 ground state to the metastable $3P_J$ states occurs at wavelength > 308 nm, indicating that the plasma generation exhibits a wavelength dependency and further, thermal material properties play a role. Due to the difficulties in the production of neutral ZnO molecules in the gas phase we performed experiments with Niobium to prove the functionality of our molecular beam setup. Under similar conditions Niobium readily produced all types of clusters. In these experiments, the strongest dimeric Nb compounds besides the oxygenated $Nb_2O_{1...5}$ complexes were Nb_2O_5H and $Nb_2O_5H \bullet H_2O$ when small water impurities were present. There is no straightforward explanation why Zn hardly produces neutral compounds or clusters other than ZnOH, Zn_2O_2H and $Zn_2O_2H \bullet H_2O$. The absence of small pure zinc metal clusters that are only weakly bonded (e.g. ~ 0.02 eV for Zn_2) [87] can be explained by the fact that we did not in most likelihood, reach ultra cold molecular beams.

These results might suggest that hydrogen plays a role and enhanced in preceding cluster formation of Zinc with oxygen.

The growth mechanism of ZnO-crystals, -nanostructures and -semiconductors are not fully understood and hydrogen impurities, which are difficult to avoid are expected to play a major role [6]. It has been argued that one of the agents for ZnO agglomeration is H_2O [88]. The question whether the agglomeration occurs via ZnOH or $Zn(OH)_2$ is not yet answered. In our experiments we did not detect any $Zn(OH)_2$, though ZnOH appeared. Studying the reaction of metal atoms and dimers in the presence of water, Kauffmann et al. [83] found that condensation of zinc atoms together with H_2O exclusively yield ZnOH in an Ar matrix upon photolysis in the region of 200-300 nm. The dominance of ZnOH in the detected mass spectra, even though water impurities were small, indicates that ZnOH should be considered in the context of heavier ZnO clusters and nano structures.

Appendix A

ToF-MS, reflectron and SIMION

In this appendix we derive the relations between detection time and ion masses that apply to time of flight mass spectrometers with single and double acceleration stages, with and without a ion reflectron. The equations derived are not new as they were already obtained before [66, 70, 89].

A.1 Linear ToF-MS system

A conventional linear ToF mass spectrometer consists of accelerating sections followed by a field free space, called drift region, where ions fly toward a detector with constant velocities. The resulting ion speeds are originated by the acceleration produced in each of these sections by uniform electric fields. The first section, where the physical extraction of ions take place, consists of two electrodes and it is commonly indicated as 'extraction' region. The electrode, called repeller, repels the ions away towards the other electrode, which let them continue their flight trough an extraction grid. The most basic ToF-MS system comprises one single electric field which propels ions along the axis of symmetry of the complete system as shown in Fig. A.1. In such a system the terminal velocity v_f is given by

$$v_f = \left(v_0^2 + 2 \frac{q}{m} E \times d_0 \right)^{\frac{1}{2}} = \left(v_0^2 + 2 \frac{q}{m} (V_1 - V_2) \times \frac{d_0}{d} \right)^{\frac{1}{2}} \quad (\text{A.1})$$

$\stackrel{def}{=} (v_0^2 + v_{f,v_0=0}^2)^{\frac{1}{2}}$

where m is the ion mass, q is the ion charge, v_0 is the initial on axis velocity component, d and d_0 are the length of the acceleration section and the initial position referred to the extraction grid along the symmetry axis respectively, E is the electric field with V_i the

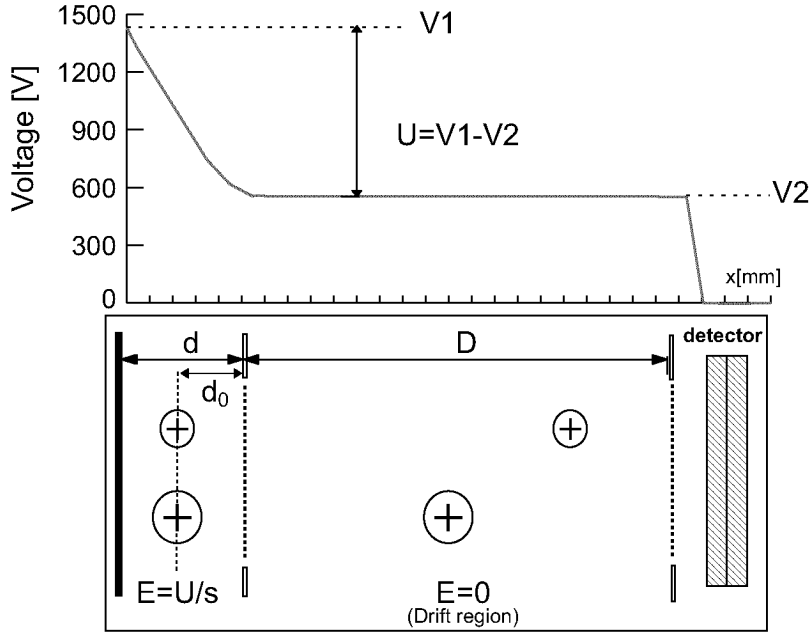


Figure A.1: Schematic representation of a ToF-MS working principle: the arrival time to the detector of heavy ions (size indicated) is shorter than that of lighter ones and the difference increase linearly with the drift region length. Above, a chart illustrates a typical potential field along the spectrometer.

corresponding potential applied between the extraction grid ($i = 1$) and the repeller ($i = 2$).

The time of flight (T) of the ion can be computed using the following equation:

$$T = \frac{m}{q} \left(\frac{v_f - v_0}{E} \right) + \frac{D}{v_f} \quad (\text{A.2})$$

where D is the length of the drift region.

Neglecting v_0 with respect to the speed due to the electric field, namely if $v_0 \ll v_f, v_0=0$ in eq. A.1, we can write

$$T = \left(\frac{m}{q} \right)^{\frac{1}{2}} \left(\frac{1}{2E \times d_0} \right)^{\frac{1}{2}} (2d_0 + D) \quad (\text{A.3})$$

Equation A.3 prescribes a time of flight which is proportional to the square root of the ion mass. This represents a general relation for all ToF spectrometers, regardless the complexity of their designs. We require the first order space focus condition to have negligible variations of ToF for small changes of the starting positions around \bar{d}_0 :

$$\left. \frac{\partial T}{\partial d_0} \right|_{\bar{d}_0} = 0 \quad (\text{A.4})$$

This condition corresponds to the following constraint in the ToF geometry of the simple system in exam:

$$D = 2\bar{d}_0 \quad (\text{A.5})$$

which is a severe limitation for the achievable resolution. Moreover, higher order focus conditions ($\left. \frac{\partial^k T}{\partial d_0^k} \right|_{d_0} = 0$, with $k = 2, 3, \dots$) are impossible to be satisfied all at once in the simple system under investigation. More acceleration sections (> 1) are required in the ToF-MS design to be able to achieve, even at higher orders, a space focus condition that fits the geometry requirements.

A.2 Two-Field ToF Mass Spectrometer

Figure A.2 shows a commonly used two-Field ToF system. We can derive the following equations:

$$v_f = \left(v_0^2 + 2\frac{q}{m}E_1 \times d_0 + 2\frac{q}{m}E_2 \times d_2 \right)^{\frac{1}{2}} \quad (\text{A.6})$$

$$T = \frac{m}{q} \left(\frac{v_1 - v_0}{E_1} \right) + \frac{m}{q} \left(\frac{v_f - v_1}{E_2} \right) + \frac{D}{v_f}$$

where d_i , E_i and v_i are the length, the uniform field and the exit velocity of the i^{th} acceleration region, respectively.

We can set $v_0 = 0$ in eq. A.6 and derive the time of flight:

$$T = \left(\frac{m}{q} \right)^{\frac{1}{2}} \left(\frac{1}{2E_1 \times d_0 + E_2 \times d_2} \right)^{\frac{1}{2}} \left(2k_0^{\frac{1}{2}}d_0 + 2\frac{k_0^{\frac{1}{2}}}{k_0^{\frac{1}{2}} + 1}d_2 + D \right) \quad (\text{A.7})$$

with $k_0 - 1 = (E_2 \times d_2) / (E_1 \times d_0)$. Equation A.7 can be represented in terms of potentials

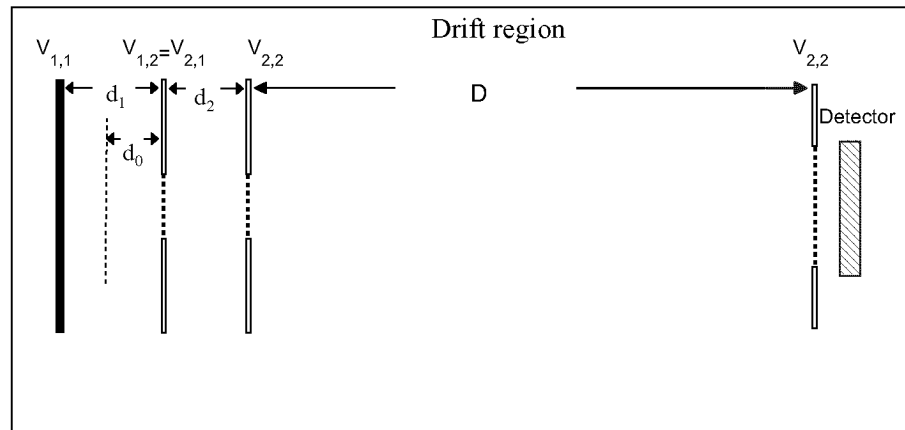


Figure A.2: Sketch of a two stages time of flight mass spectrometer. The distances between the electrodes in the extraction and acceleration stages are marked as d_1 and d_2 ; as for the linear ToF, d_0 and D indicate the depth of ions produced in the first stage and the drift tube length respectively. The electrode potentials are also designated.

$V_{k,2} - V_{k,1} = E_k \times d_k$	Potential drop across the acceleration region k
$V_{1,0} = V_{1,1} + (V_{1,2} - V_{1,1}) \frac{d_0}{d_1}$	Potential at initial ion position
$V_{k,1} = V_{k+1,2}$	Continuity

Table A.1: The potentials $V_{k,i}$ corresponding to the mass spectrometer electrodes are identified by the two indexes k, j . The first is associated to the order of the acceleration stage to which the electrode belong, while the second specifies the electrode's rank in the stage.

$V_{k,i}$, k being the acceleration region number, as

$$T = \left(\frac{m}{q}\right)^{\frac{1}{2}} \left(\frac{1}{2} \frac{1}{V_{1,0} - V_{2,1}}\right)^{\frac{1}{2}} \left(2k_0^{\frac{1}{2}} d_0 + 2 \frac{k_0^{\frac{1}{2}}}{k_0^{\frac{1}{2}} + 1} d_2 + D\right) \quad (\text{A.8})$$

where $k_0 = \left(1 - \frac{V_{2,1}}{V_{1,0}}\right) / \left(1 - \frac{V_{1,1}}{V_{1,0}}\right)$. In order to obtain eq. A.8 we used the relations summarized in Table A.1. The first order space focus condition is achieved, for $V_{2,2} = 0 V$, by imposing

$$\frac{V_{1,1}}{V_{1,2}} = 1 + \frac{1}{1 + \frac{d_0}{d_1} (y^2 - 1)} \quad (\text{A.9})$$

with y positive and real root of the 3^{rd} order polynomial $P(y) = y^3 - \frac{d_1}{2d_0} y^2 - \frac{D}{2d_0} y - \frac{D}{2d_0}$

A.3 Two-field ToF-MS with a two-stage Reflectron

In this paragraph we present an expression for T derived for the two-field ToF mass spectrometer with a one stage reflector, showed in Fig. A.3, under the severe assumptions of ideal electric fields, without boundary distortions. In the following paragraphs a comparison with a numerical approach will be presented. Referring to the nomenclature summarized in Fig. A.3 for the time of flight, we can write:

$$T = \left(\frac{m}{2U_i}\right)^{\frac{1}{2}} \left[(D_1 + D_2) + 2k_0^{\frac{1}{2}} \left(d_0 + \frac{d_2}{k_0^{\frac{1}{2}} + 1}\right) + 4k_r^{\frac{1}{2}} \left(r_0 + \frac{d_g}{k_r^{\frac{1}{2}} + 1}\right) \right] \quad (\text{A.10})$$

first and second derivatives of T are given by:

$$\begin{aligned} \frac{\partial T}{\partial d_0} = & - \left(\frac{m}{2U_t} \right)^{\frac{1}{2}} \frac{1}{2d_0 k_0} \left[(D_1 + D_2) - 2k_0 \left(k_0^{\frac{1}{2}} d_0 - \frac{d_2}{k_0^{\frac{1}{2}} + 1} \right) + \right. \\ & \left. + 4k_r \left(k_r^{\frac{1}{2}} r_0 + \frac{d_g}{k_r^{\frac{1}{2}} + 1} \right) - 8 \frac{U_t}{q (V_{r2} - V_{r1})} k_r^{\frac{1}{2}} \Delta r \right] \end{aligned} \quad (\text{A.16})$$

$$\begin{aligned} \frac{\partial^2 T}{\partial d_0^2} = & \left(\frac{m}{2U_t} \right)^{\frac{1}{2}} \frac{3}{4d_0^2 k_0^2} \left[(D_1 + D_2) - \frac{2}{3} k_0 \left(k_0^{\frac{3}{2}} d_0 - k_0^{\frac{1}{2}} d_2 - \frac{d_2}{k_0^{\frac{1}{2}} + 1} \right) + \right. \\ & \left. + \frac{4}{3} k_r \left(3k_r^{\frac{3}{2}} r_0 + k_r^{\frac{1}{2}} d_g + \frac{d_g}{k_r^{\frac{1}{2}} + 1} \right) - \frac{16}{3} \frac{U_t}{q (V_{r2} - V_{r1})} k_r^{\frac{3}{2}} \Delta r \right] \end{aligned} \quad (\text{A.17})$$

We can deduce an expression for the transversal displacement during the time of flight T :

$$\begin{aligned} \Delta y_{tot} = & V_{0y} T + \left(\frac{q}{m} \right) \left(\frac{m}{2U_t} \right)^{\frac{1}{2}} (V_{xy2} - V_{xy1}) \left(\frac{\Delta x}{\Delta y} \right) \times \\ & \left((T - T_2) - \left(\frac{m}{2U_t} \right)^{\frac{1}{2}} \right) \left(\delta + \frac{\Delta x}{2} \right) \end{aligned} \quad (\text{A.18})$$

where $T_2 = \left(\frac{m}{2U_t} \right)^{\frac{1}{2}} 2k_0^{\frac{1}{2}} \left(d_0 + \frac{d_2}{k_0^{\frac{1}{2}} + 1} \right)$ is a time of flight contribution due to the acceleration stages.

A.4 Ion time of flight vs v_{0x} and d_0 : an analytic expression

In the previous paragraphs we have derived all the formulas for the time of flight under the hypothesis of no initial ion kinetic energy along the axis of symmetry of the mass spectrometer. The properties of the uniform electric field acting in the region where ions are produced, allow us to write new equations which take into account the ions speed component at the starting time. It can be shown that an ion generated at time $t = 0$ in a position d_0 referred to the extraction grid, with velocity component v_{0x} , is equivalent to an ion formed at rest in $d_0 + \Delta d$ at a time given by δT . As a consequence, the following more general expression holds for the time of flight:

$$T(v_{0x}, d_0) = T_0(d_0 + \Delta d) - \delta T \quad (\text{A.19})$$

where T_0 is the time computed in the previous paragraphs with eq. A.10 or eq. A.8.

Figure A.4 graphically shows how Δd and the absolute value of δT , are defined. Δd is the space and δT is the time required to the ion with initial speed $-abs(v_{0x})$ to reach null

velocity moving in the uniform field. The following equations can be obtained for them:

$$\begin{cases} \Delta d = \left(\frac{m}{2q}\right) v_{0x}^2 \frac{d_1}{(V_{a1} - V_{a2})} \\ \delta T = \left(\frac{m}{q}\right) v_{0x} \frac{d_1}{(V_{a1} - V_{a2})} \end{cases} \quad (\text{A.20})$$

where the sign of δT is the same of the initial velocity component, in agreement with the following observations. If $v_{0x} > 0$, the ion, generated at rest at position $d_0 + \Delta d$, reaches a position d_0 with velocity component v_{0x} in a time interval δT . Therefore, the time of flight is given by the eq. A.19. Otherwise, if $v_{0x} < 0$, the ion, which starts at time $t = 0$ in position d_0 , moves to $d_0 + \Delta d$, where finally it reverses its direction after a time $abs(\delta T)$. The ion thus returns back to the generation plane with opposite speed component, after double the given time interval, namely $t_{turn} = 2 \times abs(\delta T)$ ¹. The resulting time of flight is then given as sum of the the time computed with the eq. A.19 for $v_{0x} > 0$ and t_{turn} . Equation A.19 correctly describes the ion ToF in this case, as shown by algebraically rearranging this sum.

The above derivation will help us to better characterize the Re-ToF vs ToF. If we use as start position the expression in eq. A.15, which accounts for the ion initial speed , we obtain:

$$r_0 = r_0|_{v_{0x}=0} + \frac{\left(\frac{1}{2}mv_{0x}^2\right)}{q(V_{r2} - V_{r1})} \Delta r \quad (\text{A.21})$$

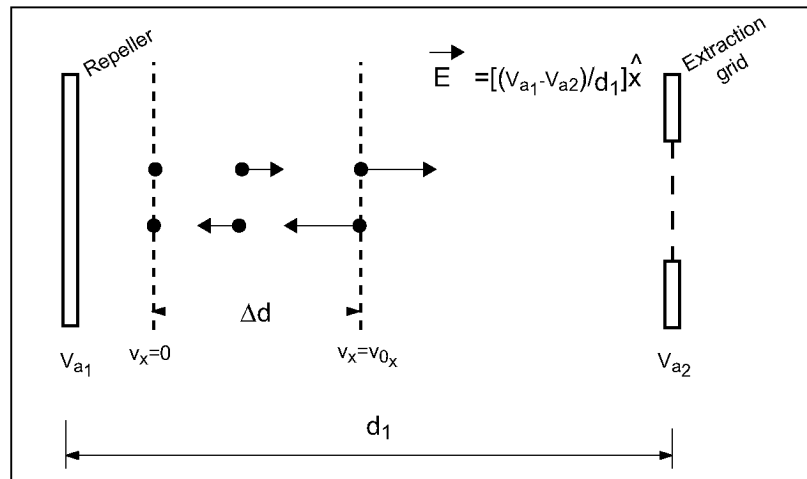


Figure A.4: Schematic drawing which illustrates the relation between the initial ion velocity and the parameters defined in eq. A.20.

¹It corresponds to the maximal ToF difference between ions with same parameters and opposite velocity components along the MS axis.

Ions with higher initial kinetic energies (in the MS axis) go deeper in the reflectron and the relation between penetration depth and the kinetic energy is linear. Moreover, the greater is the potential drop along the reflectron the smaller will be the displacement from the depth without kinetic energy. The percent change ratio is:

$$\frac{r_0 - r_0|_{v_{0x}=0}}{r_0|_{v_{0x}=0}} = \frac{\frac{1}{2}mv_{0x}^2}{q(V_0 - V_{r1})} \quad (\text{A.22})$$

that for typical potential values and initial kinetic energies lies usually in the range between 0.01% and 0.2%. Now we consider the difference between the times of flight of the same ion with and without initial kinetic energy for a Re-ToF mass spectrometer and a two stages ToF-MS. To compare the two results we require for both spectrometers the first derivative with respect to d_0 to be null and we arbitrarily set V_{a2} to a specific value. In this way we determine all voltages to be applied at the acceleration stages of Re-ToF and linear ToF-MS. Still the Re-ToF requires an additional condition to set the reflectron potentials. A frequently used condition is that the depth reached by the ion (with no initial kinetic energy) in the reflectron is 85% of its total length. In this way we guarantee that the contribution of eventual boundary effects (in the actual text not considered) is minimal and negligible. Figure A.5 shows the result computed for a ToF and for a Re-ToF having considered for the latter the potentials reported in the mass spectrometer user's manual.

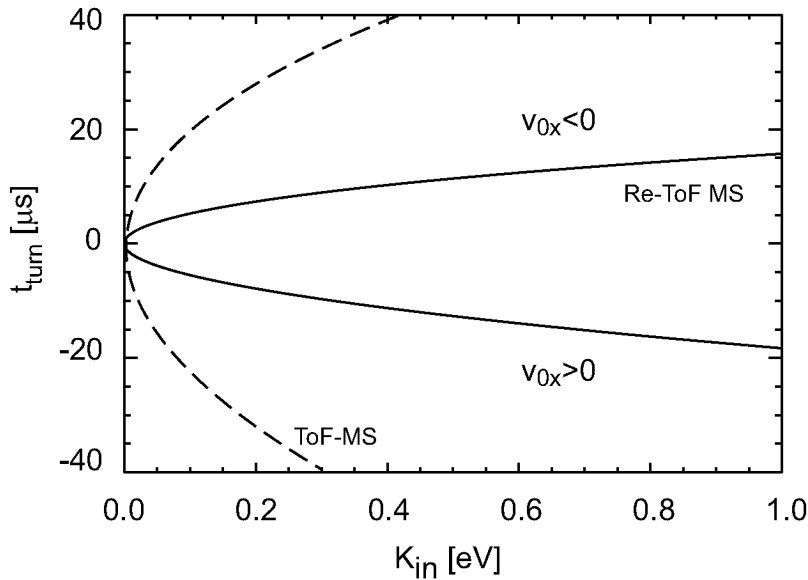


Figure A.5: Comparison of the kinetic energy dispersion attenuations with and without reflectron

A.5 Set of potentials for a second order spatial focus condition

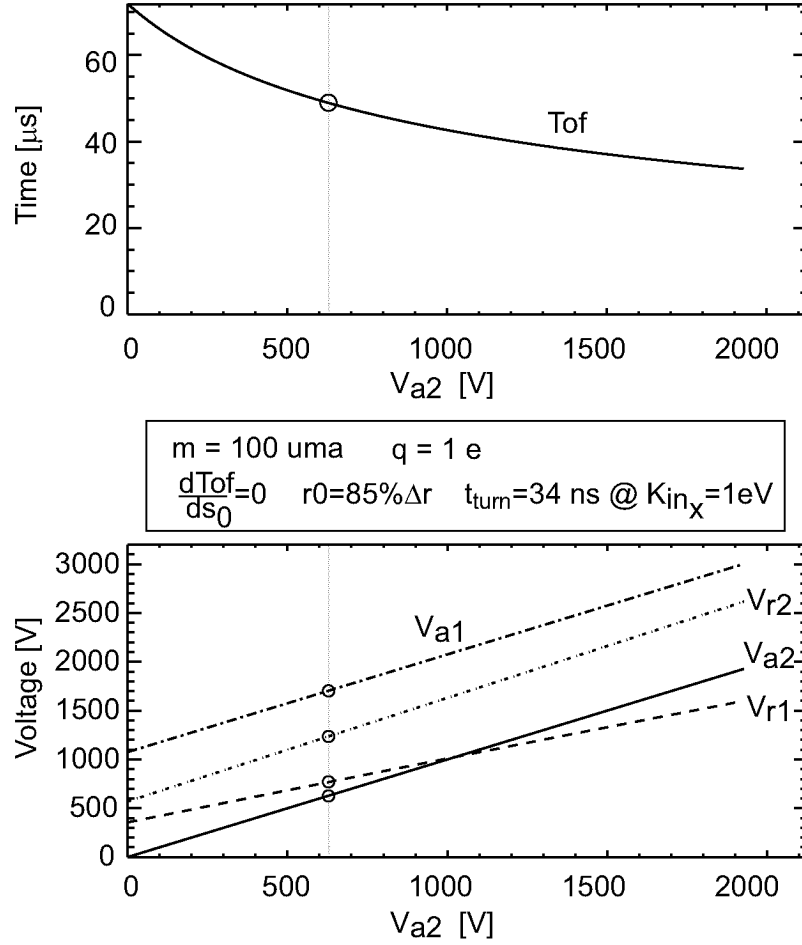


Figure A.6: Set of potentials along the Re-ToF versus its voltage at the extraction grid, obtained by imposing the condition listed in the box. The circles are used to show the set of potentials suggested by the user manual to start operation, optimized for 100 Da . The time of flight is plotted to observe that as long as we move to lower potentials the spatial resolution is expected to improve.

In this section we describe how the sets of potentials, to be applied on our Jordan Re-ToF mass spectrometer, were chosen. The goal was to select potentials that represented all together a solution for both the equations:

$$\frac{\partial T}{\partial d_0} = 0 \quad ; \quad \frac{\partial^2 T}{\partial d_0^2} = 0 \quad (\text{A.23})$$

where the spatial derivative of first and second order are related to the geometrical parameters of our spectrometer through the equations A.16 and A.17.

Thus, to identify the “proper” set of potentials, a non linear system of equation has to be solved numerically. I developed a software program to compute a solution A code through

the steps summarised in Fig. A.8. In order to simplify the problem I imposed the conditions:

$$\begin{cases} t_{turn}^{1\text{eV}} = (2m/q) v_{0x} \frac{d_1}{(V_{a1} - V_{a2})} = \text{constant} \\ \text{ratio} \stackrel{\text{def}}{=} \frac{r_0}{\Delta r} = \text{constant} \\ Vg = 0 \text{ V} \end{cases} \quad (\text{A.24})$$

where $t_{turn}^{1\text{eV}}$, together with the inversion time, δT , introduced in the previous section, is computed for an initial kinetic energy $K_{in} = 1 \text{ eV}$; the ratio specifies, in terms of Δr , the maximum depth (r_0) reached by the ion while flying through the reflectron.

With these assumptions the number of independent potentials could be reduced to two

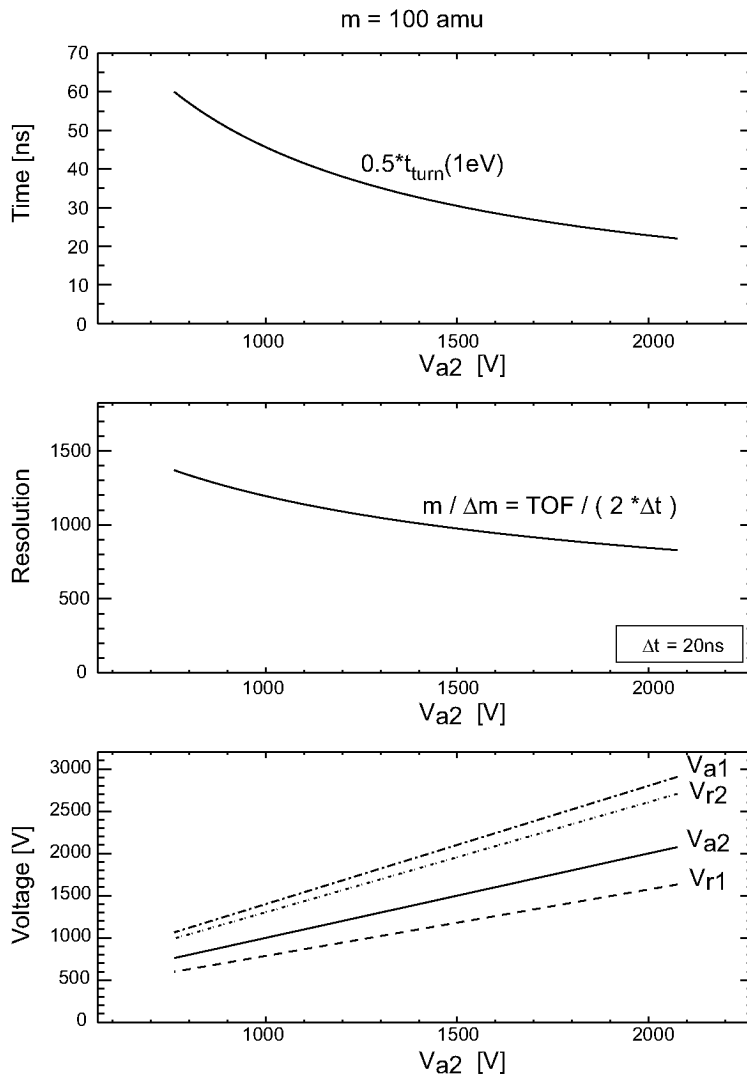


Figure A.7: The set of potentials which are solution for the eq. A.5 for a cation of mass 100 Da are plotted in function of the potential at the extraction grid. ToF and t_{turn} are also shown. The corresponding values of $t_{turn}^{1\text{eV}}$ and of the spatial resolution are also shown. At higher potentials we expect a gain of spatial resolution and a contemporary increase of the time dispersion due to initial kinetic energy.

using equations A.15 and A.4. The code searches the values of this pair of potentials that contemporary satisfy equations A.5.

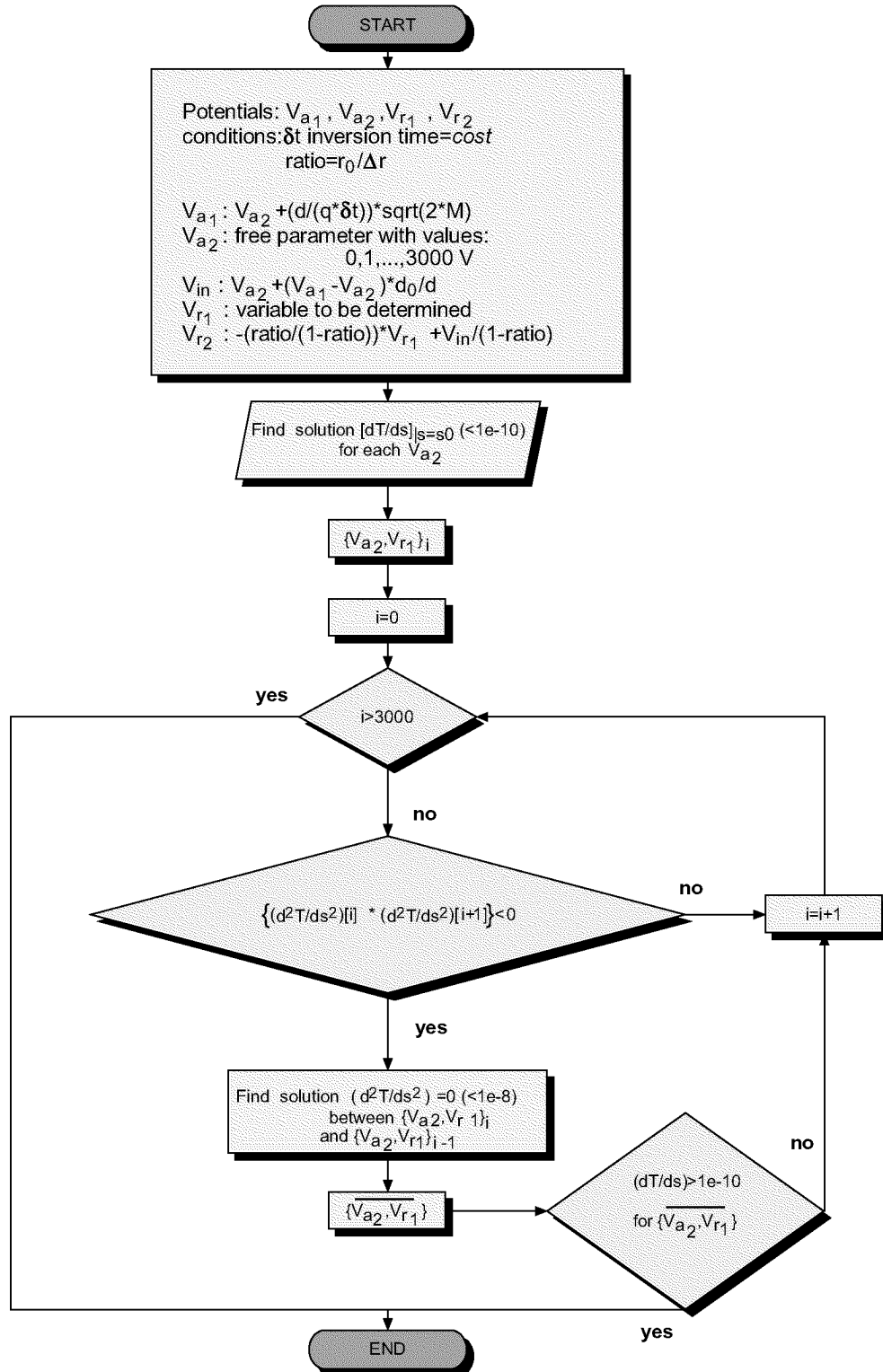


Figure A.8: Data flow diagram of the program we implemented. The main steps for computing the voltage values to be assigned to the electrodes of the Jordan Re-ToF mass spectrometer, maximizing the resolution, are indicated.

A.6 Two points calibration and mass correction

After calibration if masses corresponding to peaks are found to be incorrectly assigned, it can be necessary to carry out a mass correction. It consists of a transformation between masses obtained using two different calibrations. The transformation from the masses in the old calibration to those in the new one is described by the following equation:

$${}^*m = \left(\frac{{}^*\overline{m}_2^{1/2} - {}^*\overline{m}_1^{1/2}}{\overline{m}_2^{1/2} - \overline{m}_1^{1/2}} \right)^2 \left[m^{1/2} - \overline{m}_1^{1/2} + \left(\frac{\overline{m}_2^{1/2} - \overline{m}_1^{1/2}}{{}^*\overline{m}_2^{1/2} - {}^*\overline{m}_1^{1/2}} \right) {}^*\overline{m}_1^{1/2} \right]^2 \quad (\text{A.25})$$

where \overline{m}_i , ${}^*\overline{m}_i$ with $i = 1, 2$ are pairs of isotopic masses in the old and the new time to mass calibrations corresponding to the same detection time. Thus, a pair of masses opportunely specified is necessary (and sufficient) to accomplish the mass correction.

A.7 Computations with SIMIONTM

In optics, sometimes ray-tracing programs are used to describe a complicated physical systems or/and to find the optical elements which best fits the requirements. In mass spectrometry as well, we need to solve complicated equations to fully characterize the real system. Even if in our case the arrangement of electrodes is given, we need to:

- find the set of potentials to maximize the performances (in terms of resolution and signal) for the range of masses under investigation;
- analyze common but difficult ion optics problems, adding perturbations to the system to resemble the actual physical conditions.

A commercial tool to numerically solve the resulting Laplacian equations is SIMION [90, 91]. The program requires as inputs a three dimensional geometric model for the electrodes configuration, a set of values for the electrode potentials, and information about the types of ions under investigation (e.g. masses, charges, starting positions and energies etc). SIMION has a random number generator (with uniform distribution) which can be used to perform Monte Carlo computations for different ion trajectories.

A 3D description of the Jordan Re-ToF MS, built to be used with SIMION, is shown in figure A.9. The model is built, with a 1 mm precision, to comply with the electrode distances of the Jordan spectrometer, specified in Table 4.3.1.

The potentials given as standard settings in the spectrometer user 's manual, were used to test SIMION with the built model of our Jordan apparatus. During this phase $N = 1000$ ions with same mass M were generated using the program. The simulated ions could then fly along the virtual mass spectrometer up to a detector. The associated times of flight, for ion masses, M , ranging from 1 Da to 300 Da, were found consistent with the experimental determinations on the real mass spectrometer with the same potentials applied.

To start optimization we generated N ($N = 75$) cations with same mass M . For an assigned set of potentials for the electrodes of the mass spectrometer, several values of M were considered:

$$M[\text{Da}] = 1 + i \times \frac{499}{14} \quad (\text{A.26})$$

with $i = 0, 1, 2, \dots, 14$.

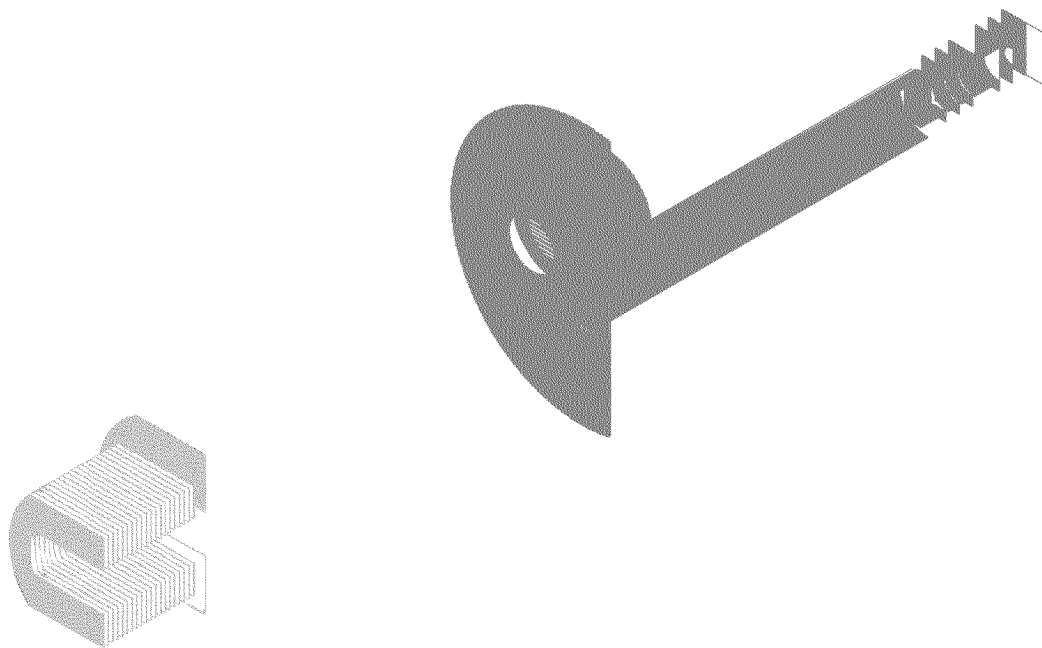


Figure A.9: A sketch of the 3D model of the Jordan ToF-spectrometer with reflectron. It is used by SIMION for numerical computations.

We assumed all ions having charge values of $+1$, which corresponds to select singly ionized atoms and molecules. Ion kinematic parameters have been generated in the following way:

	V_{A1} [V]	V_{A2} [V]	V_g [V]	V_{xy1} [V]	V_{xy2} [V]	V_{einzel} [V]	V_{R1} [V]	V_{R2} [V]
set₀	1153.1	848.4	0.0	55.0	0.0	250.0	643.5	1063.8
set₁	1191.7	876.8	0.0	60.0	0.0	250.0	665.1	1099.4
set₂	1233.1	907.2	0.0	65.0	0.0	250.0	688.2	1137.6
set₃	1277.4	939.8	0.0	70.0	0.0	250.0	712.9	1178.5
set₄	1325.1	974.9	0.0	75.0	0.0	250.0	739.5	1222.4
set₅	1376.4	1012.6	0.0	80.0	0.0	250.0	768.1	1269.7
set₆	1431.9	1053.5	0.0	85.0	0.0	250.0	799.1	1321.0
set₇	1491.9	1097.6	0.0	90.0	0.0	250.0	832.6	1376.3
set₈	1557.6	1145.9	0.0	95.0	0.0	250.0	869.2	1436.9
set₉	1628.9	1198.4	0.0	100.0	0.0	250.0	909.0	1502.7
set₁₀	1707.1	1255.9	0.0	105.0	0.0	250.0	952.6	1574.8
set₁₁	1793.1	1319.2	0.0	110.0	0.0	250.0	1000.7	1654.2
set₁₂	1888.7	1389.5	0.0	115.0	0.0	250.0	1054.0	1742.4
set₁₃	1994.4	1467.3	0.0	120.0	0.0	250.0	1113.0	1839.9
set₁₄	2113.1	1554.6	0.0	125.0	0.0	250.0	1179.2	1949.3
set₁₅	2246.9	1653.0	0.0	130.0	0.0	250.0	1253.9	2072.8
set₁₆	2398.4	1764.5	0.0	135.0	0.0	250.0	1338.4	2212.6
set₁₇	2572.2	1892.4	0.0	140.0	0.0	250.0	1435.4	2372.9
set₁₈	2772.6	2039.7	0.0	145.0	0.0	250.0	1547.3	2557.8
set₁₉	3008.3	2213.3	0.0	150.0	0.0	250.0	1678.8	2775.3

Table A.2: Potentials values to be applied to the electrodes of the mass spectrometer. They were determined by using the analytical approach described in the preceding text. The aim is to compare the previous prescriptions with the results of SIMION calculations, which should be more accurate dealing with the various physical parameters involved.

- starting positions ideally coincident with the center between the first two accelerations electrodes, with normal distribution around this point and variance along (x,y,z) directions equal to 0.02 mm. The gaussian distributed numbers were obtained with Box-Muller transformation [92] starting from the numbers generated by SIMION;
- initial momenta are randomly distributed in a cone with axis along the direction defined by the molecular beam. The max divergence is geometrically determined by the skimmer aperture and the distance from the molecular source, which is maximum 1.5° in our setup;
- kinetic energies of ions immediately after being formed is assumed to be uniformly distributed and centered around the kinetic energies of molecules in the molecular beam prior ionization, with 10% total width;
- no delays in the generation process are taken into account by considering times of birth (ToB) equal to 0 (these delays could be neglected with femtosecond laser ionization);
- sets of electrode potentials determined with the equations and the requirements given in section A.3 and A.5 are used. Indicated as set_i , with $i = 0, 1, 2, \dots, 19$, they are collected in table A.2. Set_i values of potentials indicated at the top of each column, are listed along row $(i + 1)$ of table A.2. The nomenclature used for potentials is the same introduced in previous sections (see Fig. A.3).

A.8 Simulation results

In Fig. A.10, ions trajectories ($M=100$ Da) computed with SIMION are indicated by red paths either inside the built in 3D model or over the potential surface (set_{19}) shown below. At the detector the time of flight distributions corresponding to set_0 potentials (see in table A.2) are plotted in Fig. A.11 for 75 positive ions of mass M , indicated on the right. A 0.4 ns bin size is used for all histograms. The vertical ranges are $[0, 60]$ for the first histogram ($M=1$) at the top side and $[0, 20/(1 + i \times 0.1)]$; $i = 1, 2, \dots, 14$ for the histograms below with masses $1 + i \times (499/14)$ respectively. As expected the broadening of the peak increases with mass, but the number of masses used (75) for our simulation does not allow for an accurate description of higher masses' distribution ($M > 150$ Da). For 108 Da the distribution appear to be gaussian with a 15 Da peak width (defined as its full width half maximum value, i.e. FWHM).

Figures A.12 and A.13 show time of flight histograms presented as in Fig. A.11 and obtained for set₉ and set₁₉, respectively. The peak broadening tendency for increasing masses is preserved as already observed in Fig. A.11. Generally for the same value of mass the FWHM is diminished constantly in correspondence to set₀, set₉ and set₁₉ potentials.

Fig. A.14 shows the histograms of the depth of ions' flight in the reflectron with M (ion mass) as parameter. The depth is expressed as a percentage of Δr , distance between its electrodes R1 and R2 (see Fig. A.3). The potentials assigned in the mass spectrometer are those of set₀, set₈ and set₁₆ (table A.2). The bin size and vertical ranges of all histograms are identical, i.e. 10 μm and [0, 25] respectively. The depth of ion flight decreases slightly for all potential sets when the ion mass increases. However the variations are smaller than 0.1%, which is consistent with eq. A.22.

It is interesting to compare the theoretical and simulated results for the time of flight. The theoretical time of flight can be computed by the equations A.10-A.15 using the potential sets in table A.2, masses given by eq A.26, and electrodes' distances of the Re-ToF-MS in table 4.3.1. The simulated time of flights are obtained averaging the time of flight of the iso-mass ions obtained for the same potential set. The results are plotted in Fig. A.15 versus the potential sets with ion mass as parameter. On the top side of Fig. A.15 the % difference (denoted as $\% \Delta$) between theoretical and simulated time of flights is shown. The time of flights determined theoretically result to be always longer than the simulated ones corresponding to the same mass. Although heavier ion masses exhibit an increase of their ToF differences, the corresponding percent difference does not exceed 5.5%. For a given mass, the discrepancy (in percent) between the two determinations tends to reach an absolute minima ($> 5\%$) in correspondence to extreme potential sets (below set₄-and above set₁₆). For lighter masses a local minimum between set₇ and set₁₃ is found ($> 5.2\%$).

From the comparison of simulated and theoretical results we can conclude that a difference of 5% justifies the procedure we adopted to optimize the potentials.

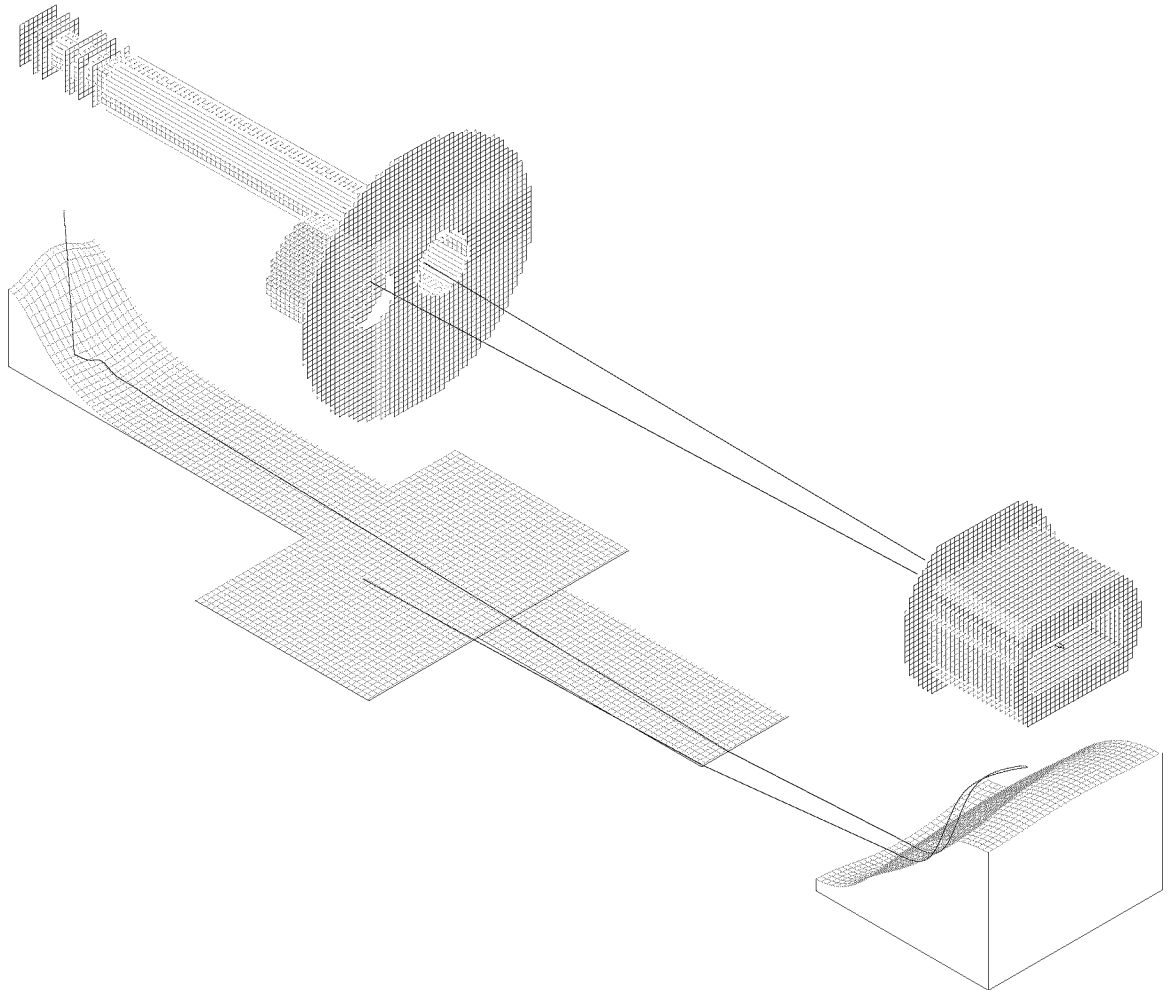


Figure A.10: The trajectories of the ions computed using SIMION. The ion flight paths have to be consistent with the geometrical constraint as well as with the voltage differences applied across the electrodes of the mass spectrometer, that determine all together the potential energy the ions are subjected to. On the bottom the effective potential energy surface found for the actual geometry of our spectrometer and the potential set₁₉ of table A.2 is shown.

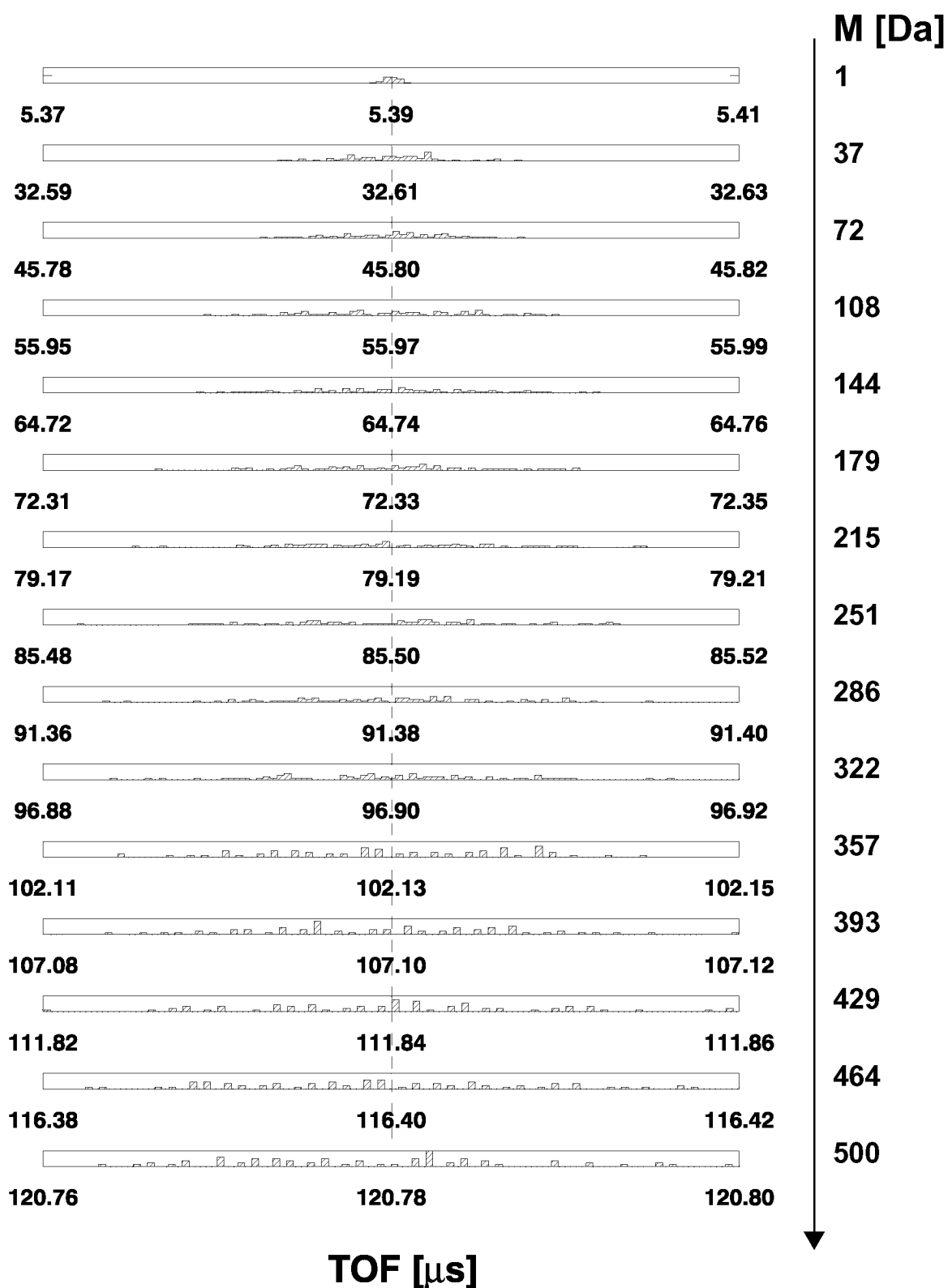


Figure A.11: Time of flight distribution at the detector of 75 positive ions all having mass M (shown on the right) when set_0 potentials (in table A.2) are used. The bin size is 0.4 ns for all histograms.

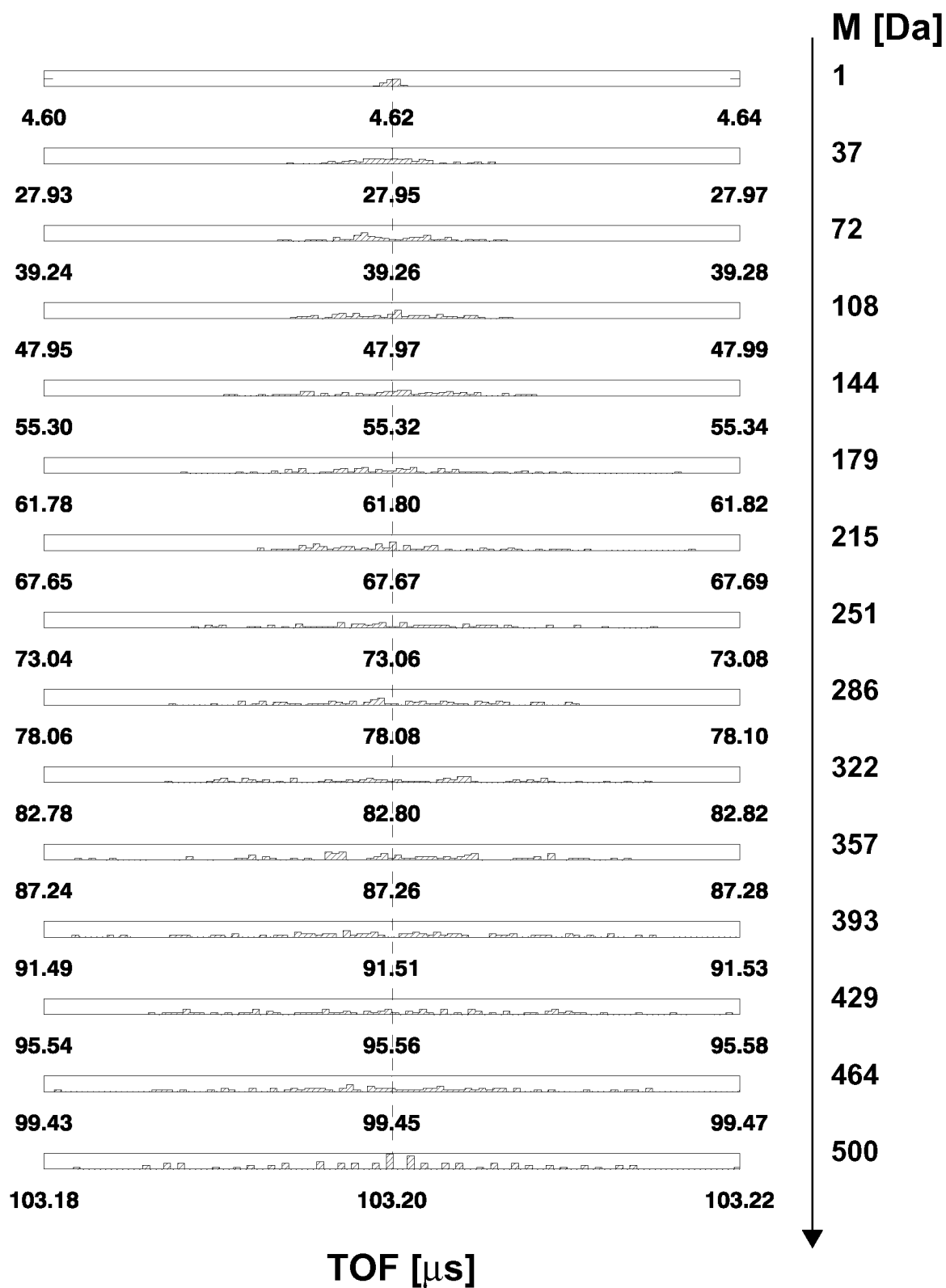


Figure A.12: Histograms of the times of flight at the detector of 75 ions all having mass M , indicated on the right side. The potentials in the mass spectrometer are those of set₉ (see table A.2), bin size and vertical scales are the same as in Fig. A.11.

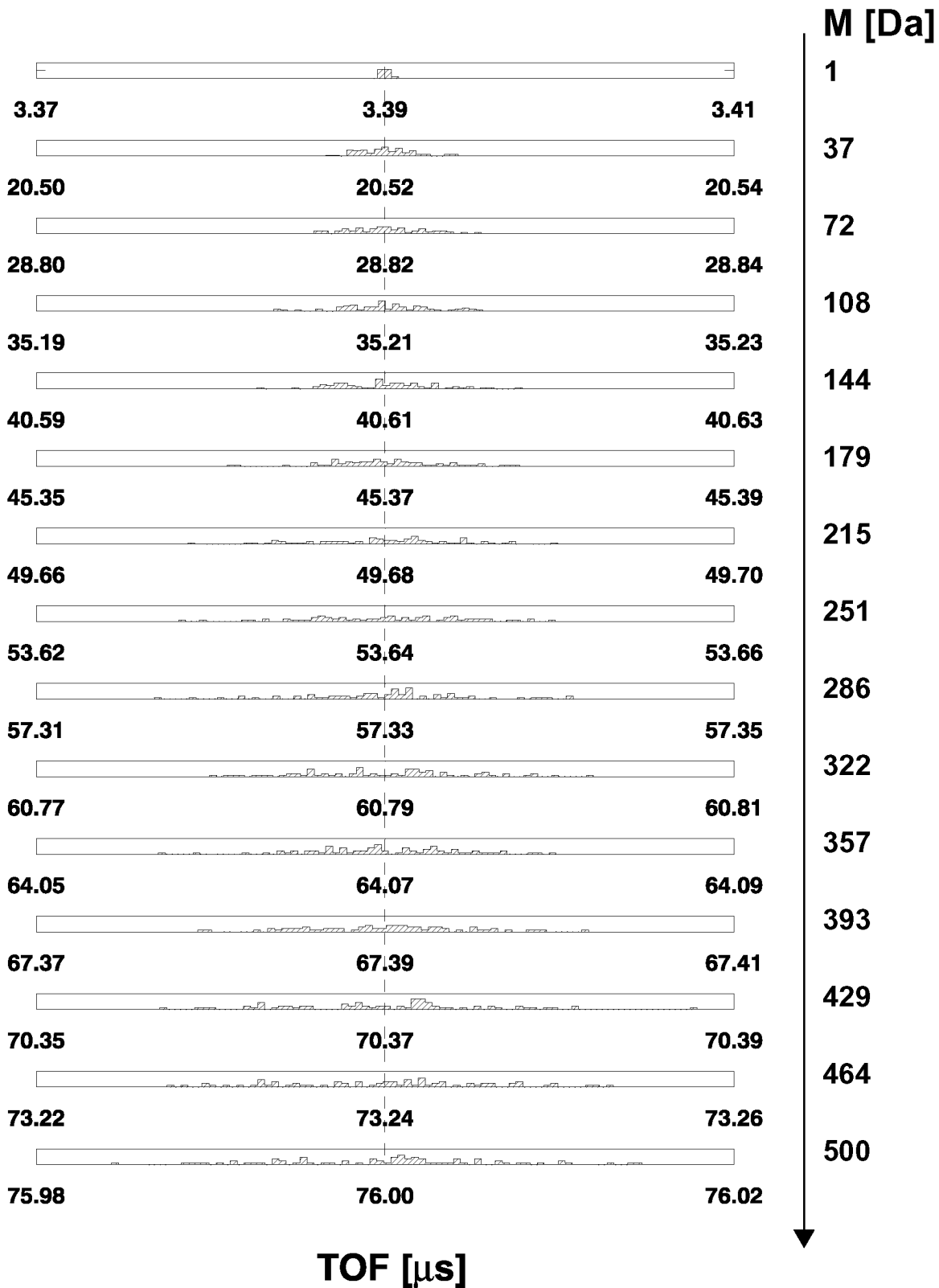


Figure A.13: The frequency distribution of the times of flight at the detector of 75 ions all having mass M , indicated on the right side, is obtained as in Figures A.11 and A.12 for the mass spectrometer potentials of set₁₉ (see table A.2).

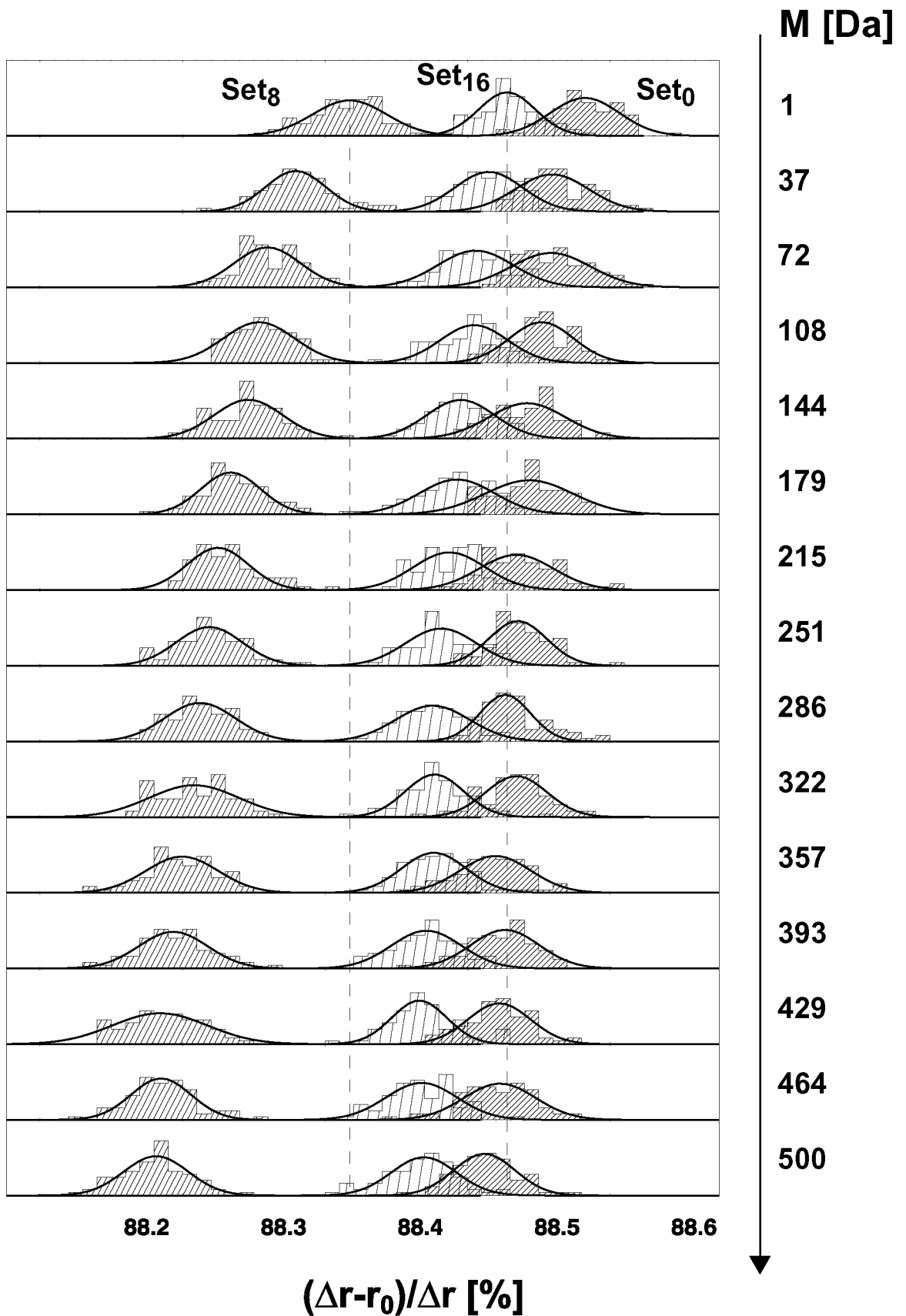


Figure A.14: Histograms of the depth of ions' flight in the reflectron expressed as a % of Δr , distance between its electrodes R1 and R2 (see Fig. A.3). The frequency distributions were determined with SIMION by letting 75 ions all having mass M , indicated on the right side, propagate through a model of our mass spectrometer. The set₀, set₈, and set₁₆ potentials are assigned in the mass spectrometer. The bin size and vertical range for all histograms are 10 μm and [0, 25] respectively.

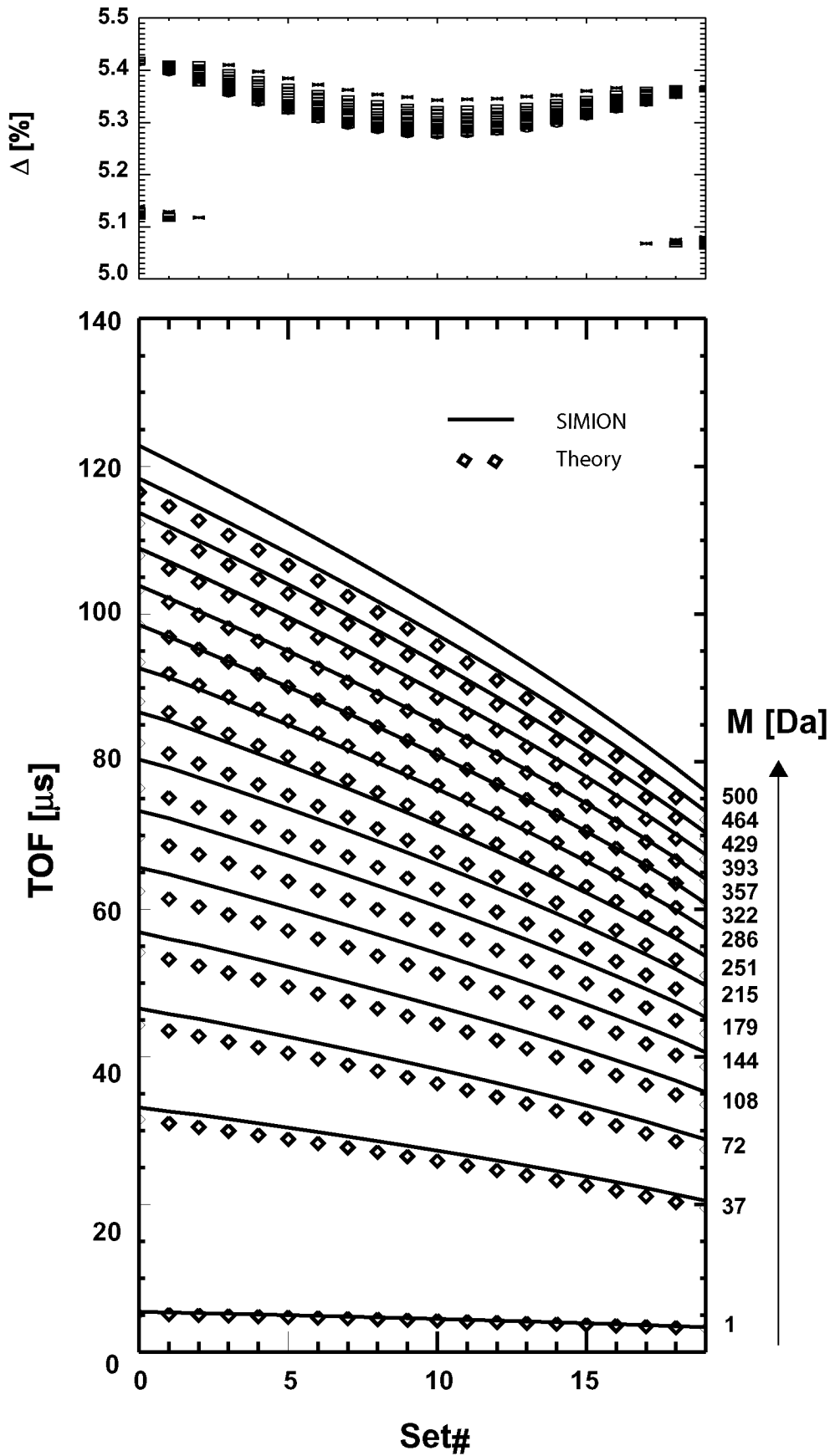


Figure A.15: The ions time of flight at the detector, computed analytically with the Eq. A.10 and A.20 are compared with the corresponding values determined using SIMION with the same sets of voltages (of table A.2) and masses. At the top the percent difference ($\% \Delta$) is shown versus potential sets.

Listing A.1: SIMION script that generates a 3D model of the electrodes comprised in the interaction region to be used in the simulations.

```
;source
pa_define (101,101,1201,p,n)

locate (50,50,0,1,0,0,0)
{
electrode(1)
{
fill
{
within
{
box3d(-22,-22,0,22,22,1)
}
}
}
}

electrode(2)
{
edge_fill
{
within
{
box3d(-6,-6,11,6,6,13)
}
notin {box3d(-7,-7,10,7,7,12)}
}
}
}

electrode(3)
{
fill
{
within
{
box3d(-22,-22,13,22,22,14)
}
notin {circle(0,0,6,6)}
}
}
}

electrode(4)
{
edge_fill
{
```

```
    within
    {
        box3d(-13,-13,24,13,13,26)
    }
    notin {box3d(-14,-14,23,14,14,25)}
}

electrode(5)
{
    fill
    {
        within
        {
            cylinder(0,0,50,15,15,24)
        }
        notin {circle(0,0,13,13)}
    }

    fill
    {
        within
        {
            box3d(-22,-22,26,22,22,27)
        }
        notin {circle(0,0,13,13)}
    }
}

electrode(6)
{
    fill
    {
        within
        {
            cylinder(0,0,63,15,15,11)
        }
        notin {circle(0,0,13,13)}
    }

    fill
    {
        within
        {
            box3d(-22,-22,52,22,22,53)
        }
    }
}
```

```
        notin { circle (0,0,13,13) }
    }
}

electrode(7)
{
    fill
    {
        within
        {
            cylinder(0,0,76,15,15,11)
        }
        notin { circle (0,0,13,13) }
    }

    fill
    {
        within
        {
            box3d(-22,-22,65,22,22,66)
        }
        notin { circle (0,0,13,13) }
    }
}

electrode(8)
{
    fill
    {
        within
        {
            box3d(-22,-22,78,13,22,79)
        }
        notin { box3d(-13,-13,77,13,13,80) }
    }

    fill
    {
        within
        {
            box3d(-15,-15,78,13,15,103)
        }
        notin { box3d(-13,-13,77,16,13,104) }
    }
}
```

```
electrode(9)
{
  fill
  {
    within
    {
      box3d(-22,-22,78,22,22,79)
    }
    notin {box3d(-23,-23,77,14,23,80)}
  }

  fill
  {
    within
    {
      box3d(-10,-12,78,15,12,103)
    }
    notin {box3d(-15,-13,77,13,13,104)}
  }
}

electrode(10)
{
  fill
  {
    within
    {
      cylinder(0,0,426,27,27,330)
    }
    notin {circle(0,0,25,25)}
  }
}

;electrode(12)
; {
; fill
; {
;   within
;   {
;     cylinder(0,0,1082,2,2,692)
;   }
; }
; }
```

Listing A.2: SIMION script that generates the 3D model of the electrodes comprised in the reflectron to be used in the simulations.

```
; reflectron
pa_define (201,201,601,p,n)

locate (100,100,400,1,0,0,0)
{
electrode(1)
  {
    fill
      {
        within_inside_or_on
          {
            box3d(-1000,-72.5,0,1000,72.5,1)
            circle(0,0,86,86)
          }
        notin_inside_or_on
          {
            box3d(-1000,-19,0,1000,19,2)
            circle(0,0,51,51)
          }
      }
  }

electrode(2)
  {
    fill
      {
        within_inside_or_on
          {
            box3d(-1000,-50,12,1000,50,13)
            circle(0,0,72.5,72.5)
          }
        notin_inside_or_on
          {
            box3d(-1000,-19,11,1000,19,14)
            circle(0,0,51,51)
          }
      }
  }

electrode(3)
  {
    fill
      {
        within_inside_or_on
```

```
        {
        box3d(-1000,-50,17,1000,50,18)
        circle(0,0,72.5,72.5)
        }
        notin_inside_or_on
        {
                box3d(-1000,-19,16,1000,19,19)
                circle(0,0,51,51)
        }
    }
}

electrode(4)
{
    fill
    {
        within_inside_or_on
        {
            box3d(-1000,-50,22,1000,50,23)
            circle(0,0,72.5,72.5)
        }
        notin_inside_or_on
        {
                box3d(-1000,-19,21,1000,19,24)
                circle(0,0,51,51)
        }
    }
}

electrode(5)
{
    fill
    {
        within_inside_or_on
        {
            box3d(-1000,-50,27,1000,50,28)
            circle(0,0,72.5,72.5)
        }
        notin_inside_or_on
        {
                box3d(-1000,-19,26,1000,19,29)
                circle(0,0,51,51)
        }
    }
}
```



```
electrode(6)
{
  fill
  {
    within_inside_or_on
    {
      box3d(-1000,-50,32,1000,50,33)
      circle(0,0,72.5,72.5)
    }
    notin_inside_or_on
    {
      box3d(-1000,-19,31,1000,19,34)
      circle(0,0,51,51)
    }
  }
}

electrode(7)
{
  fill
  {
    within_inside_or_on
    {
      box3d(-1000,-50,37,1000,50,38)
      circle(0,0,72.5,72.5)
    }
    notin_inside_or_on
    {
      box3d(-1000,-19,36,1000,19,39)
      circle(0,0,51,51)
    }
  }
}

electrode(8)
{
  fill
  {
    within_inside_or_on
    {
      box3d(-1000,-50,42,1000,50,43)
      circle(0,0,72.5,72.5)
    }
    notin_inside_or_on
    {
      box3d(-1000,-19,41,1000,19,44)
    }
  }
}
```

```
        circle(0,0,51,51)
    }
}
}
electrode(9)
{
    fill
    {
        within_inside_or_on
        {
            box3d(-1000,-50,47,1000,50,48)
            circle(0,0,72.5,72.5)
        }
        notin_inside_or_on
        {
            box3d(-1000,-19,46,1000,19,49)
            circle(0,0,51,51)
        }
    }
}
electrode(10)
{
    fill
    {
        within_inside_or_on
        {
            box3d(-1000,-50,52,1000,50,53)
            circle(0,0,72.5,72.5)
        }
        notin_inside_or_on
        {
            box3d(-1000,-19,51,1000,19,54)
            circle(0,0,51,51)
        }
    }
}
electrode(11)
{
    fill
    {
        within_inside_or_on
        {
            box3d(-1000,-50,57,1000,50,58)
```

```
        circle(0,0,72.5,72.5)
    }
    notin_inside_or_on
    {
        box3d(-1000,-19.56,1000,19.59)
        circle(0,0,51,51)
    }
}
}

electrode(12)
{
    fill
    {
        within_inside_or_on
        {
            box3d(-1000,-50.62,1000,50.63)
            circle(0,0,72.5,72.5)
        }
        notin_inside_or_on
        {
            box3d(-1000,-19.61,1000,19.64)
            circle(0,0,51,51)
        }
    }
}

electrode(13)
{
    fill
    {
        within_inside_or_on
        {
            box3d(-1000,-50.67,1000,50.68)
            circle(0,0,72.5,72.5)
        }
        notin_inside_or_on
        {
            box3d(-1000,-19.66,1000,19.69)
            circle(0,0,51,51)
        }
    }
}

electrode(14)
```

```
{
  fill
  {
    within_inside_or_on
    {
      box3d(-1000,-50,72,1000,50,73)
      circle(0,0,72.5,72.5)
    }
    notin_inside_or_on
    {
      box3d(-1000,-19,71,1000,19,74)
      circle(0,0,51,51)
    }
  }
}

electrode(15)
{
  fill
  {
    within_inside_or_on
    {
      box3d(-1000,-50,77,1000,50,78)
      circle(0,0,72.5,72.5)
    }
    notin_inside_or_on
    {
      box3d(-1000,-19,76,1000,19,79)
      circle(0,0,51,51)
    }
  }
}

electrode(16)
{
  fill
  {
    within_inside_or_on
    {
      box3d(-1000,-50,82,1000,50,83)
      circle(0,0,72.5,72.5)
    }
    notin_inside_or_on
    {
      box3d(-1000,-19,81,1000,19,84)
      circle(0,0,51,51)
    }
  }
}
```

```
    }  
  }  
}  
  
electrode(17)  
{  
  fill  
  {  
    within_inside_or_on  
    {  
      box3d(-1000,-50,87,1000,50,88)  
      circle(0,0,72.5,72.5)  
    }  
    notin_inside_or_on  
    {  
      box3d(-1000,-19,86,1000,19,89)  
      circle(0,0,51,51)  
    }  
  }  
}  
  
electrode(18)  
{  
  fill  
  {  
    within_inside_or_on  
    {  
      box3d(-1000,-50,92,1000,50,93)  
      circle(0,0,72.5,72.5)  
    }  
    notin_inside_or_on  
    {  
      box3d(-1000,-19,91,1000,19,94)  
      circle(0,0,51,51)  
    }  
  }  
}  
  
electrode(19)  
{  
  fill  
  {  
    within_inside_or_on  
    {  
      box3d(-1000,-50,97,1000,50,98)  
      circle(0,0,72.5,72.5)  
    }  
  }  
}
```

```
    }
    notin_inside_or_on
    {
        box3d(-1000,-19,96,1000,19,99)
        circle(0,0,51,51)
    }
}
}

electrode(20)
{
    fill
    {
        within_inside_or_on
        {
            box3d(-1000,-50,102,1000,50,103)
            circle(0,0,72.5,72.5)
        }
        notin_inside_or_on
        {
            box3d(-1000,-19,101,1000,19,104)
            circle(0,0,51,51)
        }
    }
}

electrode(21)
{
    fill
    {
        within_inside_or_on
        {
            box3d(-1000,-50,107,1000,50,108)
            circle(0,0,72.5,72.5)
        }
        notin_inside_or_on
        {
            box3d(-1000,-19,106,1000,19,109)
            circle(0,0,51,51)
        }
    }
}
}
```

Listing A.3: SIMION script that generates the geometry model of electrodes comprised in the detection section, including the 40 mm MCP.

```
;detector
pa_define (301,301,201,p,n)

locate (150,150,100,1,0,0,0)
{

electrode(1)
{
  fill
  {
    within
    {
      cylinder(0,0,1,127,127,2)
    }
    notin
    {
      circle(26,0,26,26)
    }
    notin
    {
      circle(-49,0,22,22)
    }
  }
}

electrode(2)
{
  edge_fill
  {
    within
    {
      cylinder(-49,0,-20,22,22,1)
    }
    notin
    {
      cylinder(-49,0,-21,23,23,4)
    }
  }
}

electrode(3)
{
```

```
fill
{
  within
  {
    cylinder(-49,0,-25,44,44,48)
  }
}
}
```

A.9 Data evaluation and isotope distributions

The mass spectrum analysis requires that the isotopic pattern of at least three elements is recognized. The corresponding assignments of their relative masses allows a calibration procedure that returns the parameters of the quadratic law between mass and time. The question that rises is how to interpret the other peaks and univocally assign them to elements. The problem can become soon not easy to be solved as higher masses are taken into account.

A.9.1 C code to calculate for a molecule the relative isotopic abundance

I developed a small program, starting from a gnu code, written in C and available on internet. It has a graphical interface, I developed using using IDL, which increases its usability. It requires a list of molecules or chemical compounds as input that the user guess to play a role in the mass spectrum. The program also needs a list of numbers representing the contribute of each compound to give the mass pattern observed.

Appendix B

Ablation and plume characteristics

In this appendix we describe shortly the effects of a nanosecond laser pulse impinging on a surface of a metal sample. The laser irradiation initiates a sequence of events which extend up to few microseconds after the short laser pulse. During the interaction between an incident laser beam pulse and a metal target, part of the laser beam energy is reflected back and part is absorbed, within a short penetration depth, by the metal (see Fig. B.1, (A)-(B)). As a result of the surface absorption, the metal transiently change phase to both liquid (melting) and vapor (sublimation/evaporation), as illustrated in Fig. B.1, (B)-(C)). The generated vapor may consist of neutrals, excited species and dissociated and ionized

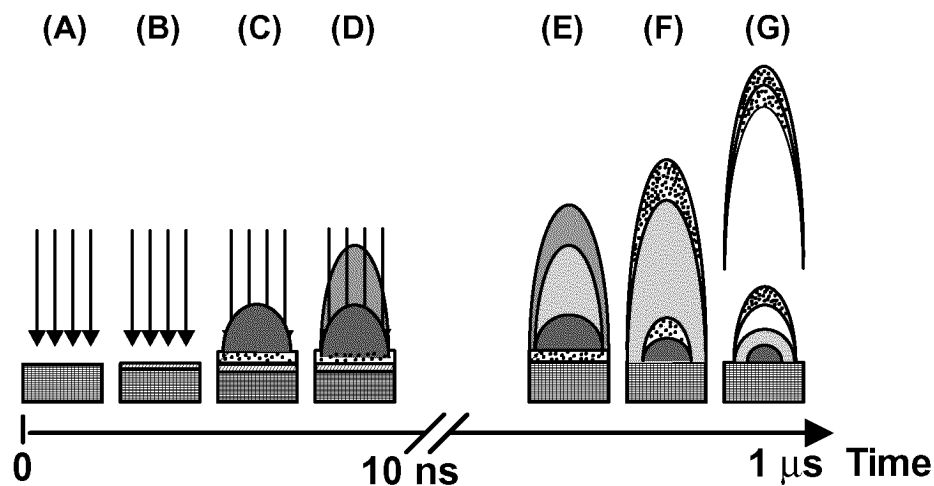


Figure B.1: Plasma plume development and material detachment produced by a nanosecond laser pulse. The process extends well after the short time during which the laser beam illuminates the material surface.

atoms or molecules, thus creating a high density plasma which subtracts part of the energy of the incident laser beam (Fig. B.1, (C)-(D)). This causes the plasma temperature to rise (due to the corresponding variation of its internal energy). Thereby the degree of ionization

of the vapor is also increased, leading to a further enhanced absorption of the trailing part of the laser beam. This positive feedback mechanism makes the plasma behaves like a thick medium providing a progressive shielding of the target surface from the impinging energy. Once the high temperature plasma is formed in the vapor phase above the target surface, its energy is transferred away via radiative exchanges with the target material/ambient and by the acceleration of the vapor to hypersonic velocities. The hot plasma transfers energy to the target via the normal electron heat conduction, in addition to a combination of the following two mechanisms [93]:

- Short-wavelength thermal plasma radiation absorbed by the target surface;
- Phase change of the vapor which condenses due to the plasma pressure insisting at the interface with the target.

Such an efficient thermal coupling between plasma and target is often referred to as 'plasma-enhanced'. This underlines the plasma key role in the context of this phenomenon, when its inner mechanisms are not yet fully unveiled. The complexity of the laser-plasma-target interactions accounts for additional heat flux contributions to the target surface which might exceed the loss of laser light due to the plasma absorption (see Fig. B.1, **(D)**-**(E)**). Thus, the combination of the expansion of the saturated gas and the heat transfer at the contact surface between the plume and ambient leads to a very rapid cooling (as shown in Fig. B.1, **(F)**-**(G)**). We have favorable conditions for the homogeneous nucleation of the condensate vapor, according to classical condensation theory, if the time for the cooling process is much shorter than the time needed for the condensation.

The saturation ratio $S = p_v/p_s$, namely the ratio between the actual vapor pressure and the saturation pressure for a given temperature, tends to assume high values with the cooling. Its impact on the proceeding of the homogeneous nucleation can be noticed in the equation for the free energy of a spherical condensed cluster of radius r [94]:

$$\Delta G = -\frac{4}{3}\pi r^3 N \Delta\mu + 4\pi r^2 \sigma \quad (\text{B.1})$$

where $\Delta\mu = k_b T \ln S$ is the chemical potential difference between condensed and uncondensed atoms (k_b , T being the Boltzmann constant, and the vapor temperature, respectively), N is the atom density and σ is the surface tension.

The velocity distributions of ablated particles are expressed in terms of a Maxwell-Boltzmann distribution function on a stream velocity u directed along the z axis [95]:

$$dN(\vec{v}, T, u) = \left(\frac{m}{2\pi k_b T} \right) \exp \left\{ -\frac{m [v_x^2 + v_y^2 + (v_z - u)^2]}{2k_b T} \right\} dv_x dv_y dv_z \quad (\text{B.2})$$

where m denotes the particle mass, v_x , v_y and v_z are the components of the velocity \vec{v} in the corresponding Cartesian directions, and k_b is the Boltzmann constant. The ablation process in general can be described as combination of thermal and non-thermal effects. For thermal ablation it is assumed that all energy is transferred into heat and the material cannot compensate the absorbed energy by heat conductivity because of the short pulse durations (~ 10 ns) and hence evaporates in the target area. The non-thermal contribution would include photo-absorption in the ablated material and fragmentation via dissociating channels. Reaching several hundreds of MW/cm² of ablation energy, ionization of the ablated material becomes dominant and a plasma plume above the ablated surface [96] is generated. Nevertheless the ionization of the plume results from a combination of laser induced ionization and a secondary ionization from highly energetic electrons in the plasma. The electrons gain kinetic energy due to inverse ‘Bremsstrahlung’ and therefore increase their ionization cross section. This means that as long as the ion density of the plasma increases the plasma plume absorption ability to the ablation laser light is enhanced. Finally no direct radiation reaches the material surface and only secondary radiation hits the metal surface. However the optimal laser intensity used in our experiment is below the breakdown threshold of most gases, and the ionization degree of the plume is expected to be sufficiently characterized by taking into account the thermal balance [97]. The ionization state of the plasma may be approximated by using the density corrected ‘Saha’ equation [98]:

$$\frac{n^{i+}}{n^{(i-1)+}} \approx 2 \frac{\sqrt{(2\pi m_e k)^3} T_e^{3/2}}{h^3} \frac{T_e^{3/2}}{n_e} \exp(-E_{ion}^{i+}/kT_e) \quad (\text{B.3})$$

where n^{i+} is the number density of i 'th ionization state of the ablated material, n_e is the number density of electrons, T_e is the temperature of the plasma and E_{ion}^{i+} is the ionization energy. The highest ionization degree is expected at the highest plasma temperature, which is expected to be at the end of the laser pulse [94].

Assuming that the total ablation rate is $N_{tot} = n^+ + n^{++} + n^0$, the number of ions as a function of the plasma temperature (neglecting higher ionization stages and degeneracy factors) can be estimated from eq. B.3, as plotted in Figures B.2 and B.3. The number ratio of Zn^+ / N_{tot} in the plume changes between 0 and 1 in the expected temperature range between 2000 and

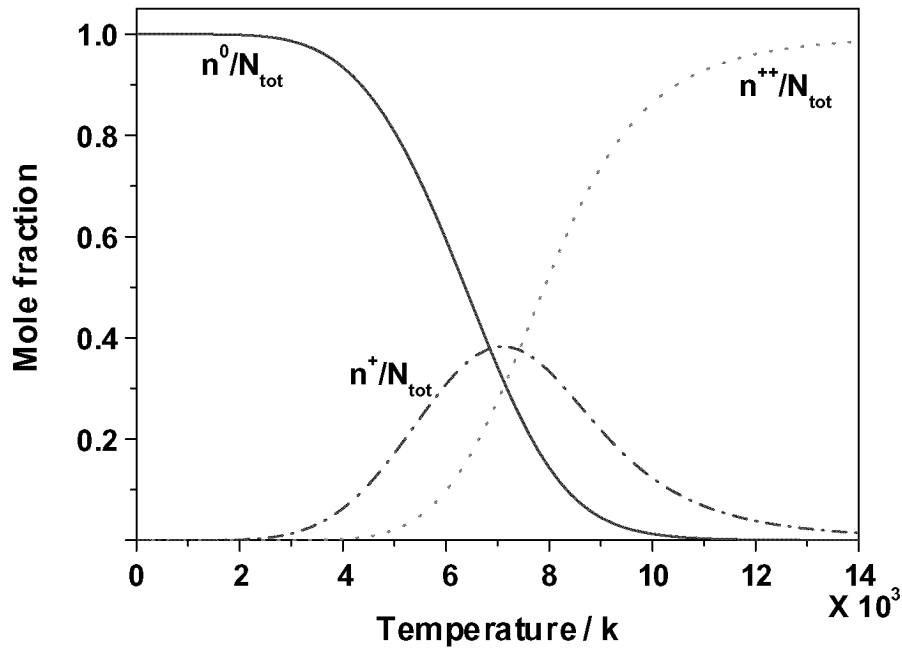


Figure B.2: Temperature variation of the plasma composition. It has been computed in Matlab by solving the Saha equation which prescribes a thermal equilibrium between neutral Nb atoms and its single and double charged ions.

7000 K. At higher temperatures (higher laser ablation power) the Zn^+ concentration decays and Zn^{++} ions become more abundant. This endorses our belief that the ZnX compound formation most effectively starts from Zn^+ cations.

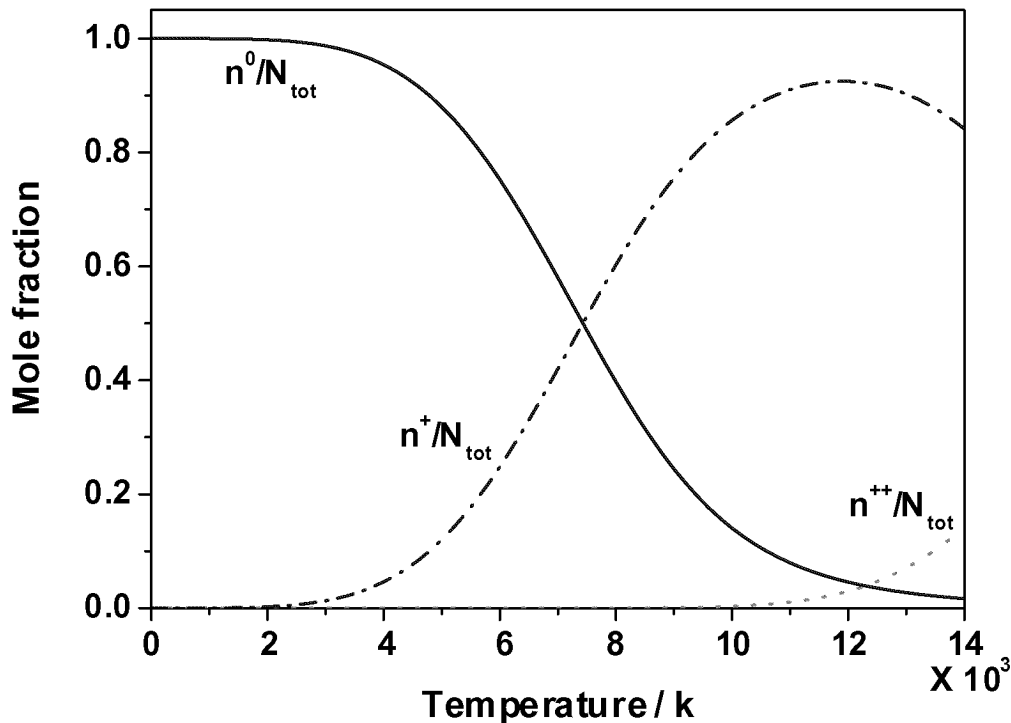


Figure B.3: As in Figure B.2, the relative abundances of Zn neutral atoms, Zn^+ and Zn^{++} with temperature is shown as computed using Saha eq. B.3.

Appendix C

Labview, Drivers, programs

In this appendix, we describe some of the programs we developed to automate the data collection. The programs were also useful to prepare the experimental setup for spectroscopic measurements and/or perform parallel experiments using a different setup.

C.1 Programs to scan with a SpeX monochromator

A spectrometer Spex (model 500M) is available in the Combustion Research laboratory for experiments [99]. With a 0.5 m focal length and a grating of 1200 grooves/mm, it is optimized for use in the visible (300 nm to 800 nm) range. The spectrometer grating is

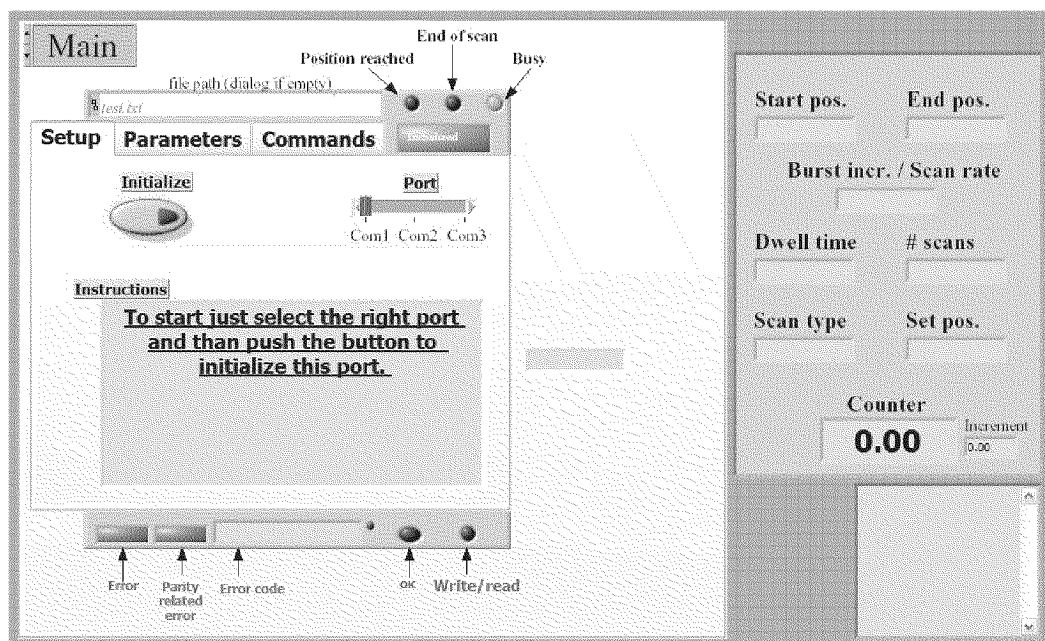


Figure C.1: Interface of the Labview program we developed in order to drive the SpeX monochromator, through the SpeX compudrive, sampling electric signals with the boxcar.

driven by a stepper motor, which is controlled by a Spex CD2A CompuDrive system [100] consisting of a command keyboard and a drive controller. In order to implement a basic scanning system we developed a Labview program with a graphical interface to set and read all the system's parameters (e.g. time, grating order, comments, etc). A initialization of the SpeX driver was operated by (manually) setting its internal registers for external communication. It allowed a PC to remotely control the SpeX compudrive being connected through a serial cable terminated by a null modem adapter.

C.1.1 PMT in combination with a Boxcar

I have developed with LabView a software program to acquire electrical signals with the Stanford Research Scientific Boxcar. The implemented code can collect, digitalize, average and store data in remote mode. It allows us to deal with signals at a maximum frequency of about 100 Hz (although the Boxcar itself can operate with faster inputs).

C.1.2 ICCD camera and Winview

The optics that couple the camera to the monochromator and the camera chip size limit the effective range of wavelength acquired by the camera, for each shot, to a few nm. Thus, in order to extend the spectra over several hundred of nm, it is necessary to scan the grating position while storing the camera shots. Each shot is taken partially overlapped with the preceding and subsequent ones to guarantee a good reconstruction of the spectrum with the wavelength. The program Winview can assist the researcher automatizing this procedure for a restricted number of cameras and spectrometers but does not support the pair of devices used in our setup. Therefore I wrote a script in Winview macrolanguage [101] that could access through the serial port the SpeX driver monochromator and actuate the gratings movements for a continuous scan during acquisition.

Script to scan the grating and average the signal

The script I implemented waits for the grating to reach defined intermediate positions prior acquiring N images (or spectra) with the camera to average out. It requires the user to set the SpeX controller for serial port communication (see parameters in the script and the controller manual for a congruent adjustment). In addition starting position, end position and step size for the scan should also be provided as input through keyboard into the SpeX

controller.

Listing C.1: Acquisition script developed for Winview to store sequential scans while the grating position of monochromator is changed.

```

REM      SPeX.CMD

rem **** start EXPERIMENT SETUP DOWNLOAD
long Timer          rem: Define a timer handle
long ElapsedTime
long TimeToWait
long totn
long indx
STRING filestr , indxstr

PHYPORT CommPtr
string SendString , SendStringb
string OneChar, FirstChar , loopstr
string InputBuffer
string ClearLine
uint OutQueueSize, InQueueSize
int NumInChars
int BaudRate , ByteSize , DeviceNumber
int MaxPorts , OutQueSize, Parity
int StopBits , UseDef
long Timer          rem: Define a timer handle
long TimeToWait
int ii , flag , loop , loopmax , totnch

int   MaxChars, SPort
STRING PrintString ( 100 )      rem: Up to 100 chars per line

let MaxChars = 100              rem: Up to 100 chars per line set in variable
let SPort = 1
let flag=0
let ii=0
let loopmax=1
let loop=0
let totnch=0
rem ::::::::::::::::::::::::::::::::::::::::::::::::::::::::::::::::::::::::::::
rem ::::::::::::::::::::::::::::::::::::::::::::::::::::::::::::::::::::::::::::

int   length , LineCounter
STRING PrintFile
byte   CR, LF, FF
byte   FillChar , OneByte

let CR = 13                      rem: Carriage Return

```

```

let LF = 10          rem: Line Feed
let FF = 12          rem: Form Feed
let CAN = 24         rem: start command
let ETX = 03         rem: end line

let tmp = SPACE( ClearLine, 80 )
let tmp = CREATEPHY( 6 ) rem: Create serial port
let tmp = PHYSETBYTESIZE( 8 ) rem: Set Byte Size to 8 bits
let tmp = PHYSETSTOPBITS( 0 ) rem: Set 1 Stop Bit
let tmp = PHYSETPARITY( 0 ) rem: Set NO Parity
let tmp = PHYSETBAUDRATE( 9600 ) rem: Set Baud Rate to 9600
let tmp = PHYSETUSEDEF( 0 ) rem: Use these parameters instead of

let FillChar = 0      rem: Use NULL for filler char needed by READSTRING()

let tmp = CREATEPHY( 6 )          rem: Create Serial-type port
let tmp = PHYSETUSEDEF( 1 )       rem: Use WINDOWS defaults for port
let tmp = PHYSETDEVICENUMBER( SPort ) rem: Set device to Serial
LET tmp = PHYINITIALIZE           rem: This actually opens the port
let tmp = PHYRESETINTERFACE

if PHYSTATUS # 1 then
    let tmp = MESSAGE( "SERIAL_PORT_INITIALIZATION_FAILED!", 0 )
endif

let doneflag = 0
let didCR = 0
let NumInChars = 1
let MaxRows = 19
let SendStringb="acq"

let TimeToWait = 25

rem input "iterations?",loopmax

while loop <= loopmax
let indx = 1
let totn = 1
let flag=0
let totnch=0
if loop=0 then
input "iterations?",loopmax, "filename?",SendStringb
endif

```



```

let loop=loop+1

let tmp = STR( loop, loopStr )
let tmp = STRCAT( SendStringb, loopstr, SendString )
let tmp = STRCAT( SendString, "_", SendString )

rem: Send String to device
let tmp = PHYOUTPUT( CAN, 0 ) rem: Send CR/LF
let tmp = PHYSENDSTRING("T", 1 )
while PHYGETCURRENTOUTQUE > 0
NOP rem: Just wait for it to be done
wend
let tmp = PHYOUTPUT( ETX, 0 ) rem: Send CR/LF
let tmp = PHYOUTPUT( CR, 0 ) rem: Send CR/LF
rem: With some devices, LF confuses it,
rem: So commented out...
rem: let tmp = PHYOUTPUT( LF, 0 )

while flag = 0
string InputBuffer
if PHYGETCURRENTINQUE > 0 then

rem: Read in a Character
let inchar = PHYINPUT( 0 )
let OneChar = inchar

if onechar="S" then
let inchar = PHYINPUT( 0 )
for ii=1 to 8
let inchar = PHYINPUT( 0 )
let OneChar = inchar
let tmp = STRCAT( InputBuffer, OneChar, InputBuffer )
next ii
let flag=1
endif

endif
wend

let flag=0

XCONTROLLER Controller

```

```

let tmp = SETDATAFILEINCFILAG ( 0 )

let Controller = DOWNLOADRUNASPERIMENT (
    "c:\winspeco\test.spe", rem run data file
        2, rem run filetype
        6, rem run datatype
        2, rem run access
    FALSE, rem confirmation flag
    TRUE, rem Auto DataType Select
    TRUE, rem Store Synchronous
    TRUE, rem autoscaling flag
    FALSE, rem autoresizing flag
        0, rem low intensity
    16000, rem high intensity
    TRUE ) rem CheckingDone

rem **** end EXPERIMENT RUN AS DOWNLOAD

let tmp = SETAUTOSTORE( 1 )
let Controller = DOWNLOADSETUP (
    0, rem exposure time
    2, rem timeunit
    0, rem reserved
    TRUE, rem synchronous flag
    1, rem sequential frames
    10, rem accumulations
    0, rem clean frames
    10, rem timing mode
    0, rem Kinetics Trigger Mode
    3, rem shutteroperation
    TRUE, rem background flag
    "c:\winviewn\back.spe", rem background file name
        2, rem background file type
    FALSE, rem flatfield flag
    "", rem flatfield file name
        2, rem flatfield file type
    TRUE, rem imageaccess flag
    0, rem upper
    0, rem left
    0, rem lower
    0, rem right
    2296, rem x group size
    17704, rem y group size
    FALSE, rem ST138 HW Accumulation
    0, rem Blemish Removal OFF
    "", rem Blemish File Name

```

```

        0,      rem Cosmic Removal Spatial OFF
        0.00,   rem Threshold Not Used
        0.00,   rem Grass Height Not Used
        0 )     rem Cosmic Removal Temporal OFF

let tmp = SETEXPSETUPSOFTBIN ( 0 )   rem Software Binning OFF

let tmp = CLEARACCESSPATTERN

let tmp = ADDACCESSPATTERN( 1,1,384,576,1,384 )
rem **** end  EXPERIMENT SETUP DOWNLOAD
while totn=1
let tmp = CLEARPRINTWINDOW
PRINT indx, 1, 1, 0
if totnch=1 then
let totn=0
let flag=1
endif
let tmp = STR( indx, indxStr )
let tmp = STRCAT( SendString, indxStr, filestr )
let tmp = STRCAT( filestr, ".prn", filestr )
let indx=indx+1

let tmp = STARTEXPERIMENT

let tmp = STARTCONTROLLER

let tmp = WAITFOREXPERIMENT

let tmp = STOPEXPERIMENT

IMEXPORT ImexpObject

let ImexpObject = DOWNLOADIMEXP (
    2,
    "c:\winspeco\test.spe",
    filestr,
    18,   rem Export to ASCII-XY
    0,   rem Number of bits
    1,   rem Start frame
    1,   rem End frame
    1,   rem Skip frame
    1,   rem Start strip
    1,   rem End strip
    1,   rem Skip strip
    1,   rem Start pixel

```

```

576,    rem End pixel
1,      rem Skip pixel
565.000000,    rem Min Intensity
810.140000,    rem Max Intensity
FALSE, rem Not used for export
FALSE, rem Not used for export
FALSE, rem Not used for export
TRUE,    rem FALSE= Display error messages
0,
"LL",
0 )    rem Don't use calibration
let tmp = SETIMEXPINCFLAG( ImexpObject, 0 )    rem Disable file increments

let tmp = RUNEXPORT ( ImexpObject )

if flag=0 then
rem: Send String to device
let tmp = PHYOUTPUT( CAN, 0 ) rem: Send CR/LF
let tmp = PHYSENDSTRING("E", 1 )
while PHYGETCURRENTOUTQUE > 0
NOP rem: Just wait for it to be done
wend
let tmp = PHYOUTPUT( ETX, 0 ) rem: Send CR/LF
let tmp = PHYOUTPUT( CR, 0 ) rem: Send CR/LF
rem: With some devices, LF confuses it,
rem: So commented out...
rem: let tmp = PHYOUTPUT( LF, 0 )
endif

while flag = 0
string InputBuffer
if PHYGETCURRENTINQUE > 0 then

rem: Read in a Character
let inchar = PHYINPUT( 0 )
let OneChar = inchar

if onechar="B" then
let inchar = PHYINPUT( 0 )
for ii=1 to 8
let inchar = PHYINPUT( 0 )
let OneChar = inchar
let tmp = STRCAT( InputBuffer, OneChar, InputBuffer )
next ii
let flag=1

```

```

elseif onechar="S" then
let inchar = PHYINPUT( 0 )
for ii=1 to 8
let inchar = PHYINPUT( 0 )
let OneChar = inchar
let tmp = STRCAT( InputBuffer, OneChar, InputBuffer )
next ii
let flag=1
elseif onechar="E" then
let totnch=1
let inchar = PHYINPUT( 0 )
if inchar="A" then
for ii=1 to 8
let inchar = PHYINPUT( 0 )
let OneChar = inchar
let tmp = STRCAT( InputBuffer, OneChar, InputBuffer )
next ii
endif
let flag=1

endif

endif
wend

let flag=0
wend

if loop=loopmax then
let loopmax=1
let loop=0
let SendStringb="acq"
let totnch=0
endif
let flag=0
wend

let tmp = DESTROYTIMER( Timer )
rem: Clean up on the way out
let tmp = PHYDESTROY
REM          ***** end of MACRO *****

```

Listing C.2: An example of the program written in IDL to reconstruct the spectrum from the shots partially overlapping described in text earlier.

```
disp=0.0301 ;nm/pixel
```

```

tmp=string(1)
filename="C:\spectra0\disc1_1.prn"
myTemplate = ASCII_TEMPLATE(filename)
Result = READ_ASCII( Filename, template=mytemplate)
xs=result.field1
is=result.field2
xs=xs/10d0+0.5
is=-is*1d4+8d3
filename=string(tmp,FORMAT = '("C:\spectra0\dsc1_",I1, ".prn")', /print)
myTemplate = ASCII_TEMPLATE(filename)

    keywords = PSConfig(Cancel=cancelled)
    IF cancelled THEN RETURN
    thisDevice = !D.Name
    Set_Plot, 'PS'
    Device, _Extra=keywords
xwavelengthRange = [400,445];in nm
xwavenumberRange = 1.0 / (xwavelengthRange * 1e-7) ; In inversed cm
labels=[0.0,0.5,1.0]
plot ,xs, is ,/nodata, xsty=9,xra=xwavelengthRange,$
    yra=[-100,1.8d4], ysty=1,ytickformat='(A1)', yticks=2,yminor=2
axis ,yaxis=0,yrange=[0,1], yticks=2,yminor=2
Axis, XAxis=1.0,$
    XRange=xwavenumberRange, XTickFormat='(F9.1)', XStyle=1, XTicks=3

for j=0,20 do begin
tmp=string((1+j))
if j gt 8 then begin
filename=string(tmp,FORMAT = '("C:\spectra0\dsc1_",I2, ".prn")', /print)
endif else begin
filename=string(tmp,FORMAT = '("C:\spectra0\dsc1_",I1, ".prn")', /print)
endelse
Result = READ_ASCII( Filename, template=mytemplate)
x=result.field1
i=result.field2
x=x+j*(327.5)
x=disp*(x-288)+400
    oplot ,x, i , color=getcolor('blue',!d.table_size-2)
endifor
    oplot ,xs, is , color=getcolor('red',!d.table_size-3)
    Device, /Close_File
    Set_Plot, thisDevice
end

```

C.2 Dye laser step-motor driver

The MicroLYNX driver is a machine control system integrating a bipolar micro-stepping driver and expandable/programmable controller into a compact panel mounted assembly. It can be employed to drive a wide range of DC bipolar motors. We used it in combination with a tunable dye laser (Questek PDL3) to control the stepping motor that actuates the orientation of grating. The MicroLYNX needs to store a program in its memory. The program, written in a proprietary language, instructs the driver on how to put in motion, move faster, slow down, and rest the motor. In this way it is possible to customize the commands at which the driver must react as well as the information in output. The listing C.3 shows the code we implemented. In order to work correctly, the program defines how the values of the grating counter vary with motor movements.

Listing C.3: Code written in the MicroLYNX proprietary language to control the Dye-Laser stepper motor that actuates the grating movements.

```
Msel=256
Munit=200*Msel
Munit=Munit/360 'divide by 48 to give the actual munit in steps/counter
                 'every 360 degrees the counter movement is of 48 units
                 '1 unit:x=48:360

x=360/48
Munit=Munit/48
Mac=10
Mrc=10
Vi=0.01
Vm=0.05 '
#####

'posit: starting position
'nposit: end position
'wlength: actual position/grating order
'order: grating order
'delta: step-interval
'incr: counter value with values between 0 and Ntot
'newpos: posit+incr*delta
'ntot: number of deltas to reach nposit
'dlay: additional delay (coupled with vm) '-----you can give as input,
                 ' during the movement, a different
                 '-----velocity max-----

#####
Pgm 200
Pos=posit
INCr=0
```

```

newpos=0
Ntot=nposit-posit
ntot=ntot/delta

LBL muovi
INCr=INCr+1
    newpos=INCr*delta
    newpos=posit+newpos
    MOVA newpos
    wlength=Pos/order 'in angstrom '
    PRINT1 wlength

LBL waitin
INPUT1,Vm,1
    BR waitin , Mvg
    HOLD 2
        PRINT1 wlength
    DELAY 500
    BR muovi,INCr<ntot
wlength=Pos/order
PRINT1 wlength

END Pgm

```

C.2.1 Visual basic code to move the dye laser grating

I implemented a program in visual basic (VB) allowing to operate with the MicroLYNX device (described in previous section) via a graphical interface. In order to change the grating position of the dye laser, the VB code send proper instructions to the MicroLYNX device (in which the program with listing C.3 is loaded). The MicroLYNX energizes a DC sine motor to actuate the grating, modifying its orientation. In the program interface shown in Fig. C.2 two output displays are visible. The main output (marked as “out1”) shows the actual position expressed with counter units/wavelength per grating order. The second output (“out2”) returns the messages exchanged with the driving unit (MicroLYNX) during operations. To initialize the program, users are required to insert the counter reading (R_{count}) associated to the actual grating position. The grating order (n) needs also to be specified in advance. At this point a correspondence between grating wavelengths and counter values is established according to equation:

$$\frac{\lambda[\text{\AA}]}{1\text{\AA}} = n \times R_{count} \quad (\text{C.1})$$

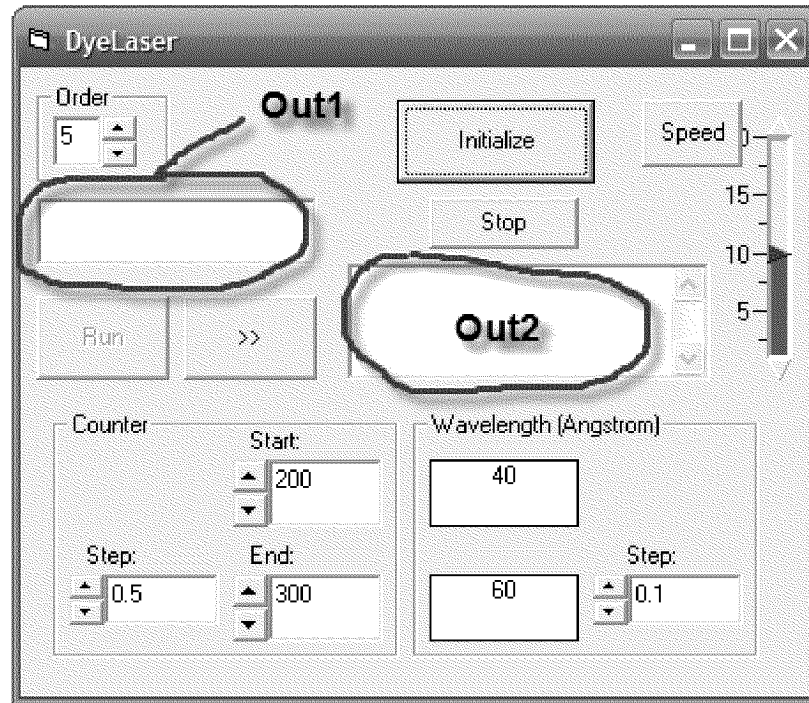


Figure C.2: Interface of a Visual Basic program written to control the grating position remotely.

Then users can interact with the program either by entering a wavelength or a counter value for the final grating orientation. The program instructs the MicroLYNX device to actuate the grating until the final orientation is accomplished. The grating can change its orientation in a continuous way (fast forward/backward mode) or in regular steps (scan mode). When wavelengths (counter values) associated to the start and final orientations of the grating are different:

- the fast forward/backward mode is started by pressing the “>>” button;
- the “Run” button starts the step movements of the grating in scan mode, with the size of increments/decrements given in the step fields (in wavelengths on the right hand side and counter values on the left).

Users can modify the velocity with which the grating changes its orientation using the button “Speed”. When this button is pressed the velocity in the vertical pointer slide is set. The grating order can be modified at any time using the list field available in the main interface. The buttons “Initialize” and “Stop” are used, respectively, to re-introduce the counter value for the actual grating orientation and to stop the serial communication with the MicroLYNX device.

C.2.2 Labview code to vary the voltages on the ReTof-MS

Six NHQ-233M (Iseg Spezialelektronik GmbH) power supplies (each having two independent outputs) were used to apply potentials to the ReTof-MS electrodes. They allow to adjust/scan their voltages or currents programmatically. Since an objective was to identify the best electrodes' potential, we started developing a simple program which could vary the voltage of either NHQ outputs, A and B. The interface of the program developed in Labview is shown in Fig. C.3. When the program is started it initializes the serial port communication according to parameters in "VISA session out". The "Channel(A)" list box specify if channel A or B is affected by the settings once the button "change" is pressed. The "Voltage" and "Current" fields give the actual output values. The values of "Voltage

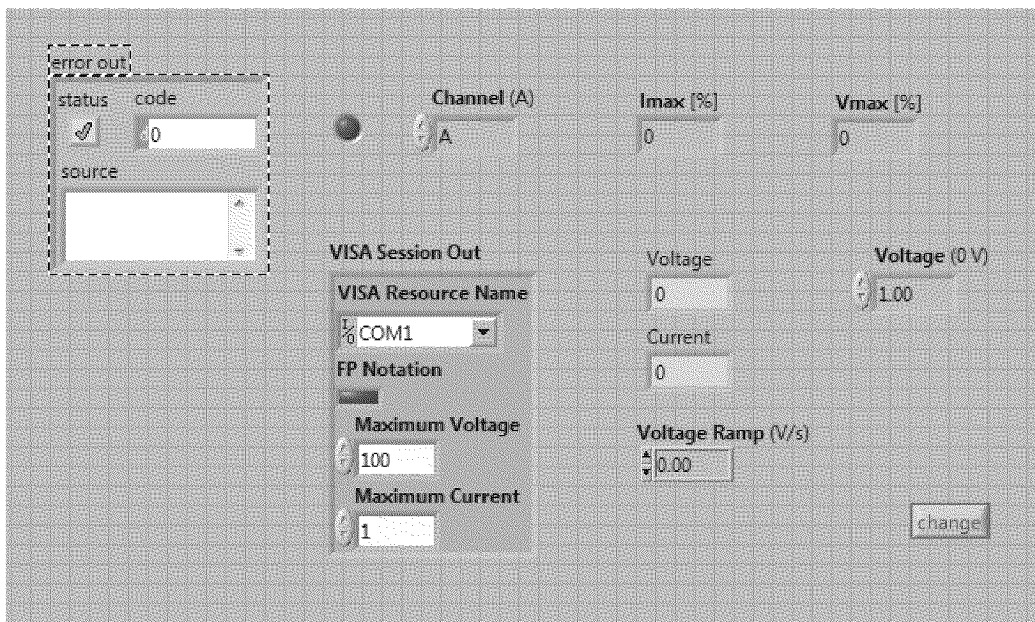


Figure C.3: Main interface of a Labview program to adjust NHQ output voltages of either channel A or B.

(0V)" and "Voltage Ramp (V/s)" fields are usually changed as they represent the final voltage value (to be reached) and rate with which this change has to occur respectively. Once their value is modified the button "change" has to be pressed to provide this new settings in input to the NHQ unit.

C.2.3 Labview programs to adjust DG535 and BNC555 time settings

In section 4.4 we discussed the importance of keeping constant and opportunely vary the phase between signal generated by the DG535 and BNC555 delay devices when the Indi-

scheme was used. There we mentioned about a program we developed to accomplish this tasks. In this section the main characteristics of the program written in Labview are shortly presented together with instructions on how to use its interface.

Figure C.4 shows the program's display on the screen¹. Prior to start the program, serial and gpib ports must be properly entered in the "VISA resource" list box and "GPIB address" entry field in order to establish the communication with BNC555 and DG535 respectively. The interface reads the current settings of both devices for the output signal of interest and calculates the phase relations accordingly to the frequency of the master signal ("Frequency" field). The timing of signals generated by the two devices is then represented on the screen with assigned symbol and colors identifying each signal. The user can at any time stop the program or read again the delay units' settings by pressing, respectively, the buttons "STOP" and "refresh".

The output fields "Valve to ion laser shot", "Valve to vap laser", and "flash to q-sw" show the computed time delays that play an important role, i.e. in the same order the time phases between:

- valve opening time and fs-laser firing;
- valve opening time and ablation laser firing;
- ablation laser flash lamp and Q switch.

The user can vary the channels A, B, C of the DG535 device through the program interface, first modifying the values of the entry fields labeled accordingly and then pressing the button "Send". After the new settings are sent to the DG535 device the transmission either occurs successfully or not. To avoid this kind of problems the settings are read again refreshing the content of the A, B, and C fields. In order to verify that changes occurred the user can check whether "lamp Delay" and "new lamp delay" fields have same values. In fact, the first field shows the current time setting for the ablation laser flash lamp while the other field give the setting required with the last data transmission to the delay devices. The switch button, "Abs position fixed", was introduced to allow the user to adjust the opening time of the valve, keeping constant the phase between the ablation laser and fs-laser firing. This can be done by pressing the "Yes" button. Other fields and buttons allow to store the actual settings on devices' local registries and to load them on request.

¹It was captured during an experiment with the valve, 6 cm away from the skimmer, injecting Ar+1%O₂ at 4 bar without the vaporization source in place.

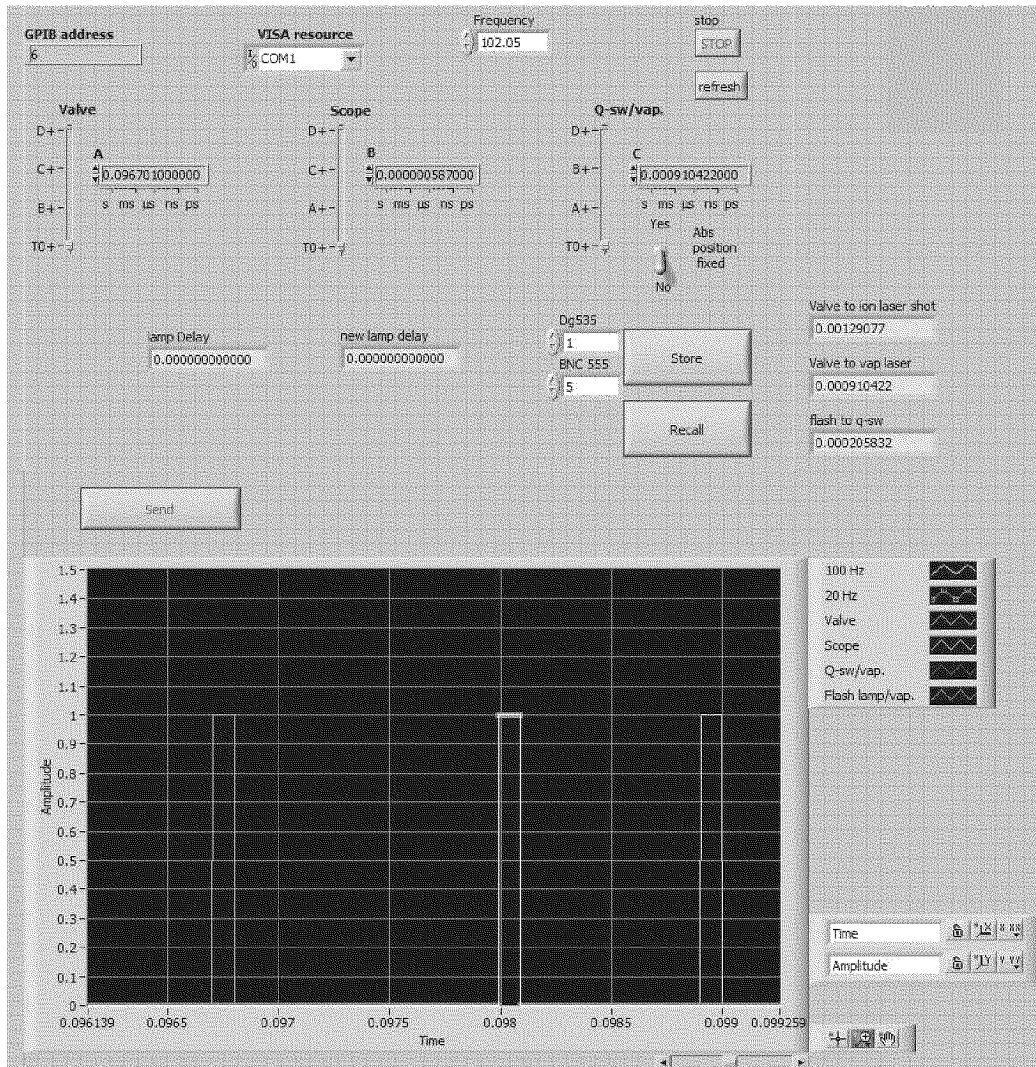


Figure C.4: Interface of the program that allow us to modify the time settings of the BNC555 and DG535 delay units accordingly. It allow to visualize/adjust the timing of pulses and store the corresponding settings.

Bibliography

- [1] C.W. Jr. Bauschlicher and H. Partridge. A comparison of ZnO and ZnO⁻. *Journal of Chemical Physics*, 109(19):8430–8434, 1998.
- [2] C.A. Fancher, H.L. de Clercq, O.C. Thomas, D.W. Robinson, and K.H. Bowen. Zinc oxide and its anion: A negative ion photoelectron spectroscopic study. *Journal of Chemical Physics*, 109(19):8426–8429, 1998.
- [3] Ü. Özgür, Ya.I. Alivov, C. Liu, A. Teke, M.A. Reshchikov, S. Doğan, V. Avrutin, S.-J. Cho, and H. Morkoçd. A comprehensive review of ZnO materials and devices. *Journal of Applied Physics*, 98(041301):1–103, 2005.
- [4] C.G. Van de Walle. Defect analysis and engineering in ZnO. *Physica B*, 308-310:899–903, 2001.
- [5] F. Kohan, G. Ceder, D. Morgan, and C.G. Van de Walle. First-principles study of native point defects in ZnO. *Physical Review B*, 61(22):15019–15027, 2000.
- [6] C.G. Van de Walle. Hydrogen as a cause of doping in zinc oxide. *Physical Review Letters*, 85(6):1012–1015, 2000.
- [7] Y.R. Ryu, S. Zhu, J.M. Wrobel, H.M. Jeong, P.C. Miceli, and H.W. White. Comparative study of textured and epitaxial ZnO films. *Journal of Crystal Growth*, 216(1):326–329, 2000.
- [8] K. Iwata, P. Fons, A. Yamada, K. Matsubara, and S. Niki. *J. Cryst. Growth*, 209:526, 2000.
- [9] D.C. Look, D.C. Reynolds, C.W. Litton, R.L. Jones, D.B. Eason, and G. Cantwell. *Applied Physics Letters*, 81:1830, 2002.
- [10] B.M.A. Ashrafi, I. Suemune, H. Kumano, and S. Tanaka. *Jpn. j. appl. phys.* 41(Part 2):L1281, 2002.

- [11] Y.R. Ryu, W.J. Kim, and H.W. White. Fabrication of homostructural ZnO p–n junctions. *Journal of Crystal Growth*, 219(4):419–422, 2000.
- [12] M.H. Huang, S. Mao, H. Feick, H. Yan, Y. Wu, H. Kind, E. Weber, R. Russo, and P. Yang. Room–temperature ultraviolet nanowire nanolasers. *Science*, 292(5523):1897–1899, 2001.
- [13] M. Epstein, K. Ehrensberger, and A. Yogev. Ferro-reduction of ZnO using concentrated solar energy. *Energy*, 29:745–756, 2004.
- [14] P. Haueter, R. Moeller, S. Palumbo, and A. Steinfeld. The production of zinc by thermal dissociation of zinc oxide – Solar chemical reactor design. *Solar Energy*, 67:161–167, 1999.
- [15] G.V. Chertihin and L. Andrews. Reactions of laser-ablated Zn and Cd atoms with O₂: Infrared spectra of ZnO, OZnO, CdO, and OCdO in solid argon. *Journal of Chemical Physics*, 106(9):3457–3465, 1997.
- [16] M. Keunecke, A. Meier, and R. Palumbo. Solar thermal decomposition of zinc oxide: an initial investigation of the recombination reaction in the temperature range 1100–1250 K. *Chemical Engineering Science*, 59(13):2695–2704, 2004.
- [17] A. Steinfeld, M. Brack, A. Meier, A. Weidenkaff, and D. Wuillemin. A solar chemical reactor for the co-production of zinc and synthesis gas. *Energy - The International Journal*, 23(10):803–814, 1998.
- [18] L. Brewer and D.F. Mastick. The stability of gaseous diatomic oxides. *Journal of Chemical Physics*, 19(7):834–845, 1951.
- [19] B. G. Wicke. Dynamics of the chemiluminescent oxidation of zinc atoms by nitrous oxide. *Journal of Chemical Physics*, 78(10):6036–6044, 1983.
- [20] L.R. Watson, T.L. Thiem, R.A. Dressler, R.H. Salter, and E. Murad. High temperature mass spectrometric studies of the bond energies of gas-phase zinc oxide, nickel oxide, and copper (II) oxide. *Journal of Physical Chemistry*, 97(21):5577–5580, 1993.
- [21] R.E. Leuchtner. Mass spectrometry and photoionization studies of the ablation of ZnO: ions, neutrals, and Rydbergs. *Applied Surface Science*, 127-129:626–632, 1998.

- [22] D.E. Clemmer, N.F. Dalleska, and P.B. Armentrout. Reaction of Zn^+ with NO_2 . the gas-phase thermochemistry of ZnO. *Journal of Chemical Physics*, 95(10):7263–7268, 1991.
- [23] E.S. Prochaska and L. Andrews. Infrared, Raman, and visible spectroscopic studies of Zn and Cd matrix reactions with ozone. Spectra of metalozonides and oxides in solid argon and nitrogen. *Journal of Chemical Physics*, 72(12):6782–6793, 1980.
- [24] V.D. Moravec, S.A. Klopčič, B. Chatterjee, and C.C. Jarrold. The electronic structure of ZnO and ZnF determined by anion photoelectron spectroscopy. *Chemical Physics Letters*, 341:313–318, 2001.
- [25] J.H. Kim, Xi Li, Lai-Sheng Wang, H.L. de Clercq, C.A. Fancher, O.C. Thomas, and K.H. Bowen. Vibrationally resolved photoelectron spectroscopy of MgO^- and ZnO^- and the low-lying electronic states of MgO, MgO^- , and ZnO. *Journal of Physical Chemistry A*, 105(23):5709–5718, 2001.
- [26] D.S. Pešić. Emission spectrum of zinc oxide between 6000 and 5000 Å. *Croatica Chemica Acta*, 38:313–315, 1966.
- [27] C.W. Jr. Bauschlicher and S.R. Langhoff. Theoretical study of the low-lying electronic states of ZnO and ZnS. *Chemical Physics Letters*, 126(2):163–168, 1986.
- [28] J.Q. Hu, X.L. Ma, Z.Y. Xie, N.B. Wong, C.S. Lee, and S.T. Lee. Characterization of zinc oxide crystal whiskers grown by thermal evaporation. *Chemical Physics Letters*, 344(1):97–100, 2001.
- [29] E.C. Behrman, R.K. Foehrweiser, J.R. Myers, and M.E. French, B.R. and Zandler. Possibility of stable spheroid molecules of ZnO. *Physical Review A*, 49(3):R1543–R1546, 1994.
- [30] M.E. Zandler, E.C. Behrman, M.B. Arrasmith, J.R. Myers, and T.V. Smith. Semiempirical molecular orbital calculation of geometric, electronic, and vibrational structures of metal oxide, metal sulfide, and other inorganic fullerene spheroids. *Journal of Molecular Structure (Theochem)*, 362:215–224, 1996.
- [31] J.M. Matxain, J.E. Fowler, and J.M. Ugalde. Small clusters of ii-vi materials: Zn_iO_i , $i = 1-9$. *Physical Review A*, 62(5):053201(1–10), 2000.

- [32] A.V. Bulgakov, I. Ozerov, and W. Marine. Laser ablation synthesis of zinc oxide clusters: a new family of fullerenes? E-print, <http://arXiv.org/abs/physics/0311117>, 2003.
- [33] I. Ozerov, A.V. Bulgakov, D.K. Nelson, R. Castell, M. Sentis, and W. Marine. Ablation de ZnO par laser UV (193 nm): Nano-agregats en phase gazeuse. *Journal de Physique. IV*, 108:37–40, 2003.
- [34] I. Ozerov, A.V. Bulgakov, D.K. Nelson, R. Castell, and W. Marine. Production of gas phase zinc oxide nanoclusters by pulsed laser ablation. *Applied Surface Science*, 247:1–7, 2005.
- [35] L.M. Kukreja, A. Rohlfiing, P. Misra, F. Hillenkamp, and K. Dreisewerd. Cluster formation in UV laser ablation plumes of ZnSe and ZnO studied by time-of-flight mass spectrometry. *Applied Physics A*, 78(5):641–644, 2004.
- [36] F. Claeysens, A. Cheesman, S.J. Henley, and M.N.R. Ashfold. Studies of the plume accompanying pulsed ultraviolet laser ablation of zinc oxide. *Journal of Applied Physics*, 92(11):6886–6894, 2002.
- [37] E.R. Fisher, J.L. Elkind, D.E. Clemmer, R. Georgiadis, S.K. Loh, N. Aristov, L.S. Sunderlin, and P.B. Armentrout. Reactions of fourth-period metal ions ($\text{Ca}^+ - \text{Zn}^+$) with O_2 : Metal-oxide ion bond energies. *Journal of Chemical Physics*, 93(4):2676–2691, 1990.
- [38] K.S. Haber, J.W. Zwanziger, F.X. Campos, R.T. Wiedmann, and E.R. Grant. Direct determination of the adiabatic ionization potential of NO_2 by multiresonant optical absorption. *Chemical Physics Letters*, 144(1):58–64, 1988.
- [39] S.W. Hunsucker. *Time-of-Flight Mass Spectrometry to Characterize Inorganic Coordination Complexes of Cyanobacteria*. PhD thesis, Virginia Polytechnic Institute and State University, 2001.
- [40] M.L. Campbell, E.J. Kölsch, and K.L. Hooper. Kinetic study of the reactions of gas-phase $\text{V}(a^4\text{F}_{3/2})$, $\text{Cr}(a^7\text{S}_3)$, $\text{Co}(a^4\text{F}_{9/2})$, $\text{Ni}(a^3\text{F}_4, a^3\text{D}_3)$ and $\text{Zn}(4s^2 \ ^1\text{S}_0)$ atoms with nitrous oxide. *Journal of Physical Chemistry A*, 104(47):11147–11153, 2000.
- [41] E. Cartmell and G.W. A. Fowles. *Valency and molecular structure*. Butterworth & Co. Ltd, 1966.

- [42] L. Pauling. *The Nature of the Chemical Bond*. Cornell University Press, Ithaca, NY, 3rd edition, 1967.
- [43] G. Sproul. Electronegativity and bond type: Predicting bond type. *Journal of Chemical Education*, 78(3):387–390, 2001.
- [44] E.G. Bakalbassis, M.D. Stiakaki, A.C. Tsipis, and C.A. Tsipis. Ground and low-lying excited state properties of the first-row transition-metal oxide diatomics calculated by an improved ased-mo model. *Chemical Physics*, 205:389–399, 1996.
- [45] P. Bodek and I. Alxneit. Rekin, an experiment to study the kinetics of the oxidation of zinc vapour - conceptual overview and design. In *PSI-Scientific Report*, volume V, pages 25–26, 2002.
- [46] P. Bodek and I. Alxneit. Rekin - characterization of the experiment, first results of the flow visualization. In *PSI-Scientific Report*, volume V, pages 37–38, 2004.
- [47] L.S. Andrews, A. Rohrbacher, C.M. Laperle, and R.E. Continetti. Laser desorption/ionization of transition metal atoms and oxides from solid argon. *Journal of Physical Chemistry A*, 104(35):8173–8177, 2000.
- [48] A. Pramann, K. Koyasu, A. Nakajima, and K. Kaya. Photoelectron spectroscopy of cobalt oxide cluster anions. *Journal of Physical Chemistry A*, 106(19):4891–4896, 2002.
- [49] D.N. Shin, Y. Matsuda, and E.R. Bernstein. On the iron oxide neutral cluster distribution in the gas phase. I. Detection through 193 nm multiphoton ionization. *Journal of Chemical Physics*, 120(9):4150–4156, 2004.
- [50] Y. Matsuda, D.N. Shin, and E.R. Bernstein. On the zirconium oxide neutral cluster distribution in the gas phase: Detection through 118 nm single photon, and 193 and 355 nm multiphoton, ionization. *Journal of Chemical Physics*, 120(9):4142–4149, 2004.
- [51] W.J. Balfour, J. Cao, R.H. Jensen, and R. Li. The spectrum of nickel monoxide between 410 and 510 nm: laser-induced fluorescence and dispersed fluorescence measurements. *Chemical Physics Letters*, 385(3):239–243, 2004.
- [52] S. DePaul, D. Pullman, and B. Friedrich. A pocket model of seeded supersonic beams. *The Journal of Physical Chemistry*, 97(10):2167–2171, 1993.

- [53] J. Westergren and H. Gröbeck. Noble gas temperature control of metal clusters: a molecular dynamics study. *Journal of Chemical Physics*, 107(8):3071–3079, 1997.
- [54] *Laser Applications to Chemical Dynamics*, volume 742 of *Proceedings of the SPIE - The International Society for Optical Engineering*, 13-14 Jan 1987. Los Angeles, CA, USA.
- [55] P. Milani and W.A. deHeer. Improved pulsed laser vaporization source for production of intense beam of neutral and ionized clusters. *Review of Scientific Instruments*, 61(7):1835–1838, 1990.
- [56] W.A. deHeer and P. Milani. An improved laser vaporization cluster source and time-of-flight mass spectrometer. *Z. Phys. D - Atoms, Molecules and Clusters*, 20:437–439, 1991.
- [57] F.K. Urban III, S.W. Feng, and J.J.I Nainaparampi. Determination of zinc cluster size in ionized cluster beam film deposition. *Journal of Applied Physics*, 74(2):1335–1338, 1993.
- [58] A.R. Skinner and D.W. Chandler. Spectroscopy with supersonic jets. *American Journal of Physics*, 48(1):8–13, 1980.
- [59] C.C. Jr. Leiby and A.L. Besse. Molecular beams and effusive flows. *American Journal of Physics*, 47(9):791–796, 1979.
- [60] R.E. Smalley, L. Wharton, and D.H. Levy. Molecular optical spectroscopy with supersonic beams and jets. *Accounts of Chemical Research*, 10:139–145, 1977.
- [61] A. Kantrowitz and J. Grey. A high intensity source for the molecular beam. Part I. Theoretical. *Review of Scientific Instruments*, 22(5):328–332, 1951.
- [62] M. D. Morse. Supersonic beam sources. In F. Dunning and R. Hulet, editors, *Atomic, molecular, and optical physics: Atoms and molecules*, volume 29B, pages 21–46. 1996.
- [63] A.E. Cameron and D.F. Jr. Eggers. An ion “velocitron”. *Review of Scientific Instruments*, 19(9):605–607, 1948.
- [64] R.E. Steiner, C.L. Lewis, and V. Majidi. Consideration of a millisecond pulsed glow discharge time-of-flight mass spectrometer for concurrent elemental and molecular analysis. *Journal of Analytical Atomic Spectrometry*, 14:1537–1541, 1999.

- [65] A. Zelenyuk and D. Imre. Single particle laser ablation time-of-flight mass spectrometer: An introduction to SPLAT. *Aerosol Science and Technology*, 39:1–15, 2005.
- [66] W.C. Wiley and I.H. McLaren. Time-of-flight mass spectrometer with improved resolution. *Review of Scientific Instruments*, 26(12):1150–1157, 1955.
- [67] D.M. Lubman and R.M. Jordan. Design for improved resolution in a time-of-flight mass spectrometer using a supersonic beam and laser ionization source. *Review of Scientific Instruments*, 56(3):373–376, 1985.
- [68] M. Guilhaus. Principles and instrumentation in Time-of-Flight Mass Spectrometry. *Journal of Mass Spectrometry*, 30(11):1519–1532, 1995.
- [69] J.O. Clevenger. *Spectra and Dynamics of Calcium Monochloride*. PhD thesis, Massachusetts Institute of Technology, 2002.
- [70] B.A. Mamyrin, V.I. Karataev, D.V. Shmikk, and V.A. Zagulin. The mass-reflectron, a new nonmagnetic time-of-flight mass spectrometer with high resolution. *Sov. Phys.-JETP*, 37(1):45–48, 1973.
- [71] BURLE optics Inc. Burle long-life MCP selection guide (<http://www.burle.com>). (Burle Electro-optics Inc., Sturbridge, Ma, 2003).
- [72] O. Almen, W. Hartmann, K. Frank, and J. Christiansen. Fast rise time, high sensitivity MCP ion detector for low-energy ion spectroscopy. *Journal of Physics E*, 22(6):382–386, 1989.
- [73] P.P. Radi, P. Beaud, D. Franzke, H.-M. Frey, T. Gerber, B. Mischler, and A.-P. Tzannis. Femtosecond photoionization of $(\text{H}_2\text{O})_n$ and $(\text{D}_2\text{O})_n$ clusters. *Journal of Chemical Physics*, 111(2):512–518, 1999.
- [74] R. Odom and B. Schueler. *Lasers and Mass Spectrometry*, chapter 5. Oxford University Press, 1990.
- [75] P.J. Brucat, L.-S. Zheng, C.L. Pettiette, S. Yang, and R.E. Smalley. Metal cluster ion photofragmentation. *Journal of Chemical Physics*, 84(6):3078–3088, 1986.
- [76] U. Heiz, F. Vanolli, L. Trento, and W.-D. Schneider. Chemical reactivity of size-selected supported clusters: An experimental setup. *Review of Scientific Instruments*, 68(5):1986–1994, 1997.

- [77] T. Vystavel, G. Palasantzas, S.A. Koch, and Th.M. De Hosson. Niobium nanoclusters studied with *in situ* transmission electron microscopy. *Applied Physics Letters*, 83(19):3909–3911, 2003.
- [78] J.R. Sambrano, J. Andrés, A. Beltrán, F. Sensato, and E. Longo. Theoretical study of the structure and stability of Nb_xO_y and Nb_xO_y^+ ($x=1-3$; $y=2-5, 7, 8$) clusters. *Chemical Physics Letters*, 287:620–626, 1998.
- [79] H.T.K. Deng, K.P. Kerns, and A.W.Jr. Castleman. Formation, structures, and reactivities of niobium oxide cluster ions. *Journal of Physical Chemistry*, 100:13386–13392, 1996.
- [80] P.P. Radi, G. von Helden, M.T. Hsu, P.R. Kemper, and M.T. Bowers. Thermal bimolecular reactions of size selected transition metal cluster ions: $\text{Nb}_n^+ + \text{O}_2$, $n=1-6$. *International Journal of Mass Spectrometry and Ion Processes*, 109:49–73, 1991.
- [81] V. Kumar and Y. Kawazoe. Atomic and electronic structures of niobium clusters. *Physical Review B*, 65(12):125403(1–11), 2002.
- [82] K. Athanassenas, D. Kreisle, B.A. Collings, D.M. Rayner, and P.A. Hackett. Ionization potentials of niobium cluster oxides. *Chemical Physics Letters*, 213(1–2):105–110, 1993.
- [83] J.W. Kauffman, R.H. Hauge, and J.L. Margrave. Studies of reactions of atomic and diatomic Cr, Mn, Fe, Co, Ni, Cu, and Zn with molecular water at 15 K. *Journal of Physical Chemistry*, 89(16):3541–3547, 1985.
- [84] T.M. Greene, W. Brown, L. Andrews, A.J. Downs, G.V. Chertihin, N. Runeberg, and P. Pyykkö. Matrix infrared spectroscopic and ab initio studies of ZnH_2 , CdH_2 , and related metal hydride species. *Journal of Physical Chemistry*, 99:7925–7934, 1995.
- [85] M.E. Jacox. Vibrational and electronic energy levels of polyatomic transient molecules: Supplement A. *Journal of Physical and Chemical Reference Data*, 27(2):115–393, 1998.
- [86] T.G. Dietz, M.A. Duncan, D.E. Powers, and R.E. Smalley. Laser production of supersonic metal cluster beams. *Journal of Physical Chemistry*, 74(11):6511–6512, 1981.

- [87] Z. Liu, M.P. Gelinas, and R.D. Coombe. II-VI compound thin-film deposition by resonant laser sputtering. *Journal of Applied Physics*, 75(6):3098–3104, 1994.
- [88] A. Sharma. Dendritic aggregation of metal hydrides and oxides in a laser-produced aerosol medium. *Physical Review A*, 45(6):4184–4187, 1992.
- [89] H. Wollnik. Time-of-flight mass analyzers. *Mass Spectrometry Reviews*, 12(2):89–114, 1993.
- [90] D.A. Dahl. *SIMION 3D Version 7.0 User's Manual*. Idaho Nat. Eng. Laboratory, 2000.
- [91] I.V. Veryovkin, C.Y. Chen, W.F. Calaway, M.J. Pellin, and T. Lee. Computer simulation of time-of-flight mass spectrometers: calculations of mass spectra and spatial distributions of ions. *Nuclear Instruments and Methods in Physics Research A*, 519(1-2):345–352, 2004.
- [92] G.E.P. Box and M. E. Muller. A note on the generation of random normal deviates. *Annals of Mathematical Statistics*, 29:610–611, 1958.
- [93] S.S. Harilal, C.V. Bindhu, M.S. Tillack, F. Najmabadi, and A.C. Gaeris. Internal structure and expansion dynamics of laser ablation plumes into ambient gases. *Journal of Applied Physics*, 93(5), 2003.
- [94] M.S. Tillack, D.W. Blair, and S.S. Harilal. The effect of ionization on cluster formation in laser ablation plumes. *Nanotechnology*, 15:390–403, 2004.
- [95] L.V. Zhigilei and B.J. Garrison. Velocity distributions of molecules ejected in laser ablation. *Appl. Phys. Lett.*, 71(4):551–553, 1997.
- [96] R.W. Dreyfus. *Laser Ablation of Electronic Materials: Basic Mechanisms and Applications*, volume 4, chapter Comparison of the Ablation of Dielectrics and Metals at High and Low Laser Powers, pages 61–72. European Materials Research Society Monographs, North-Holland, Amsterdam, 1992.
- [97] I.C.E. Turcu, M.C. Gower, and P. Huntington. Measurement of KrF laser breakdown threshold in gases. *Optics Communications*, 134:66–68, 1997.
- [98] H.R. Griem. High-density corrections in plasma spectroscopy. *Physical Review*, 128(3):997–1003, 1962.

-
- [99] Edison NJ 08820 SPEX Industries, Inc. 3880 Park Ave. *M Series - 500M, 750M, 1000M, 1250M*. HORIBA Jobin Yvon.
- [100] Edison NJ 08820 SPEX Industries, Inc. 3880 Park Ave. *CD2A-B CompuDrive*. HORIBA Jobin Yvon.
- [101] Princeton Instruments. *Macro Basic Programming*, revision 1.b edition, 1997. [ftp://ftp.roperscientific.com/Manuals/Files/Archived/Macro Basic Programming Manual.pdf](ftp://ftp.roperscientific.com/Manuals/Files/Archived/Macro%20Basic%20Programming%20Manual.pdf).

Curriculum Vitae

Name Daniele Cannavò
Nationality Italian
Birthday 06.09.1971

2001-2006 PhD student at ETH, Zurich
2001-2004 Research assistant at Paul Scherrer Institute (PSI),
Reaction Analysis Group, Villigen
2000-2001 Project for an infrared beamline at the Swiss Light
Source (SLS) -ETH/PSI fellowship
July 1999 Laurea” degree (Master equivalent) in Physics
with final evaluation of **110/110**. Line of study:
Biophysics. University of Rome, “La Sapienza” (Italy)
Master Thesis: *Beamlines design for infrared
synchrotron radiation*
Advisors: Prof. P. Calvani (IRS) and Dr. A. Marcelli (INFN)
1997-1998 Research assistant at National Institute of Nuclear Physics
(INFN-LNF), Frascati (Rome)
1995 Research on X-rays metrology at ‘Casaccia’ ENEA laboratories,
1986-1991 Pre-University education